Wrocław University
of Science and Technology

FIELD OF SCIENCE: Natural Sciences

DISCIPLINE OF SCIENCE: Physical Sciences

DOCTORAL DISSERTATION

“The use of fiber optics in spectroscopic setups for studying of van der Waals crystals”

Karolina Ciesiołkiewicz-Klepek

Supervisor:
prof. dr hab. inż. Robert Kudrawiec

Co-supervisor:
dr inż. Jan Kopaczek

Keywords: TMDC, optical fiber, modulation spectroscopy, optical spectroscopy, van der Waals crystals

WROCŁAW 2025

Acknowledgments

First of all, I would like to thank my supervisors, Prof. Robert Kudrawiec and Dr. Jan Kopaczek, for guiding me through the journey of my doctoral studies, for their invaluable academic support, for all the ideas and problem-solving together, and above all, for their confidence in me, which was a constant source of motivation.

I am also grateful to my colleagues from the Department of Semiconductor Materials Engineering for introducing me to the laboratory, for their constant willingness to help, and for creating an atmosphere that made coming to work a pleasure.

Special thanks go to Prof. Tomasz Polak, who was the first to show me the beauty of physics.

I would like to thank the friends I made during my studies for all the time spent studying together, for their motivation, and above all, for their support, which has continued beyond our studies and remains present in the important moments of my life.

Z głębi serca dziękuję moim Rodzicom, których wsparcie i pozytywne spojrzenie na świat dodawało mi wiary w chwilach zwątpienia, a także mojej Babci, która swoim życiem i postawą stała się dla mnie wzorem siły. Za ich miłość.

Finally, I dedicate this work to my Love, Arkadiusz, whom I am fortunate to call my husband.

Streszczenie

Niniejsza rozprawa doktorska stanowi cykl czterech artykułów naukowych, które koncentrują się na zagadnieniach związanych z wykorzystaniem światłowodów optycznych jako platformy pomiarowej do badania właściwości kryształów van der Waalsa. Poszczególne prace obejmują zarówno rozwój i implementację nowych technik spektroskopowych, jak i ich zastosowanie do analizy zjawisk optycznych w dichalkogenkach metali przejściowych (TMDC).

W pierwszym artykule opisano badania nad układem do fotoodbicia i bezkontaktowego elektroodbicia wzbogaconym o światłowody, co umożliwiło fizyczne oddzielenie strefy pomiarowej od źródła wzbudzenia i detektorów. Systematyczne badania nad wpływem średnicy rdzenia oraz odległości od próbki ujawniły ich znaczenie dla jakości sygnału. Taka konfiguracja w pomiarach dla bezkontaktowego elektroodbicia wyeliminowała efekt cienia, zwiększyła bezpieczeństwo pomiarowe i wzmocniła sygnał.

Kolejne prace rozwinęły koncepcję spektroskopii typu lab-on-fiber poprzez przeniesienie cienkich warstw TMDC bezpośrednio na powierzchnię końcówki włókna. Umożliwiło to opracowanie metody termotransmitancji, w której lokalne nagrzewanie indukowane laserowo prowadziło do mierzalnych przesunięć rezonansów ekscytonowych i zmian współczynnika absorpcji, co opisano w drugim artykule.

Trzeci artykuł opisuje dalszy rozwój układu, który został wzbogacony o pomiary kriogeniczne dzięki integracji adaptera światłowodowego z kriostatem helowym o obiegu zamkniętym. Konstrukcja ta zapewniła wyjątkową stabilność, odporność na wibracje i eliminację problemu dryftu temperaturowego, umożliwiając badania fotoluminescencji, transmisji, fotomodulowanej transmisji i fotoodbicia w szerokim zakresie temperatur. System z powodzeniem zastosowano do cienkich warstw, monowarstw i heterostruktur. Ważnym aspektem była także stosunkowo niska cena budowy takiego układu dzięki wykorzystaniu popularnego kriostatu o obiegu zamkniętym.

W ostatnim artykule zaprezentowano spektroskopię transmisyjną stopów monowarstwowych na bazie MoS_2. Eksperymenty wykazały, że zastąpienie siarki selenem powoduje przesunięcie przejść ekscytonowych ku czerwieni, natomiast zastąpienie molibdenu wolframem prowadzi do przesunięcia ku wyższym energiom. Stwierdzono również, że wrażliwość temperaturowa ekscytonów silnie zależy od składu stopu: struktury bogate w wolfram i selen wykazują większe przesunięcia energetyczne wraz ze zmianą temperatury.

Wyniki uzyskane w niniejszej rozprawie wskazują, że techniki światłowodowe mogą rozszerzyć możliwości eksperymentalne charakteryzacji materiałów 2D. Opracowane metody oparte na światłowodach umożliwiają precyzyjne, stabilne i wszechstronne pomiary optyczne zarówno w warunkach otoczenia, jak i kriogenicznych, pokazując potencjał tego podejścia w przyszłych zastosowaniach w spektroskopii i urządzeniach ze zintegrowanymi światłowodami opartych na kryształach van der Waalsa.

Abstract

This doctoral dissertation consists of a series of four scientific articles that focus on the use of optical fibers as a measurement platform for investigating the properties of van der Waals crystals. The individual studies cover both the development and implementation of new spectroscopic techniques as well as their application to the analysis of optical phenomena in transition metal dichalcogenides (TMDCs).

The first article describes research on a photoreflectance and contactless electroreflectance setup enhanced with optical fibers, which allowed the physical separation of the measurement zone from the excitation source and detectors. Systematic studies of the fiber core diameter and sample-to-fiber distance revealed their impact on signal quality. This configuration in contactless electroreflectance measurements eliminated the shadow effect, increased measurement safety and amplified the signal.

Subsequent works expanded the concept of lab-on-fiber spectroscopy by transferring thin TMDC layers directly onto the fiber facet. This enabled the development of a thermotransmittance method, where local laser-induced heating led to measurable shifts in excitonic resonances and changes in the absorption coefficient, as described in the second article.

The third article presents further development of the system, which was extended to cryogenic measurements through the integration of a fiber-to-fiber adapter with a closed-cycle helium cryostat. This design provided exceptional stability, vibration resistance, and eliminated temperature drift, allowing the study of photoluminescence, transmission, photomodulated transmission, and photoreflectance over a wide temperature range. The system was successfully applied to thin films, monolayers, and heterostructures. An important aspect was the relatively low cost of constructing such a setup, thanks to the use of a commercially available closed-cycle cryostat.

In the final article, optical transmission spectroscopy of monolayer alloys based on MoS_2 is presented. The experiments showed that substituting sulfur with selenium leads to a redshift of excitonic transitions, while replacing molybdenum with tungsten results in a blueshift. It was also found that the temperature sensitivity of excitons strongly depends on alloy composition: tungsten- and selenium-rich structures exhibit larger energy shifts with temperature.

The results obtained in this dissertation indicate that fiber-optic techniques can expand the experimental capabilities for characterizing 2D materials. The developed fiber-based methods allow precise, stable, and versatile optical measurements under both ambient and cryogenic conditions and highlight the potential of this approach for future applications in spectroscopy and fiber-integrated devices based on van der Waals crystals.

Contents

1. Introduction

1.1. Motivation and Hypothesis

Optical fibers, which for decades have served primarily in optical communication,[1] are now emerging as tools for precise diagnostics of matter at the micro- and nanoscale.[2,3] At the same time, the discovery and intensive study of van der Waals (vdW) crystals have significantly advanced our understanding of the properties of solid-state materials.[4,5] The convergence of these two fields: fiber optics and the physics of two-dimensional (2D) materials,[6,7] forms the starting point of this dissertation. The hypothesis proposed herein is that combining these disciplines will not only simplify spectroscopic setups but also deepen understanding of the properties of vdW crystals.

In recent years, 2D materials, particularly transition metal dichalcogenides (TMDCs),[8–10] have attracted significant attention due to their unique optical and electronic properties,[11–13] as well as their potential for applications in advanced optoelectronic technologies.[14,15] The optical properties of these materials, including their band gap, can be precisely tuned by modifying the material's thickness,[16] applying external strain,[17] introducing dopants into the crystal structure,[18] varying the temperature,[19] or forming alloys.[20] These features offer an exceptionally broad range of property engineering, enabling the design of devices such as diodes,[21] lasers,[22] detectors,[23] and sensors.[24] As research in this field progresses, there is a growing need for more precise, stable, and versatile characterization techniques for ultrathin layers, particularly under varying temperatures, electric fields, or in experimental setups requiring miniaturization. In this context, optical fibers, until recently used mainly in telecommunications and optical sensing, are becoming promising platforms for fundamental spectroscopic applications as well. Their integration into measurement systems offers several advantages: mechanical stability, precise sample positioning, compatibility with cryogenic conditions, and the miniaturization of the entire experimental setup.

This dissertation presents a series of experiments utilizing fiber-optic techniques to investigate primarily the optical properties of van der Waals crystals, with additional studies on III-V semiconductors. The primary focus of these studies lies in the development and implementation of measurement systems based on optical fibers, allowing light transmission or reflection through (or from) monolayers placed directly on the fiber core, and enabling modulation spectroscopy measurements such as photoreflectance, contactless electroreflectance, and photomodulated transmission. It is demonstrated that the use of optical fibers not only improves the quality and repetability of measurements but also enables access to experimental regimes, such as studies of monolayers and few-layer systems, that were previously difficult to achieve using modulation spectroscopy techniques conventionally employed in our laboratories. The hypothesis of this work is that, by incorporating optical fibers, spectroscopic setups can not only be simplified but also provide enhanced capabilities for characterizing van der Waals crystals. The validation of this hypothesis is supported by results obtained using a range of spectroscopic techniques which, when implemented in a novel fiber-based configuration, enable more precise, stable, and versatile optical studies of 2D materials.

1.1. Optical spectroscopy

Optical spectroscopy provides a tool for probing the fundamental properties of semiconductors. When light interacts with a semiconductor, it can be absorbed, transmitted, or reflected in ways that depend sensitively on the material's electronic band structure, excitonic effects, impurity states, and phonon interactions. The energies at which these processes occur reveal information about the band gap, critical points, defect levels, and the presence of excitons or free carriers. By analyzing the spectral features such as absorption edges, reflectance minima or maxima, and photoluminescence (PL) peaks, under various external conditions, one can gain detailed insights into the optical and electronic behavior of semiconductor materials.[4,5,25]

1.2. Optical Absorption

Optical absorption is one of the most powerful and widely used tools for investigating semiconductor materials. It relies on the interaction of light with matter, enabling the extraction of key optical parameters such as reflectance, transmittance, and absorption coefficients, as well as information on electronic transitions, band structure, and excitonic effects. The fundamental principle of optical spectroscopy involves measuring changes in the intensity or energy of electromagnetic radiation after it passes through a sample, is reflected from its surface, or is emitted as a result of external excitation. Optical absorption in semiconductors refers to the process in which photons are absorbed by electrons, promoting them from the valence band to the conduction band. This phenomenon is strongly influenced by the material's electronic band structure and the joint density of states. Near the absorption edge, the absorption coefficient $\alpha(E)$ rises steeply due to interband transitions and possible excitonic resonances. The amount of light absorbed as it travels through a material of thickness d is described by the Lambert–Beer law:

$$I = I_0 e^{-\alpha/d} \tag{1.1}$$

where I_0 is the intensity of the incident light, I is the transmitted intensity, α is the absorption coefficient [cm^{-1}], d is the thickness of the material. In practical applications, if the sample is much thicker than the coherence length of the light, interference effects can be neglected. In that case, the total transmittance T for a thin film of thickness d with absorption coefficient α and single-pass reflectance R is expressed as:

$$T = \frac{(1-R)^2 e^{-\alpha d}}{1-R^2 e^{-2\alpha d}} \tag{1.2}$$

For strongly absorbing materials, where internal reflections can be neglected, this simplifies to:

$$T = (1-R)^2 e^{-\alpha d} \tag{1.3}$$

From this, one can derive an expression for the absorption coefficient α:

$$\alpha = -\frac{1}{d} \ln \frac{T}{(1-R)^2} \tag{1.4}$$

Thus, in an experiment, determining the absorption coefficient requires knowledge of both the reflectance and transmittance spectra as a function of photon energy. Analyzing these quantities

allows for accurate determination of band gap energies, excitonic features, and temperature-dependent shifts of electronic transitions.[4,5]

A typical optical measurement setup (Figure 1) for collecting reflectance and transmittance spectra includes a light source (tungsten-halogen lamp) modulated by a mechanical chopper operating at a few hundred hertz, a monochromator, and a photodetector. The light is focused onto the sample, and depending on the configuration, either the reflected or transmitted light is collected and directed to a monochromator for spectral dispersion. The spectrally resolved light is then detected using a photodetector selected according to the spectral range of interest, for example, Si photodiodes for the visible region and InGaAs detectors for the near-infrared. To enhance the signal-to-noise ratio, the system uses lock-in detection, which isolates the signal component modulated at the reference frequency, thereby greatly suppressing background noise.[26] The setup can be modified by replacing the monochromator and detector with a spectrometer, which enables faster measurements by recording the entire spectrum simultaneously. In this case, the use of a chopper is also unnecessary. However, it should be noted that the spectrometer may have a limited spectral range and introduce more noise.

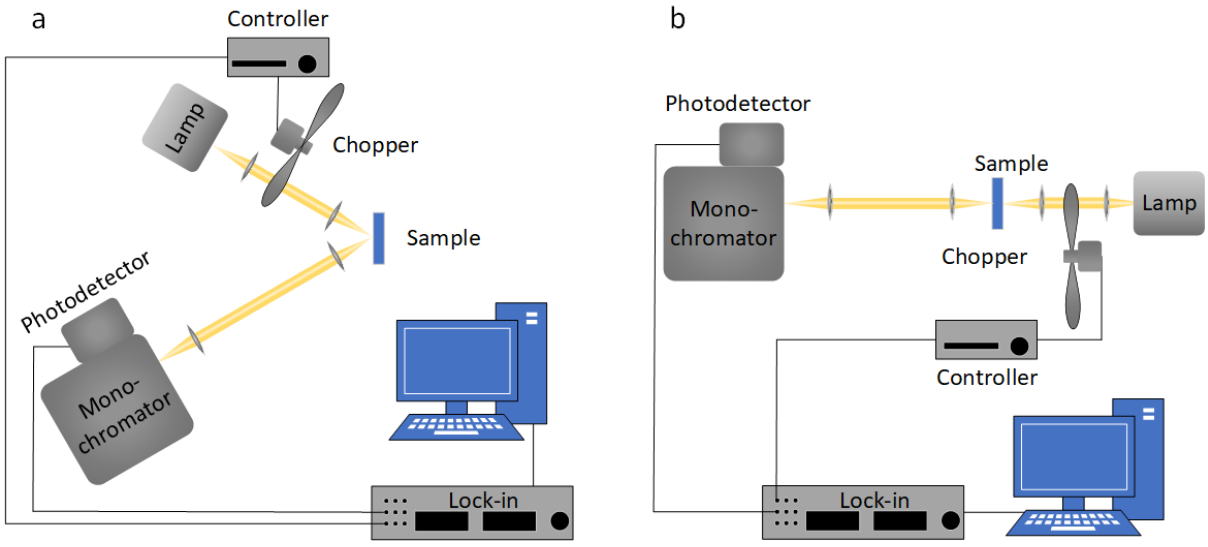

Figure 1. Schematic diagram of the system for measuring reflectance (a) and transmission (b).

1.3. Modulation spectroscopy

Modulation spectroscopy is an advanced optical technique that enhances sensitivity to subtle features related to the electronic structure, particularly optical transitions. Unlike standard absorption or photoluminescence measurements, which detect absolute signal levels, modulation spectroscopy detects small changes in the optical response induced by an external perturbation. In particular, modulation spectroscopy techniques provide precise information about the energy position, broadening, and amplitude of optical transitions, making them highly sensitive to subtle changes in a material's electronic structure. Moreover, modulation spectroscopy methods are typically classified based on the type of external perturbation applied to the sample, which induces changes in the optical response near critical points in the joint density of states, corresponding to interband transitions at high-symmetry points in the electronic band structure. These perturbations may include: internal electric field modulation

(photoreflectance, photomodulated transmission, electroreflectance, contactless electroreflectance), temperature variations (thermoreflectance), and mechanical stress (piezoreflectance). Such perturbations modify the internal electronic or structural properties of the material, leading to characteristic derivative-like features in the optical spectrum at the transition energies. These appear as resonance-like line shapes, allowing the identification of otherwise weak or indistinct transitions that may not be clearly visible in conventional passive spectroscopy.[25]

Photoreflectance and Photomodulation Transmission

Photoreflectance (PR), as one of the modulation spectroscopy techniques, enables non-invasive investigation of optical transitions in semiconductor materials and structures. The modulation occurs through illumination of the sample with an additional light source, the so-called pump beam, which generates electron–hole pairs. These photogenerated carriers screen the existing electric field, causing a transient reduction of the band bending. As a result, the reflectance of the sample, probed by white light, is modulated. This effect, illustrated in Figure 2a, allows for the precise determination of the energy positions of optical transitions, their broadening, and other parameters of the band structure, since modulation occurs only at the energies corresponding to interband transitions.

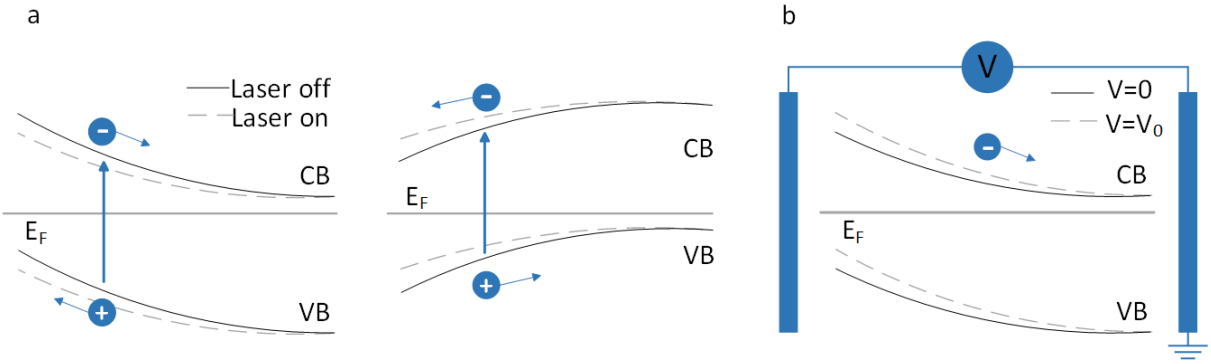

Figure 2. Band bending in photoreflectance for both n- and p-type materials (a) and electroreflectance (b) measurements.

In a typical photoreflectance setup (Figure 3), the pump beam is provided by a laser with a photon energy higher than the band gap of the investigated material. For TMDCs, commonly used pump wavelengths include 532 nm or 405 nm, which efficiently generate electron–hole pairs. Sub-band gap excitation is also possible, although it is a less common approach and requires careful tuning of the system due to the subtler signal response. Despite the use of spectral filters, the pump beam must be aligned such that its reflected light does not enter the monochromator slit, as its high intensity could interfere with the detection of the probe signal. Furthermore, the pump beam is modulated (i.e., periodically blocked and unblocked) using a mechanical chopper, typically at frequencies of several hundred hertz. These frequencies are chosen to be lower than the inverse of the carrier lifetime, ensuring that photogenerated carriers have sufficient time to recombine and the built-in electric field can recover before the next pump pulse. Simultaneously, the sample is illuminated with a probe beam, usually broadband light from a halogen lamp. The reflected probe light passes through a monochromator, which selects specific photon energies, and is then directed to a detector. Similar to reflection/transmission, depending on the spectral range of

interest, detectors are used either for the visible range or for the near-infrared region. The signal is analyzed using lock-in detection, which allows the modulated (AC) component to be extracted from the total (DC + AC) signal. This technique enables the detection of subtle changes in reflectance, resulting in characteristic resonance-like features at the energies of optical transitions. A closely related technique is photomodulated transmission, which differs only in the detection of transmitted light instead of reflected light. Consequently, the experimental setup requires slight modifications, illustrated in Figure 3b, to accommodate the transmitted beam path and corresponding alignment of optical components.[25,27,28]

The choice between reflectance and transmission measurements depends primarily on the optical thickness and transparency of the sample. Photoreflectance is particularly useful for thin films on solid substrates or multilayer structures, where transmission is not possible. It is sensitive to regions near the surface where built-in electric fields typically exist and is commonly used for epitaxial layers, heterostructures, and bulk materials. Photomodulated transmission, on the other hand, is preferred when the sample is sufficiently thin and semi-transparent over the spectral range of interest. It enables probing of the overall optical response through the sample thickness and is especially useful for monolayers, few-layer van der Waals crystals, and free-standing films.

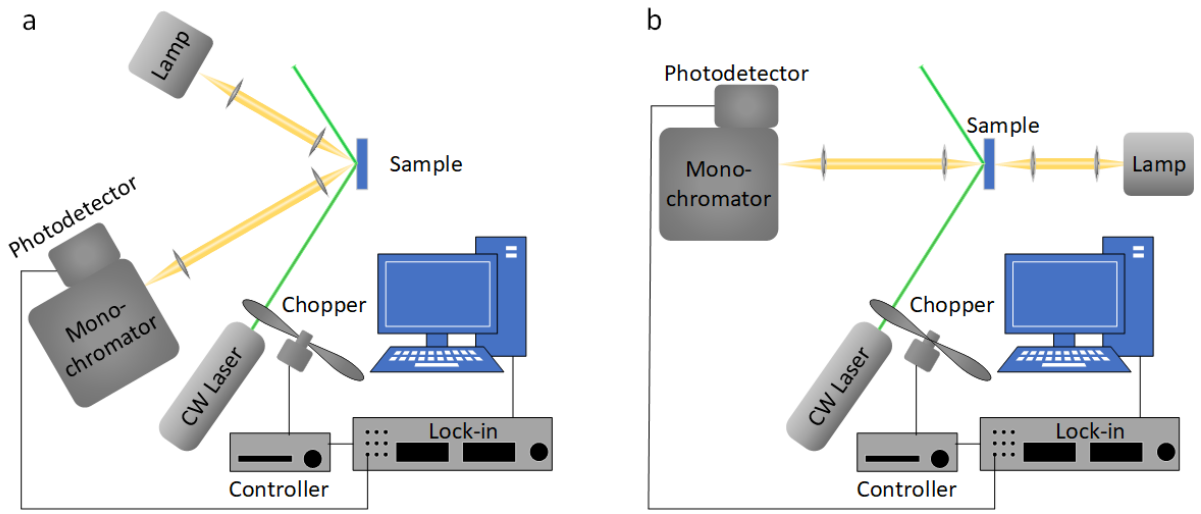

Figure 3. Schematic diagram of the system for measuring photoreflectance (a) and photomodulated transmission (b).

Contactless Electroreflectance

Another technique that utilizes the modulation of the internal electric field is electroreflectance. In this work, however, I focus on its contactless (CER) version, which is considered safer for the sample. In the CER technique, instead of illuminating the sample with an additional pump beam, it is placed in a capacitor-like setup, where an alternating voltage with a frequency of several hundred hertz is applied (Figure 4). One of the electrodes is an opaque solid substrate, to which the sample is attached using silver paste. The other electrode is a metal mesh that is transparent to light and separated from the sample by a narrow air gap. Together, they form a capacitor in which the applied electric field periodically redistributes charge carriers in the sample, which modifies the internal potential distribution and results in periodic perturbation of band bending.

(Figure 2b). This modulation of the internal electric field affects the reflectance near the absorption edge and at higher energies corresponding to critical points in the joint density of states. The resulting changes in reflectance are detected as a modulated optical signal (so-called resonances in the ΔR/R spectra), allowing for precise analysis of excitonic and band-to-band transitions. Unlike PR/PT with a pump beam, the ER or CER approach avoids the problem of PL signal overlap, which is particularly important when studying materials with strong emission.[25,27,28]

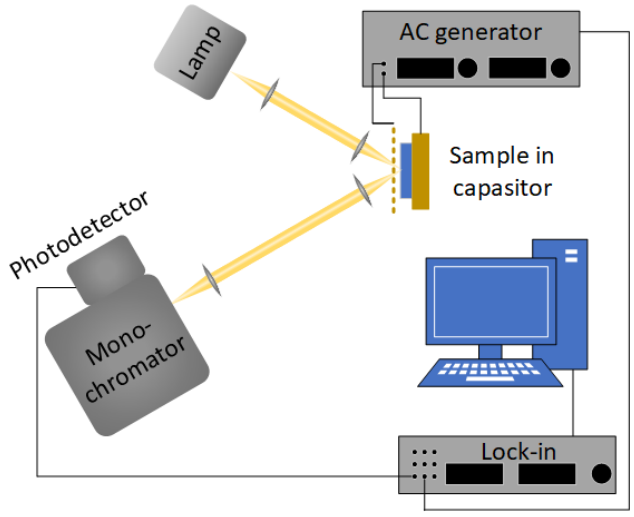

Figure 4. Schematic diagram of the system for measuring contactless electroreflectance.

Theory consideration

The theoretical background underlying all modulation techniques presented in this work is essentially the same, and can be conveniently introduced using the example of PR. The core idea of modulation spectroscopy is to periodically perturb certain parameters associated with the sample (such as the electric field in the case of PR or CER), which in turn induces small changes in its optical spectra. These changes arise primarily due to modifications in the imaginary part of the complex dielectric function, ε_2. From this perspective, the relative change in reflectance can be expressed as:

$$\frac{\Delta R}{R} = \alpha(\varepsilon_1, \varepsilon_2)\Delta\varepsilon_1 + \beta(\varepsilon_1, \varepsilon_2)\Delta\varepsilon_2 \tag{1.5}$$

where α and β are Seraphin coefficients that depend on the unperturbed dielectric function,[29] and $\Delta\varepsilon_1$ and $\Delta\varepsilon_2$ represent changes in the real and imaginary parts, respectively (Figure 5). Since ε_1 and ε_2 are intrinsicaly linked via the Kramers–Kronig relations, the measured changes in reflectance are also interdependent. These relations arise from the causality and analyticity of the material's optical response and allow one component of the dielectric function to be reconstructed from the other. This means that knowledge of either the real or imaginary part is sufficient to fully describe the material's complex dielectric response.

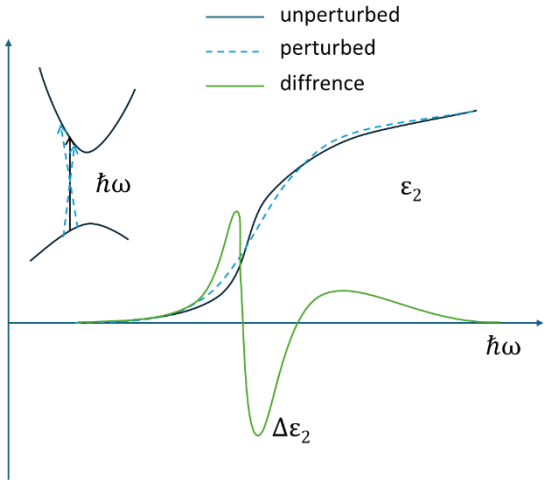

Figure 5. A band structure diagram illustrating the allowed optical transitions and the corresponding changes in the imaginary part of the dielectric function under perturbation of built-in electric field.[30]

The nature of the electro-optic effects observed in modulation spectroscopy also depends on the strength of the electric field applied to the sample.[30] This can be characterized by the electro-optic energy $\hbar\Omega$, defined as:

$$(\hbar\Omega) = \frac{q^2\hbar^2F^2}{2\mu} \tag{1.6}$$

where q is the elementary charge, $\hbar$ is the reduced Planck constant, F is the electric field strength, and μ is the reduced electron-hole effective mass along the field direction. In the weak-field regime, where $\hbar\Omega \leq \Gamma$ (with Γ denoting the broadening of the transition), the modulation induces small, perturbative changes in the dielectric function. In the intermediate field regime, where $\hbar\Omega \geq \Gamma$ but $qFa_0 \leq E_g$ (with a_0 being the lattice constant and E_g the band gap), more complex modifications of the band structure may occur. In strong electric fields, when $qFa_0 \approx E_g$ and $\hbar\Omega \geq \Gamma$, significant shifts of energy levels are observed due to the Franz–Keldysh or quantum-confined Stark effects.[26]

Moreover, the lineshape of the optical transition is commonly approximated by a Lorentzian function. While a Gaussian distribution may more accurately describe inhomogeneously broadened features, especially at elevated temperatures, a Lorentzian profile is typically sufficient for experimental fitting. Furthermore, in PR and CER spectroscopy, the perturbation of the complex dielectric function leads to changes in the energy position, broadening, and amplitude of the transitions, which are originally represented by lineshapes such as the Lorentzian. These modulated responses manifest as derivative-like features in the spectrum (see Figure 5). A standard approach to model the modulation spectrum is the so-called Aspnes third-derivative functional form, given by:

$$\frac{\Delta R}{R}(\mathrm{E}) = \mathrm{Re}\left[Ae^{i\theta}(\mathrm{E} - \mathrm{E}_0 + i\Gamma)^{-m}\right] \tag{1.7}$$

where θ is the phase factor, E_0 is the critical point energy, and m represents the type of optical transition. Specifically, m=2 corresponds to excitonic transitions, m=2.5 is typical for band-to-band transitions in bulk materials, and m=3 is characteristic of transitions in two-dimensional systems or in cases of significant inhomogeneous broadening.[26–28,30,31]

Thermoreflectance (TR) is a modulation spectroscopy technique that employs periodic temperature modulation to enhance the optical response of a material. By inducing small, controlled temperature oscillations and monitoring the resulting modulated reflectance, TR enables the sensitive detection of optical transitions. These transitions do not necessarily shift significantly with temperature; rather, their reflectance signal becomes detectable through lock-in amplification of the temperature-induced modulation. The experimental setup for thermoreflectance (Figure 6) is analogous to that used in photoreflectance (Figure 3a), with one key difference: the sample is mounted on a holder equipped with Ohmic contacts, and its temperature is modulated by passing a pulsed current through the sample, this is referred to as the direct heating approach. An alternative method involves indirect heating, in which the sample is placed in good thermal contact with a heated, thermally conductive substrate coated with a metallic layer, while silicone grease is applied to ensure efficient heat transfer. Regardless of the heating approach, in thermoreflectance methods the modulation originates from periodic temperature fluctuations, which induce thermal expansion and contraction of the lattice constants. These temperature-induced changes affect the electronic band structure of the material, specifically, they shift the band edge or, more generally, the energies of interband transitions. Unlike in PR and CER, temperature modulation in TR has a comparatively weaker influence on the amplitude and linewidth of transitions. However, the material's dielectric function is still modified, which in turn affects the reflectance R of the sample.[32–34]

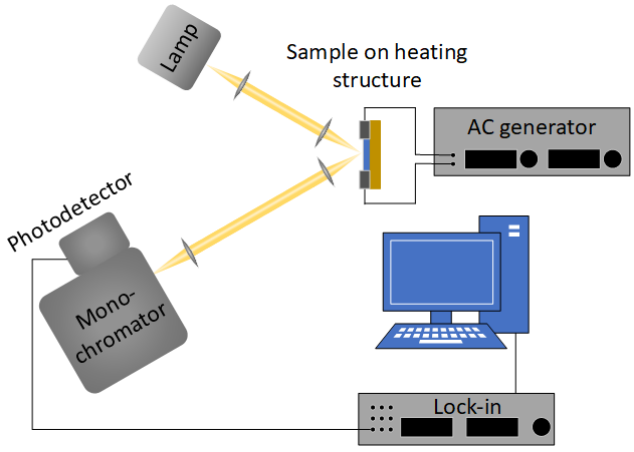

Figure 6. Schematic diagram of the system for measuring thermoreflectance.

As discussed earlier, these effects are experimentally measured as the relative change in reflectance, given by:

$$\frac{\Delta R}{R} = \frac{R(T+\Delta T)-R(T)}{R(T)} \tag{1.8}$$

where ΔT is the amplitude of the temperature modulation (i.e., the small periodic variation around the equilibrium temperature T), and $R(T)$ is the reflectance at equilibrium. The periodic temperature modulation acts as a perturbation that modifies lattice parameters (e.g., via thermal expansion) but preserves the overall crystal lattice periodicity. The resulting changes, primarily in the transition energy, are small compared to the transition energy itself, making this a first-order perturbation. In TR, the modulated reflectance signal is approximately proportional to the first derivative of the unperturbed dielectric function with respect to energy (Figure 7), whereas in

electromodulation techniques such as PR and CER, it is typically proportional to the third derivative (Figure 5).[28]

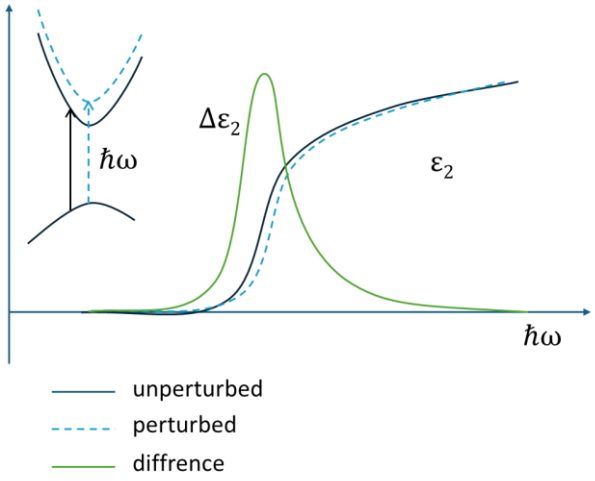

Figure 7. A band structure diagram illustrating the allowed optical transitions and the corresponding changes in the imaginary part of the dielectric function under perturbation of temperature.[30]

Photoluminescence

Photoluminescence (PL) is a form of emission spectroscopy in which a material emits light as a result of optical excitation. This method provides valuable insight into the electronic structure, excitonic properties, and defect states of semiconductors and other optoelectronic materials. The process begins when a photon, typically from a laser source and in the visible or ultraviolet spectral range (i.e., with energy above the band gap), is absorbed by the material. This absorption promotes an electron from the valence band to the conduction band, or from a lower to a higher electronic state, resulting in the formation of an electron–hole pair. Following excitation, the excited carriers undergo relaxation, during which they lose excess energy by interacting with lattice vibrations. These interactions with phonons bring the carriers to lower energy states within the conduction and valence bands. Once relaxed, the electron and hole may recombine radiatively, emitting a photon whose energy can correspond to the energy of, e.g., the bandgap. Moreover, the emitted light can originate from band-to-band recombination, excitonic transitions, or recombination processes involving localized states such as defects, impurities, or surface traps.[4,5]

The PL measurement setup shown in Figure 8 consists of a pump beam, typically provided by a laser, which is directed onto the sample under investigation. In the illustrated configuration, the emitted PL is collected and directed toward a spectrometer that simultaneously records the entire emission spectrum. To prevent the intense excitation laser light from reaching the detector and overwhelming the PL signal, a long-pass filter is placed in the optical path. This filter blocks wavelengths shorter than a specified cutoff, effectively suppressing the laser line and allowing only the longer-wavelength luminescence emission to pass through to the spectrometer.

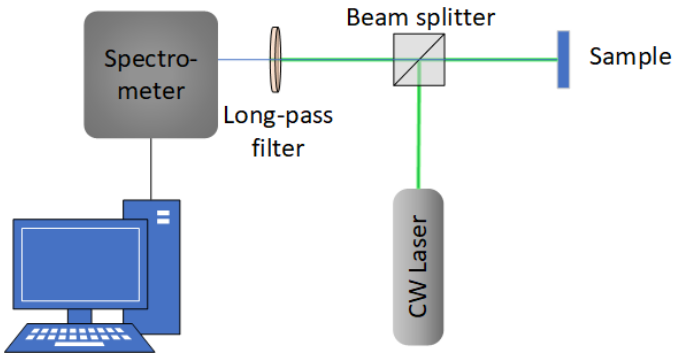

Figure 8. Schematic diagram of the system for measuring photoluminescence.

External stimuli

One part of this study involves applying external stimuli in the form of temperature to induce and characterize the evolution of the optical properties of layered materials. In this context, the major changes include shifts in the energies of optical transitions and narrowing of their linewidths, which also helps distinguish different interband transitions at low temperatures. The temperature dependence of the dielectric function ε reflects not only the shift in band gap energy $E_g(T)$ but also changes in the positions of individual bands contributing to different optical transitions. This behavior can be described using the Varshni equation:

$$E_g(T) = E_0 - \frac{\alpha T^2}{T+\beta} \tag{1.9}$$

where $E_g(T)$ is the transition energy at temperature T, E_0 is the energy at 0 K, and α is a material-specific coefficient that quantifies the strength of the band gap reduction with temperature related to electron–phonon coupling and thermal expansion effects; β is a parameter that can be interpreted as an effective temperature scale at which the band gap energy changes more rapidly. Alternatively, the Bose–Einstein model provides a more physically grounded description by explicitly incorporating exciton–phonon interactions:

$$E_g(T) = E_0 - \frac{a_B}{\exp\left(\frac{\theta_B}{T}\right)-1} \tag{1.10}$$

where a_B is a coupling constant that represents the strength of the exciton–phonon interaction, and θ_B is an effective phonon temperature and is related to the average energy of the phonons involved in the interaction. This model better captures the low-temperature behavior, where the phonon population follows Bose–Einstein statistics. It is particularly well-suited for materials with pronounced exciton–phonon coupling, such as 2D TMDCs.[4,35]

Broadening

The temperature dependence of the broadening of interband critical point transitions in semiconductors is commonly described using the Bose–Einstein statistical model:

$$\Gamma(T) = \Gamma_0 + \frac{\Gamma_{LO}}{\exp\left(\frac{\theta_{LO}}{T}\right)-1} \tag{1.11}$$

Where $\Gamma(T)$ is the temperature-dependent broadening (linewidth), Γ_0 is the inhomogeneous broadening at 0 K, Γ_{LO} reflects the strength of the exciton–phonon coupling, θ_{LO} is the effective phonon temperature, related to the average LO phonon energy, T is the absolute temperature. This expression, based on the Bose–Einstein distribution, captures the increase in linewidth with rising temperature due to the thermal occupation of optical phonon modes. The parameter θ_{LO} extracted from the fits reflects the dominant phonon modes interacting with electronic transitions, while Γ_{LO} quantifies the strength of this interaction. This formulation provides a microscopic description of exciton–phonon coupling effects and complements empirical models like the Varshni equation used for the temperature dependence of the transition energies.[36–38]

1.1. Investigated Materials

Semiconductors play a fundamental role in the technology of the modern world. Their unique properties form the basis of modern photonics and optoelectronics.[14,15,15,39] Technological advances are fueling a growing need for in-depth research into new classes of semiconductor materials, particularly 2D materials, which reveal increasingly complex mechanisms determining their optical and electronic properties. This doctoral dissertation examines selected semiconductor materials, particularly compounds from groups III-V and layered van der Waals crystals. These two groups represent distinct classes of materials, differing in their crystalline structure and bonding patterns, which translates into significant differences in their physical properties.

III-V Semiconductors

III–V semiconductors constitute a broad class of compounds formed by elements from group III and group V. Most of them crystallize in the zinc-blende structure[40] (e.g., arsenides and phosphides) or the wurtzite structure[41] (e.g., nitrides), shown in Figure 9. The crystal structure determines optical, mechanical, and transport properties, including their anisotropy, and, most importantly, the nature of the band structure.

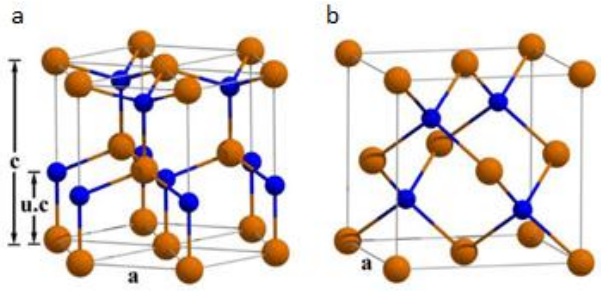

Figure 9. Two crystalline polymorphs of GaN: (a) wurtzite, (b) zinc-blende, Ga atoms are shown in brown and N in blue color.[42] Reproduced from Ref. 42 licensed under CC BY 4.0.

Many III–V semiconductors exhibit a direct fundamental band gap. In such a case, the maximum of the valence band and the minimum of the conduction band lie at the same point in reciprocal space (usually the Γ point), enabling, e.g., efficient radiative recombination of electrons and holes or strong light absorption. In some materials, such as AlAs or high-aluminum-content AlGaAs, the fundamental band gap becomes indirect, which suppresses radiative transitions and makes optical absorption less efficient due to the need for phonon assistance. Moreover, it is well known that the band gap energy and its nature (direct or indirect) depend strongly on chemical composition. In this context, it is useful to refer to a familiar diagram that shows the dependence of the band gap energy on the lattice constant for various III–V materials, as presented in Figure 10.[43] This graph represents an important aspect of material science: the continuous tuning of band gap energy by adjusting the composition of ternary compounds. Moreover, another crucial factor is the evolution of the electronic band structure with temperature, which affects the optical properties of materials. With increasing temperature, a systematic decrease in band gap is usually observed, due to electron–phonon interactions and thermal expansion of the crystal lattice. This behavior is commonly described empirically by the Varshni equation or the Bose-Einstein model. III–V semiconductors also exhibit low effective carrier masses and high mobility, especially for electrons, resulting from the curvature of the conduction band minimum in the band structure. The band structure also determines strong nonlinear optical responses, such as refractive index modulation, absorption modulation, and electro-optic effects. Furthermore, in the presence of an external electric field, phenomena such as the Franz–Keldysh effect (modification of the absorption edge) and the quantum-confined Stark effect (shift of optical transitions) can be observed.[39,43,44] III–V materials are grown using epitaxial techniques that allow for high-quality crystalline layers with controlled composition and thickness. The most commonly used methods are molecular beam epitaxy (MBE), metalorganic chemical vapor deposition (MOCVD), and hydride vapor phase epitaxy (HVPE). Each of these methods enables the growth of layers with different purity levels, growth rates, and compositional uniformity. Precise growth conditions are crucial to minimizing lattice defects that can significantly affect the material's optical and electrical properties.[43]

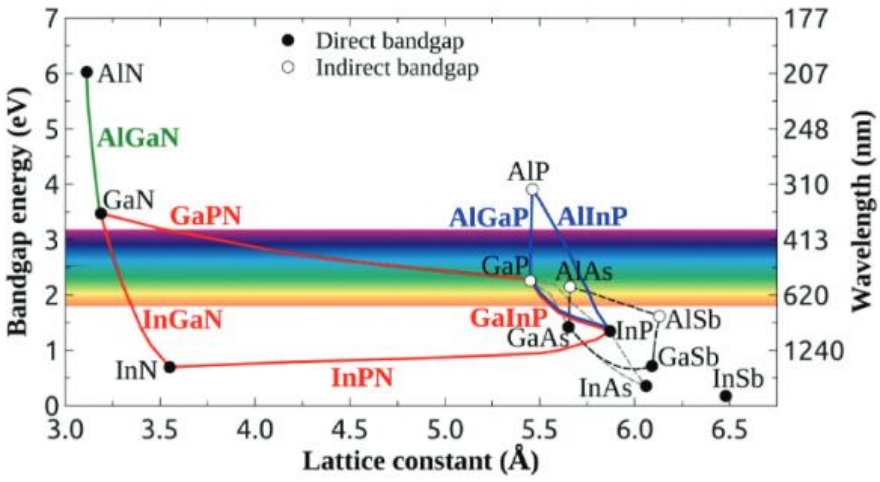

Figure 10. Band gap energy as a function of lattice constant for different III–V materials. Black solid dots represent direct band gap materials, and white dots represent indirect band gap materials.[39] Reproduced from Ref. 39, licensed under CC BY 4.0.

Van der Waals (vdW) crystals are a group of materials with a characteristic layered structure, in which atoms within a single layer are bound by strong covalent bonds, while adjacent layers are held together by much weaker, non-directional van der Waals forces.[10] This unique structure allows for easy separation (exfoliation) of individual layers down to the level of a single monolayer. The anisotropy in bond strength initiated the dynamic development of 2D materials, pioneered by graphene, i.e., a monolayer of carbon atoms arranged in a honeycomb lattice, first isolated in 2004 by Novoselov and Geim.[45] 2D materials are defined as structures with a thickness of one or a few atomic layer, where charge carriers are confined to two dimensions. The layered nature of vdW crystals leads to remarkable optical anisotropy, stemming from the fundamental difference between strong in-plane covalent bonding and weak interlayer interactions.[46] Furthermore, van der Waals materials display a wide range of physical properties – from insulators (hexagonal boron nitride, h-BN), through semiconductors (TMDCs), to metals and superconductors ($NbSe_2$).[47,48] Accordingly, their band gaps span from ~6 eV in h-BN, through 1–2.5 eV in TMDCs, down to the gapless graphene, as shown in Figure 11. Such diversity has led to broad applications in fields such as nanotechnology, optoelectronics, spintronics, and correlated electron systems. Thanks to the absence of dangling bonds on their surfaces, these materials can be stacked into vdW heterostructures – systems built from different 2D materials that preserve their individual layer properties but exhibit new phenomena due to interlayer interactions.[10,49] The mechanical and chemical stability of many vdW crystals, as well as the ability to precisely control the number of layers and their relative orientation, enables sophisticated tailoring of their properties. Consequently, vdW materials are regarded as a promising platform for future quantum devices and post-silicon electronics, including next-generation transparent and flexible systems.[50]

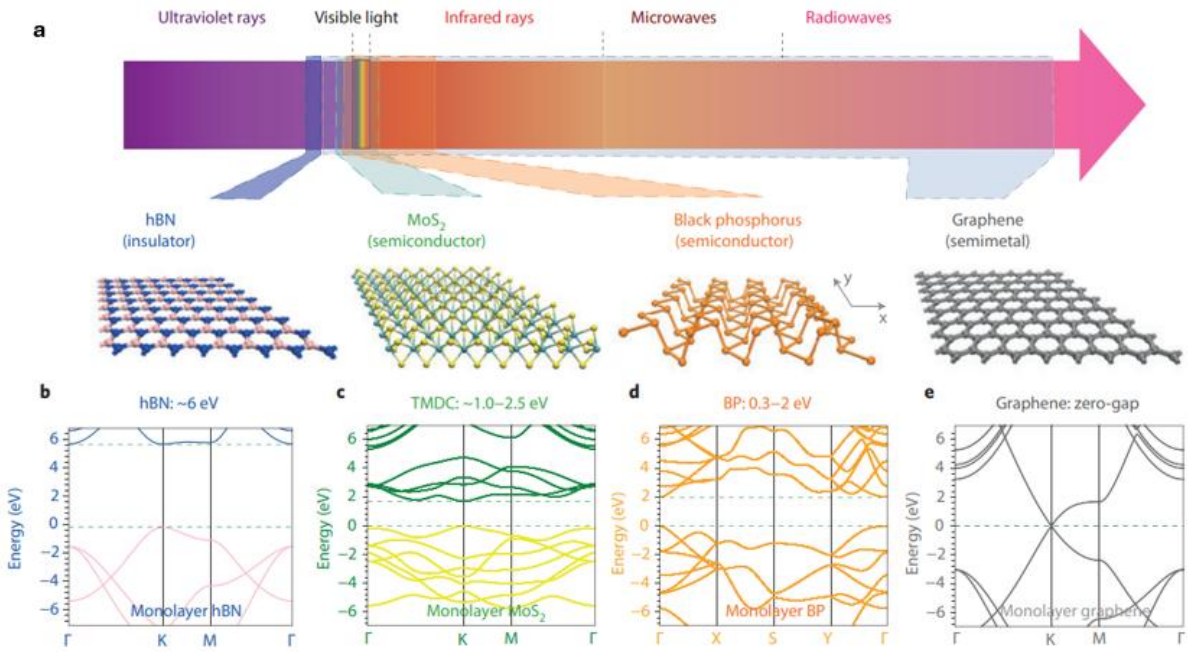

Figure 11. Electronic band structure in 2D materials. [48] Reproduced from ref. 48 with permission from Springer Nature.

Transition Metal Dichalcogenides

TMDCs, with the general formula MX_2, where M is a transition metal (e.g., Mo, W) and X is a chalcogen element (S, Se, Te), form layered crystal structures exhibiting a range of unusual optical and electronic properties in the 2D limit.[47] In Figure 12a, in the periodic table, elements from these groups are marked in green (transition metals) and orange (chalcogens). The fundamental structural unit of TMDCs is a so-called "trilayer", in which the transition metal atoms are sandwiched between two layers of chalcogen atoms. A single such trilayer corresponds to what is commonly referred to as a monolayer, with a typical thickness of approximately 0.7 nm.[47,51] In the most commonly encountered 2H (hexagonal) structure, the metal exhibits trigonal prismatic coordination, each metal atom is surrounded by six chalcogen atoms arranged in a geometry resembling a triangular prism. Within a single layer, strong covalent bonds dominate, while adjacent layers are held together by weak vdW interactions, enabling exfoliation down to monolayers (Figure 12b).

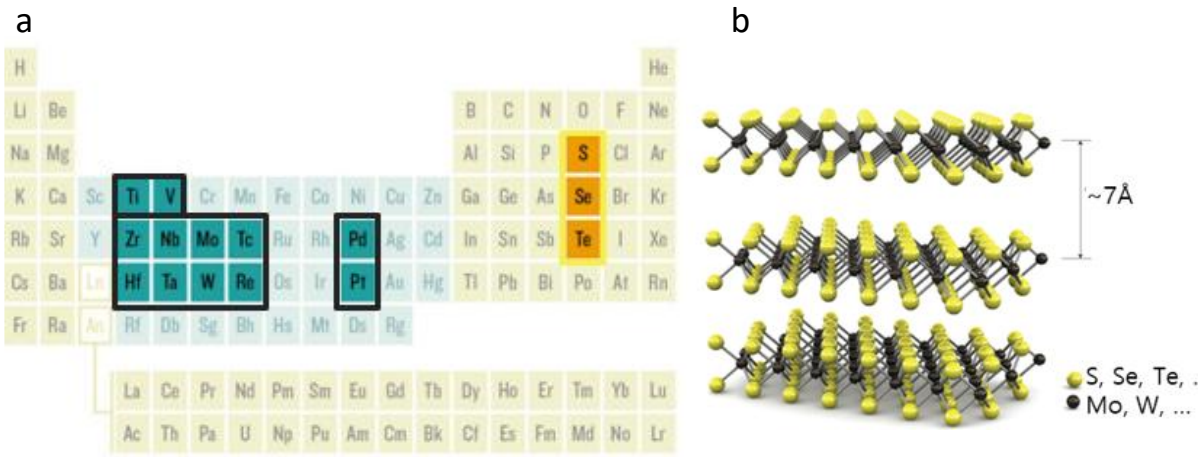

Figure 12. Periodic table with transition metals (green) and chalcogens (orange) forming TMDCs marked (a), and Schematic of a TMDC layer in the 2H phase, showing a structure with a transition metal atom sandwiched between two chalcogen layers (b).[81]

In bulk form, most TMDCs are indirect band gap semiconductors, the valence band maximum is located at the Γ point, while the conduction band minimum lies at the Q point or between Γ and K. As the number of layers is reduced to one, a fundamental band structure transition occurs: both the valence band maximum and conduction band minimum shift to the K (and K') points in the Brillouin zone, resulting in a transition from an indirect to a direct band gap (Figure 13a). This mechanism is attributed to the reduction of interlayer interactions and to the different thickness dependencies of the energy positions of individual bands. As a result, monolayer TMDCs exhibit significantly enhanced PL, up to two orders of magnitude stronger than their bulk counterparts.[52]

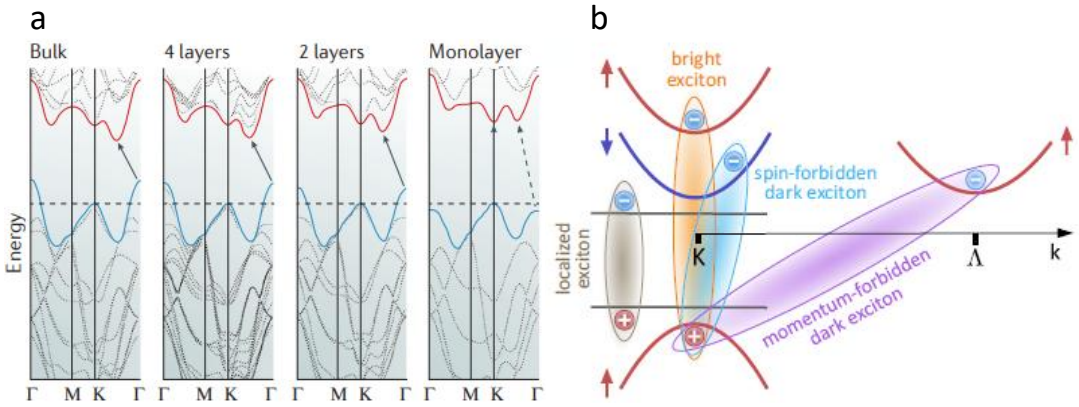

Figure 13. Change of band gap from indirect to direct as a function of layer number in MoS_2. In the bulk, the valence band maximum lies at the Γ point and the conduction band minimum at the Q point (or between Γ and K), resulting in an indirect band gap. As the number of layers decreases, interlayer interaction is reduced, and the band structure evolves. In a monolayer, both the conduction band minimum and valence band maximum are located at the K point, leading to a direct band gap.[47] Reproduced from ref. 47 with permission from Springer Nature. (a) Momentum-forbidden dark excitons have electrons and holes in different momentum-space valleys, while spin-forbidden dark excitons have opposite spins. Localized excitons are trapped by impurity-induced potentials.[53] Reproduced from Ref. 53, licensed under CC BY 4.0. (b)

Despite their atomically thin structure, TMDC monolayers display exceptionally strong light absorption, reaching up to 20% in the visible range, due to the strong coupling of light with excitonic transitions. The main absorption resonances are associated with the A and B excitons, which result from the spin–orbit coupling-induced splitting of the valence band. Since optical transitions between the valence and conduction bands are spin-conserving, this splitting gives rise to two well-separated interband optical transitions, identified as A (originating from the upper valence band) and B (from the lower valence band). This leads to distinct excitonic features in both absorption and PL spectra, which are particularly prominent in monolayer TMDCs.[52]

Moreover, in monolayers, exciton-related phenomena dominate the optical response. This stems from limited dielectric screening and strong quantum confinement, leading to a high exciton binding energy on the order of 0.5–0.7 eV, ensuring exciton stability at room temperature. In addition to neutral excitons, trions (charged excitons), biexcitons, and, within heterostructures, interlayer excitons (where the electron and hole reside in different layers) are observed. These interlayer excitons exhibit longer lifetimes and lower recombination energies. TMDC PL spectra often show multiple excitonic features, which reflect local potential fluctuations, compositional inhomogeneities, defects, and many-body interactions. At the K and K' points of the Brillouin zone, strong spin–orbit coupling leads to valence band splitting (especially pronounced in $MoSe_2$ and WS_2), resulting in, as already mentioned, the emergence of two exciton types: A and B. Depending on the spin and momentum configuration of the electron and hole, excitons can be classified as bright or dark, only the former couple efficiently to light and contribute directly to photoluminescence. In contrast, dark excitons remain optically inactive under direct excitation (Figure 14b). In addition, owing to the lack of inversion symmetry and the time-reversal degeneracy of the K and K' valleys, it is possible to selectively excite excitons in a specific valley using circularly polarized light. This effect, known as valley polarization, lies the foundation for the emerging field of valleytronics, where information is encoded not only in charge and spin but also in momentum-space location.[11,52]

Using the CVD technique, it is also possible to create multicomponent TMDC alloys, such as $Mo_{1-x}W_xS_2$ or $MoS_{2(1-x)}Se_{2(x)}$, enabling continuous tuning of the band gap, band structure, and excitonic resonances. Introducing a second metal or chalcogen induces nanoscale potential fluctuations, which can induce partial exciton localization. This localization may manifest as substructures in the PL and alter carrier recombination dynamics. In this case, the PL peak position often shows an S-shaped dependence on temperature, due to a competition between thermal band gap shrinkage and thermal redistribution of excitons among local potential minima associated with defects or strain. These effects are particularly pronounced in alloys and monolayers, where compositional inhomogeneities create an energy landscape conducive to carrier trapping.[54–57] Alloys also allow tailoring of material properties for specific applications, for example, in designing heterojunctions with desired band alignments (straddling, staggered, or broken gap), which are crucial for efficient optoelectronic device performance.[58,59]

Moreover, TMDCs find widespread applications in nanotechnology and photonics. Thanks to the combination of direct band gap, high absorption, mechanical flexibility, and compatibility with photonic platforms, they are used as active materials in photodetectors, nanoscale lasers, light modulators, as well as in spintronic and valleytronic devices. Their atomic thickness and the ability to precisely engineer their properties (via strain, electric field, or doping) also make them attractive candidates for future 2D electronics and neuromorphic computing.[54]

Top-down methods for obtaining thin layers of van der Waals crystals

As already mentioned, layered materials owe their unique properties to the anisotropic nature of their chemical bonding. While atoms within each layer are tightly bound by strong covalent bonds, the interaction between adjacent layers is much weaker (up to a thousand times weaker) and governed by vdW forces. This bonding scheme, illustrated schematically for graphene in Figure 14, is a defining feature of layered crystals. It enables the use of mechanical exfoliation techniques to isolate individual atomic layers, opening the door to the study of exotic physical phenomena in two-dimensional systems. The resulting vdW surfaces are essentially free of dangling bonds and exhibit exceptional stability under ambient conditions.[60]

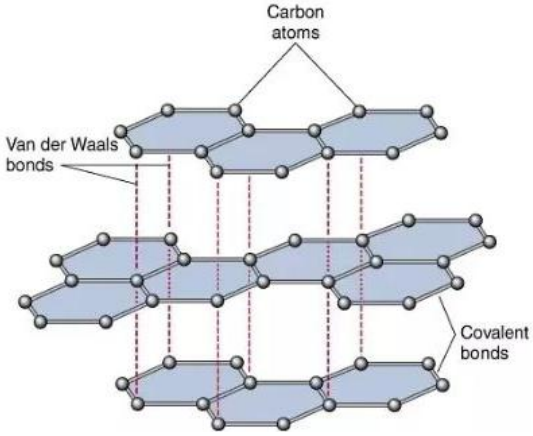

Figure 14. Layered graphene structure with schematically marked van der Waals and covalent bonds.[52]

Mechanical exfoliation was already known in the 90s, however, it was Andre Geim and Konstantin Novoselov who first successfully obtained a single layer of graphene using this method.[45] For this groundbreaking achievement, they were awarded the Nobel Prize in Physics in 2010. Today, this

technique is used not only for isolating graphene but also for obtaining monolayers of other layered materials, such as TMDC,[61] hexagonal boron nitride,[62] black phosphorus,[63] and various metal oxides.[64] The method involves mechanically separating thin layers from a bulk crystal using adhesive tape, most commonly Scotch or Nitto tape. The process typically requires repeated exfoliation until monolayers or flakes of the desired thickness are obtained. The exfoliated material is then transferred onto a flexible substrate, typically polydimethylsiloxane (PDMS),[65] from which it can be further transferred onto the target structure. The individual steps of the exfoliation process are illustrated in Figure 15.

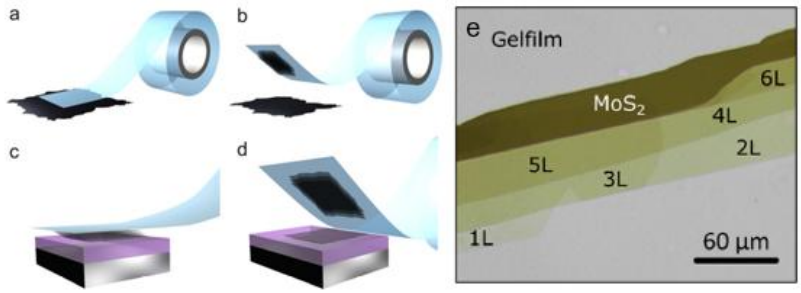

Figure 15. Schematic representation of the mechanical exfoliation process. A bulk crystal is repeatedly cleaved using adhesive tape to produce thin flakes (a,b). Selected flakes are then transferred onto a flexible substrate, usually PDMS (c), and the tape is then detached from the PDMS (d).[65] Reproduced from Ref. 66, licensed under CC BY 4.0. Microscopic image of exfoliated MoS_2 showing stepped layers from monolayer to bulk (e).[16] Reproduced from Ref. 16, licensed under CC BY 4.0.

Although dry exfoliation allows for obtaining good-quality flakes, they are limited in scale, usually reaching sizes of several dozen to several hundred micrometers. In addition to classical mechanical exfoliation, other methods are also widely used in studies on layered materials, such as wet, chemical, and electrochemical exfoliation.[66,67]

Liquid-phase exfoliation is a widely used technique for obtaining 2D materials from their bulk counterparts. The process involves suspending the bulk crystal in a suitable solvent such as N-methyl-2-pyrrolidone (NMP), N,N-dimethylformamide (DMF), or isopropanol (IPA) and applying ultrasonic energy to overcome the interlayer forces. The key mechanism enabling exfoliation is the weakening of interlayer van der Waals interactions, particularly London dispersion forces, in the presence of a liquid medium. In a liquid environment, the potential energy between adjacent layers is significantly reduced compared to vacuum (air) conditions, making delamination easier. Optimal exfoliation efficiency is achieved when the surface tension of the solvent closely matches that of the target material.[66] After sonication, the resulting suspensions are typically centrifuged to remove unexfoliated material.[68]

Chemical exfoliation, also referred to as intercalation exfoliation, involves overcoming interlayer adhesion by introducing appropriate molecules between the layers of the material. This process weakens the van der Waals forces responsible for maintaining structural cohesion and enables the separation of atomic layers. A key role is played by the effects following intercalation, such as increased interlayer spacing, gas release, or energetically favorable solvation, a process in which dissolved molecules are surrounded by solvent molecules. This solvation helps prevent the exfoliated flakes from reaggregating.[69,70]

Electrochemical exfoliation involves introducing ions (e.g., alkali metal ions or protons) between the layers of a material through electrochemical reactions in a controlled setup. This process is carried out in an electrochemical cell consisting of three electrodes: a working electrode (WE), which is made of the exfoliated material (e.g., graphite or MoS_2), a counter electrode (CE), typically a platinum wire, and a reference electrode (e.g., Ag/AgCl), all immersed in an electrolyte containing ions capable of intercalation. Depending on the applied potential, cation intercalation (e.g., Li^+, THA^+, TBA^+) occurs under a positive potential (when the exfoliated material acts as the cathode), while anion intercalation (e.g., SO_4^{2-}, NO_3^-, PF_6^-) occurs under a negative potential (when the material acts as the anode). As ions enter the interlayer spaces, the van der Waals forces are weakened, facilitating the separation of individual atomic layers. Additional processes such as gas evolution (e.g., hydrogen release) may also occur, and sonication is often applied to improve exfoliation efficiency. The resulting suspensions can be centrifuged and used for further applications. Figure 16 below illustrates both anodic (anion-based) and cathodic (cation-based) electrochemical exfoliation routes, as well as how they lead to the formation of exfoliated 2D nanosheets.[66,67,71]

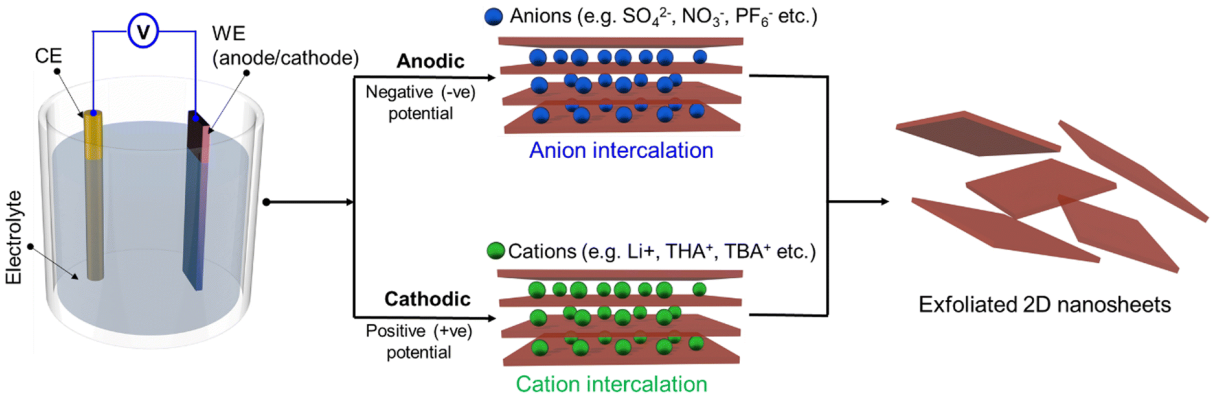

Figure 16. Schematic diagram of electrochemical exfoliation of van der Waals crystals with representation of anions and cations.[67] Reproduced from Ref. 68, licensed under Creative Commons Attribution-NonCommercial 3.0 Unported Licence.

Bottom-up growth technique

In contrast to the previously discussed exfoliation techniques, which rely on the separation of existing layers from bulk materials, chemical vapor deposition (CVD) is a growth technique that enables the synthesis of thin layers directly on a substrate. It is one of the most widely used methods for obtaining thin films of TMDCs, such as MoS_2, WS_2, and their alloys. The CVD process involves the reaction of gaseous or sublimed precursors at elevated temperatures, resulting in the deposition of a thin layer of the target material on a heated substrate. A typical setup includes a tube furnace with a heating zone containing a metal precursor (e.g., MoO_3 or WO_3), a source of sulfur or selenium in powder form, and a carrier gas that transports the reactants to the growth zone. Through precise control of process parameters like temperature, precursor concentration, pressure, and substrate type, it is possible to synthesize large-area monolayers of TMDCs with high crystalline quality. The resulting domains typically exhibit regular hexagonal or triangular shapes and uniform thickness, making CVD particularly attractive for both fundamental research and industrial applications, where scalable production of uniform and high-quality monolayers is essential.[72,73]

2D materials reveal a wide range of physical,[74] optical,[75] and mechanical[13] properties, which can be further tailored and expanded by constructing heterostructures, enabling even multifunctional behavior. Two main types of heterostructures are considered: in-plane and vertical (out-of-plane) arrangements. For better illustration, vertical structures are often compared to stacking LEGO blocks, whereas in-plane heterostructures resemble assembling puzzle pieces (Figure 17). Strong covalent bonds ensure in-layer stability, while van der Waals-like forces are sufficient to keep the layers stacked together.[76] The most popular techniques for constructing such heterostructures include direct synthesis via CVD or mechanical exfoliation and transfer (Figure 18). Van der Waals heterostructures allow for the combination of various 2D materials, such as TMDCs, graphene, or h-BN, without the need for lattice matching.[10] A key aspect is that layers are held together by van der Waals forces, which minimize strain arising from differences in their crystal lattice parameters. From a physical point of view, each layer retains its own band structure, but in the strong-coupling regime, hybridization of electronic states can occur, and adjacent layers can induce electrostatic potential tuning.[77]

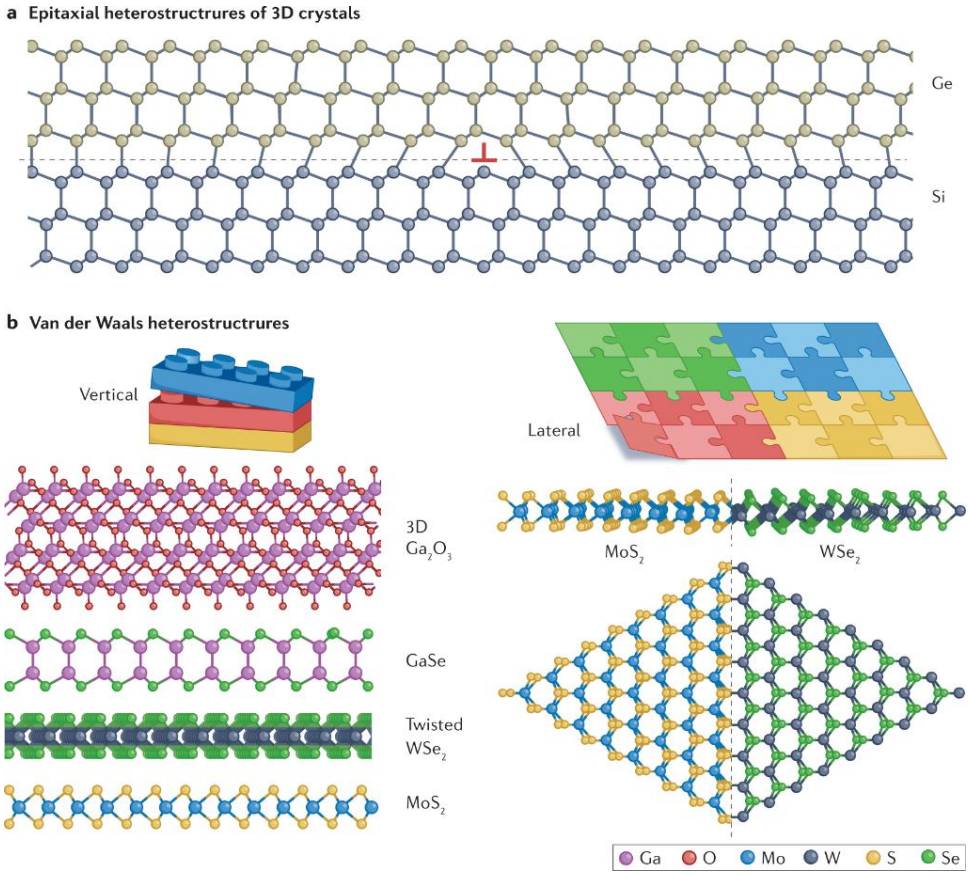

Figure 17. Vertical and lateral van der Waals heterostructures. Vertical stacking resembles LEGO blocks due to its layered construction, while lateral heterostructures resemble puzzle pieces, reflecting the edge-to-edge joining of materials.[76] Reproduced from ref. 77 with permission from Springer Nature.

The electronic properties of heterostructures can also be tuned by twistronics, i.e., changing the relative twist angle between layers. At small twist angles, a moiré superlattice forms, leading to the formation of minibands and strong modulation of the potential in real space. This, in turn, causes localization of electrons and holes in regions with a specific atomic registry, effectively

forming moiré traps.[78] Interlayer interactions involve not only classical van der Waals forces but also interlayer charge transfer, band offset engineering, and the formation of hybrid states. For instance, in type-II heterostructures (e.g., $MoSe_2/WSe_2$), the conduction and valence bands are offset relative to each other, which facilitates charge separation - electrons localize in one layer and holes in another. This leads to the formation of interlayer excitons, where the wavefunction is spatially separated.[79] As a result, their lifetimes can reach nanoseconds, in contrast to picoseconds for intralayer excitons.[80,81] The dielectric environment and differences in the effective masses of carriers also play a key role in shaping the spatial distribution and binding energy of excitons, leading to effects such as band renormalization and shifts of optical resonance energies. [65]

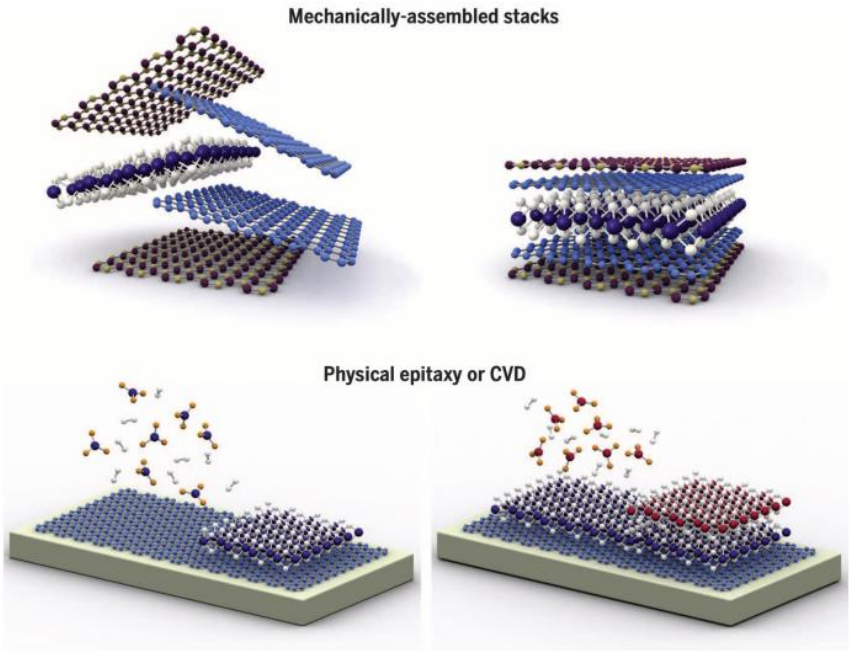

Figure 18. Schematic illustration of heterostructure fabrication methods. The top part shows mechanically assembled stacks, while the bottom part presents structures grown via physical epitaxy and CVD. From Novoselov, K. S., Mishchenko, A., Carvalho, A. & Castro Neto, A. H. 2D materials and van der Waals heterostructures. *Science* **353**, aac9439 (2016). Reprinted with permission from AAAS.[10]

Van der Waals heterostructures find application in advanced optoelectronic and quantum devices.[82,83] Specifically, thanks to precise control over their composition and layer configuration, they are used in photodetectors,[23] light emitters,[21] optical modulators,[84] field-effect transistors,[85] and non-volatile memory devices.[86] Of particular interest are their interlayer excitonic properties, enabling the development of optoelectronic elements with extended carrier lifetimes, as well as in spintronic and valeytronic devices that exploit additional particle degrees of freedom (spin, valley).[87] Moiré heterostructures are also promising platforms for realizing artificial quantum lattices and for simulating strongly correlated materials.[88]

1.2. Lab-on-fiber: Light-matter interaction in miniaturized optical systems and TMDC applications

An optical fiber is a dielectric waveguide structure that enables light propagation through the phenomenon of total internal reflection at the boundary between the core and the cladding – two

layers with carefully selected refractive indices. Light travels along the fiber in the form of so-called propagation modes, which are stable distributions of the electromagnetic field. The number and nature of these modes depend on the core diameter, the wavelength, and the refractive index contrast. Single-mode fibers support only one fundamental mode, ensuring high stability and minimal pulse broadening. In contrast, multimode fibers allow the simultaneous propagation of multiple modes, increasing the information-carrying capacity but introducing greater dispersion.[1] Understanding modal properties is crucial in designing optical sensors, filtering elements, resonators, and spectroscopic systems.

Although optical fibers are most commonly associated with telecommunications and long-distance signal transmission,[89] their application potential is much broader. In modern photonics, optical fibers can serve as passive light guides or as active components of optical systems. This diversity stems from the possibility of modifying their geometry, material properties, and structure. Fibers exist not only in the classical cylindrical form but also as D-shaped structures,[90] waveguides,[91] or photonic crystal fibers with modified cores.[92] The fiber end can also be functionally modified: tapered tips act as focusing lenses,[93,94] angled cleaves reduce back reflections (important, for example, in lasers or sensors),[95] and spherical ends are used in focusing systems and optical traps.[96] The fiber core itself can undergo various mechanical and optical modifications: side polishing enables coupling of waves with the environment,[97,98] micro- and macro-bending allow for selective wavelength filtering,[99,100] and tapering alters propagation conditions and facilitates light coupling with other structures.[101] There are also hollow-core fibers, where light is guided through an empty space filled with gas or vacuum, reducing losses and enabling unique optical interactions.[102,103] A special case is fiber Bragg gratings, formed by periodic changes in the refractive index along the fiber core. These structures reflect selected wavelengths and are widely used in temperature and strain sensors, as well as in selective components in lasers and optical filters.[104]

Beyond their passive function, optical fibers can also serve as active components. Examples include fibers doped with rare-earth ions, such as erbium or ytterbium, which enable light amplification or laser emission.[105] Nonlinear fibers, exploiting higher-order optical effects, are used for supercontinuum generation and oscillators.[106,107] This wide variety of modifications and functions has given rise to a new research trend in which the fiber is no longer just a passive carrier but becomes a functional measurement element. This led to the emergence of the lab-on-fiber concept, miniaturized analytical systems in which the optical fiber simultaneously functions as a transmission medium, a coupling element, and an active sensor or spectroscopic platform. In each application, the fiber acts as a versatile platform for conducting spectroscopic, chemical, biological, or nonlinear photonics research. Moreover, in certain experimental configurations, lab-on-fiber (LOF) technology can also replace conventional optomechanical components, offering compactness, stability, and enhanced integration with fiber-based systems (Figure 19).[3,6,108,109]

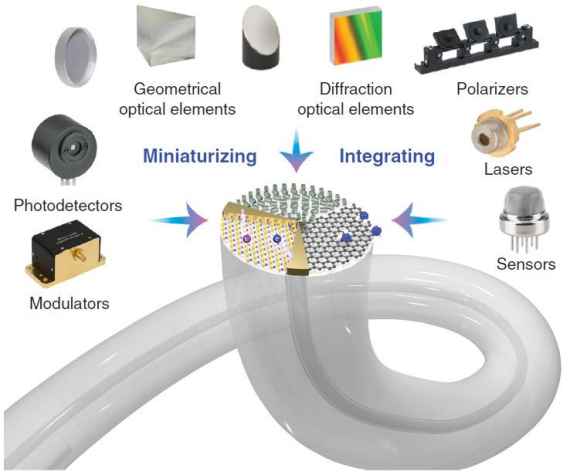

Figure 19. Representative configurations for integrating and miniaturizing components on the optical fiber tip.[6] Reproduced from Ref. 6, licensed under CC BY 4.0.

The physical operation of LOF systems is based on the interaction of the electromagnetic field of light propagating in the fiber with media located in the immediate vicinity of the core. Of key importance is the phenomenon of the evanescent wave – the optical field that "leaks" beyond the fiber core and allows coupling with a material placed on its surface or nearby. This makes it possible to detect changes in refractive index, absorption, or nonlinear properties without breaking the continuity of the fiber. Light–matter interaction in such systems enables highly sensitive probing of local optical properties, which can be applied in absorption, plasmonic, and Raman spectroscopy.[110] There are many methods for manufacturing such devices, as shown in Figure 20.

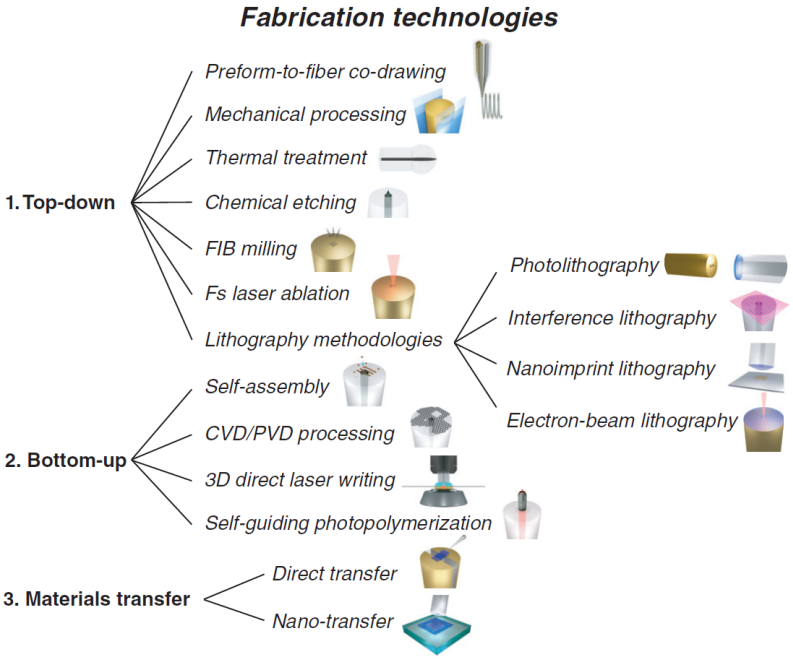

Figure 20. Overview of fabrication technologies for LOF platforms, categorized into tree main approaches: (1) top-down methods (e.g., laser ablation, focused ion beam milling, lithography), (2) bottom-up techniques (e.g., self-assembly, CVD/PVD processing, 3D direct laser writing), and (3) material transfer strategies (direct and nano-transfer). These methods enable the integration and miniaturization of functional elements on the end face of optical fibers.[6] Reproduced from Ref. 6, licensed under CC BY 4.0.

In recent years, particular attention has been paid to the integration of optical fibers with 2D materials, especially graphene and TMDCs, such as MoS_2 or WS_2.[111,112] Their integration with the fiber tip creates unique conditions for studying light–matter interactions on the nanometer scale, with high spectral and temporal sensitivity. The placement of materials on the fiber is usually achieved via CVD/PVD techniques or deterministic transfer.[6] When light propagating through the fiber reach a functionalized tip covered with a TMDC layer, direct interaction occurs between the optical wave and excitons or other excitations in the material. This coupling can occur via evanescent wave interaction or direct transmission through the material, depending on the system geometry (Figure 21).[109]

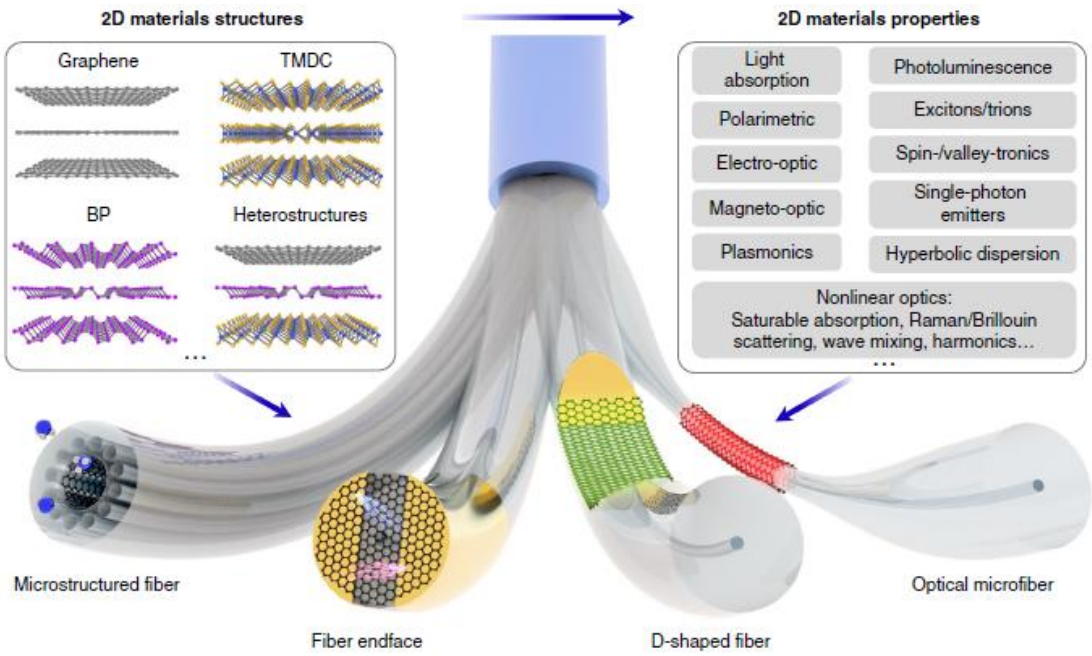

Figure 21. Schematic representation of the integration of 2D materials (e.g., graphene, TMDCs, black phosphorus, and heterostructures) with various types of optical fibers, including microstructured, end face-functionalized, D-shaped, and microfibers. The unique optical, electronic, and nonlinear properties of 2D materials, such as light absorption, PL, exciton dynamics, and nonlinear interactions, enable a broad range of fiber-integrated photonic functionalities.[7] Reproduced from Ref. 6, licensed under CC BY 4.0.

This configuration, i.e., a fiber with layered materials on top, enables, among other things, precise measurements of transmission changes as a function of temperature, allowing for monitoring of band gap shifts and other quantum effects in 2D systems. In the case of tapered or D-shaped fibers, a significant portion of the propagating field can be coupled to the material surface.[7] Thanks to their versatility and ability to operate under cryogenic conditions, high vacuum, or chemically aggressive environments, LOF systems are used not only in biological and chemical sensors but also in fundamental studies of modern materials.[113–115]

Integrating optical fibers with TMDC layers opens up new experimental possibilities in environments where traditional optical systems would be impractical due to their size, fragility, or sensitivity to external disturbances. Despite the dielectric nature of silica-based fibers, which limits direct integration of electrical functionality, hybrid systems combining fibers with electrodes and 2D materials, such as graphene or MoS_2, have already been demonstrated. These include fiber-integrated nanoelectromechanical system (NEMS)[116] devices and

photodetectors,[112] as well as laser systems in which graphene serves as a saturable absorber.[22] Moreover, light propagating through the fiber can be efficiently modulated by various external stimuli, including electric or magnetic fields, temperature changes, mechanical deformation, or interaction with other optical fields. The small core size and the ability to tailor the fiber's geometry enhance light–matter interactions, positioning optical fibers as a highly versatile platform for building miniaturized modulators, sensors, and laser sources. With the development of electrode deposition techniques on fiber tips, it is now possible to design electro-optic and thermo-optic modulators.[6]

The use of optical fibers enabled the development of measurement techniques employed in our research group, leading to increased precision and the expansion of studies on monolayers and heterostructures. The implementation of a fiber-compatible setup, along with temperature-controlled measurements, allowed for more versatile and sensitive analyses. Although this area still offers ample opportunities for further development, in the following sections, we present the results already achieved through these advancements.

2. Scientific Articles

The following part of the dissertation consists of four peer-reviewed scientific articles that constitute the core of the research conducted during the doctoral studies. Each article presents experimental studies on the optical properties of 2D materials, in particular TMDCs, using advanced fiber-based spectroscopy techniques developed and implemented as the main part of this work.

The articles are included in their published or accepted form, without modification. Before each article, a short section describes the author's specific contribution to the work, highlighting the scope of individual involvement in the design, execution, analysis, and authorship of the study.

Together, the four articles provide a coherent and multifaceted insight into the use of fiber-integrated systems for optical spectroscopy of 2D materials. The studies cover modulation techniques such as PR and CER, PL, thermotransmittance, conventional absorption spectroscopy, and demonstrate how optical fibers can enhance experimental control and precision in cryogenic and variable-temperature conditions.

2.1. Optical fiber-enhanced photoreflectance and contactless electroreflectance measurements of van der Waals crystals and III-V semiconductor materials

Citation:

Published in *Measurement*, Volume 253, Part C, 1 September 2025, 117678,

DOI: 10.1016/j.measurement.2025.117678

Co-authors:

Karolina Ciesiołkiewicz, Jan Kopaczek, Szymon J. Zelewski, Robert Kudrawiec

Author's contribution:

Karolina Ciesiołkiewicz designed the optical setup and built the complete measurement system, conducted all measurements, including photoreflectance and contactless electroreflectance, collected and analyzed the data, prepared the figures and graphical representations of the results, developed the interpretation of the results, wrote the manuscript, and served as the corresponding author.

Context within the dissertation:

This article constitutes a foundational experimental component of the dissertation. It presents the development and demonstration of an innovative optical fiber-based system for modulation spectroscopy. The approach enabled the integration of photoreflectance and contactless electroreflectance techniques with van der Waals crystals and conventional III-V semiconductors. The results and methodology introduced here laid the groundwork for the subsequent fiber-based studies presented in later articles.

Measurement 253 (2025) 117678

Contents lists available at ScienceDirect

Measurement

journal homepage: www.elsevier.com/locate/measurement

Optical fiber-enhanced photoreflectance and contactless electroreflectance measurements of van der Waals crystals and III-V semiconductor materials

K. Ciesiołkiewicz *, J. Kopaczek, S.J. Zelewski, R. Kudrawiec

Department of Semiconductor Materials Engineering, Wroclaw University of Science and Technology, Wybrzeże Wyspiańskiego 27, 50-370 Wrocław, Poland

ARTICLE INFO

Keywords:
Optical spectroscopy
Optical fiber
Photoreflectance
Contactless electroreflectance
Dichalcogenide
III-V semiconductors

ABSTRACT

Among many different applications, optical fibers have not been widely utilized in fundamental optical studies of semiconductors. Their integration into different scientific domains typically leads to the miniaturization and simplification of measurement systems. Here, the optical fiber is integrated into a modulation spectroscopy setup, allowing for the optical characterization of semiconductor materials including van der Waals crystals. Investigating fibers with different core diameters in photoreflectance experiments revealed distinct advantages: fibers with smaller cores are suitable for scanning samples with micrometer spatial resolution, while larger cores facilitate maintaining a greater distance from the sample. In contactless electroreflectance measurements, using fibers enhances the signal and allows for precise electrode positioning, significantly reducing the risk of electrical breakdown. Most importantly, integrating fiber allowed for decoupling the measurement zone from the experimental setup. This pioneering approach not only refines optical spectroscopy methodologies but also optimizes experimental conditions while prioritizing safety and integrity.

1. Introduction

1.1. Modulation spectroscopy for optical characterization of 2D materials

In recent years, there has been a growing interest in the development and study of new 2D materials [1–3]. The field of van der Waals materials is continually evolving as unique mechanical [4,5], optical [6,7], and electronic [8,9] properties are explored, making them promising for next-generation devices [10–12]. With an increasing number of new materials being synthesized [13], the need for advancing and refining characterization methods becomes paramount. Optical spectroscopy plays a crucial role in this context as it offers insights into the electronic band structure, phonon modes, and optical response of these materials [14–17]. Most importantly, the use of modulation techniques in spectroscopy enables the precise extraction of information on the properties of the studied crystal by modulating an internal parameter while measuring a change in the optical response [18,19]. The small perturbation induced in the studied material can be related to the built-in electric field [20,21], strain [22], or temperature [23], which, as a result, leads to a measurable variation in the reflectance of the crystal. Two related modulation spectroscopy techniques, photoreflectance and electroreflectance, which rely on a built-in electric field perturbation, are commonly employed to study the optical properties of semiconductors and other materials [17]. Photoreflectance (PR) involves illuminating a sample with modulated laser light, where the built-in electric field is affected by a photogenerated electron-hole pair, and measuring the changes in the reflected light as a function of the energy [6,9]. On the other hand, electroreflectance, or contactless electroreflectance (CER), relies on directly applying an external electric field to the sample and also measuring the changes in reflected light as a function of the energy [17]. Both techniques (PR and CER) are based on the perturbation of the internal parameter, the built-in electric field, in turn causing changes in the complex dielectric function which leads to a variation in the reflection coefficient at energies corresponding to optical transitions [24]. Analyzing the modulated signal obtained by the PR or CER technique allows for extracting information about the bandgap energy of the studied material, built-in electric field, carrier concentration, and other properties [21,25,26,27]. Both PR and CER serve as powerful tools for studying semiconductors and other material properties. They are non-destructive, non-invasive techniques that facilitate in-situ sample studies, making them well-suited for device fabrication and testing. Moreover, they are complementary techniques that provide valuable insights into the optical properties of materials [28].

* Corresponding author.
E-mail addresses: karolina.ciesiolkiewicz@pwr.edu.pl (K. Ciesiołkiewicz), robert.kudrawiec@pwr.edu.pl (R. Kudrawiec).

https://doi.org/10.1016/j.measurement.2025.117678
Received 13 February 2024; Received in revised form 9 April 2025; Accepted 22 April 2025
Available online 23 April 2025

1.2. Applications of Optical Fibers in Sensing and Spectroscopy

Studies related to fiber optics cover a wide range of fields and applications [29,30]. One of the primary research areas within the optical fibers field is the development of technologies for transmitting data in the form of light [31]. They are also extensively employed in various sensor applications, including temperature sensing, monitoring changes in the refractive index of liquids [32] and gases [33], as well as pressure [34] and humidity measurements [35]. Additionally, fibers play a crucial role in light-emitting sources such as lasers [36]. Research in this domain is focused on enhancing the efficiency, stability, and availability of the mentioned light sources. Furthermore, when fibers are integrated with specific functional materials possessing unique physical, mechanical, and biological properties, they provide an attractive platform for creating 'lab-on-fiber' (LOF) micro-laboratories [37–39].

1.3. Integrating optical fibers with modulation spectroscopy

Over recent decades, numerous methods for structuring fiber optics terminations have been developed, thereby expanding their applications to encompass both measurement and semiconductor devices, which are based on optical fibers and van der Waals crystals [40,41]. In the materials characterization field, optical fibers are mainly used to guide light through a system. They are responsible for illuminating the sample or transmitting a signal from a sample [42]. So far, a limited number of studies have shown the use of optical fibers in experimental setups for modulation spectroscopy measurements [20,43,44]. Optical systems used for both PR and CER techniques, enriched with fibers, could allow for microscopic measurements compatible not only with bulk materials but also exfoliated micro-flakes. The advantage of having a fiber-based probe is freedom of movement and decoupling of the measurement zone from the experimental setup, hence making it less prone to vibrations. For modulation spectroscopy measurements used in fundamental studies of semiconductors, the optical fiber may be used to deliver a light beam to the surface of a crystal being deposited on different substrates, or alternatively, the crystals may be placed directly on the optical fiber.

This work demonstrates, for the first time, the use of optical fibers in both PR and CER spectroscopy techniques. As mentioned before, this approach allowed us to decouple the signal detection area from the experimental setup and perform measurements on representative semiconductor materials including van der Waals crystals. In all experiments, the studied samples were kept on a separate holder, which allowed for precise control of the distance between the sample and the fiber. The presented PR and CER results were obtained using fibers with different core diameters (50 μm, 105 μm, and 400 μm). Moreover, in order to perform CER measurements, a custom holder has been developed. In that holder, the sample was placed on a metal base that served as one of the capacitor plates, while the other plate was located directly on the optical fiber. Additionally, CER sensitivity enhancement has been achieved by inserting a sapphire plate between the optical fiber with the electrode and the sample, enabling the reduction of the sample-fiber distance without the risk of dielectric breakdown. In the next step, the different measurement configurations will be explored, and the studied materials will be placed directly on the core of the flat fiber tip. Locating samples directly at the fiber tip can provide additional advantages in various measurements, such as eliminating the need for system alignment or reducing substrate vibrations. Therefore, further developments in this area are expected.

2. Experimental methods

In the built measurement setup, the probe light is emitted by a quartz tungsten halogen (QTH) lamp known for its good temporal stability [45,46]. This probe beam is subsequently coupled, through a 10x objective lens, to the optical fiber along which it travels until the studied material reflects it, as depicted in the scheme in Fig. 1b. The reflected light is then directed to a spectrometer consisting of a monochromator (Horiba Jobin YvonTriax 550) dispersing the light beam and a photodetector (InGaAs amplified photodiode module). Moreover, to simultaneously evoke changes in the reflectance spectra, the sample can be either (i) illuminated by a laser, which acts as a pump beam and excites electron-hole pairs, leading to a variation of the built-in electric field or (ii) subjected to the external alternating electric field by placing it inside a capacitor which also causes modulation of the built-in electric field.

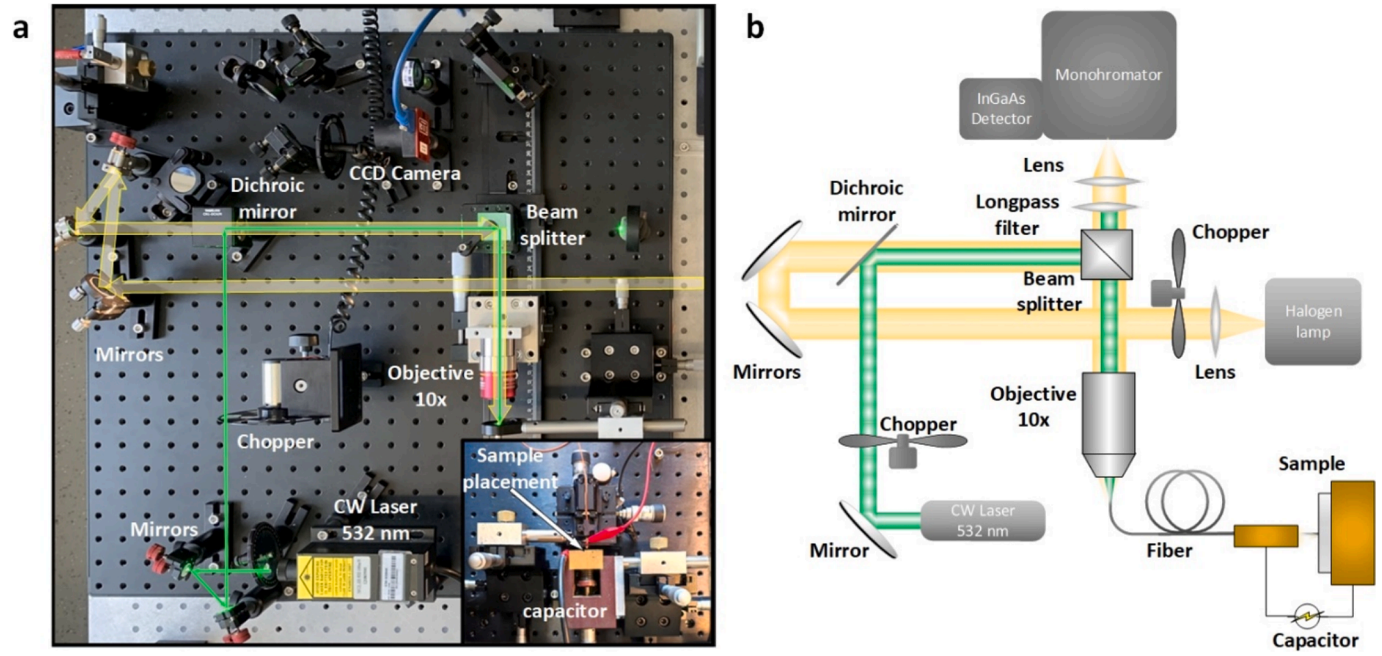

Fig. 1. Experimental setup for PR and CER measurements with an integrated optical fiber. (a) Picture of the measurement setup (in the inset photo, the location of the sample is shown to which probe and pump beam are provided through optical fiber – this part of the setup is located on the separate optical breadboards), and (b) schematic representation of the measurement system.

These two approaches represent PR and CER techniques, respectively. In the case of PR measurements, the pump laser beam is redirected to the main optical axis with a dichroic mirror and coupled to the optical fiber through the same 10x objective lens. Furthermore, in both PR and CER measurements, we used multimode fibers with different core diameters (50 μm, 105 μm, and 400 μm) to thoroughly test the amplitude of the generated signal. The numerical aperture of the 10x objective lens and fibers is compatible, amounting to 0.22. This compatibility ensures optimal light coupling between these two elements. In Fig. 1a, a picture of the experimental setup is also shown.

In the PR configuration, a continuous-wave laser emitting at 532 nm was employed. The pump beam intensity was controlled using a neutral density (grey) filter, and an edge filter was used to prevent the laser beam from entering the monochromator and illuminating the photodetector. To achieve pump beam modulation and thereby modulate the electric field within the studied sample, a mechanical chopper was utilized, modulating the laser beam with a frequency of 280 Hz.

Considering CER measurements, the only change made was in the way modulation of the built-in electric field was evoked. For that purpose, a homemade capacitor was used, allowing for direct perturbation of the electric field inside a sample. The studied sample was mounted on a solid metal substrate, which acted as one of the capacitor plates. In the so-called standard configuration [17], the second plate was a metal mesh positioned in front of the sample (Fig. 2a), where an alternating voltage of ~ 2 kV was applied between the capacitor plates at the frequency of ~ 280 Hz.

In both types of measurements, i.e., PR and CER, we used a lock-in amplifier, which allows for a phase-sensitive detection of very small changes in the analyzed signal (the change in the reflectance on the sixth or seventh decimal can be detected). The lock-in amplifier operates by extracting the AC signal at a specific frequency and phase, which is chosen arbitrarily. In our studies, it is the frequency with which the built-in electric field is modulated. Importantly, for the primary studies involving optical fiber, the metal ferrule was placed directly on the measuring fiber, serving as a second electrode of the capacitor, thereby enabling modulation of the built-in electric field (Fig. 2b). Both electrodes, i.e., the ferrule and solid substrate with the sample on it, were placed on the x-y-z stages to control distance between them precisely. The use of a ferrule as a second electrode, located directly on the optical fibers, offers an advantage over standard solutions (metal mesh) by avoiding the 'shadow effect' [47] and modulating/probing only a small area of the studied sample.

Furthermore, it is important to note that the primary limitation for CER measurements is the maximum voltage that can be applied without causing an electric breakdown in the air gap. This breakdown occurs when the electric field strength exceeds the dielectric strength of air, which stands at approximately 3 kV/mm under standard atmospheric conditions [48]. Voltages exceeding this threshold result in an electrical breakdown, which could be detrimental for both the studied sample and the tip of measuring fiber. To circumvent this issue and enhance the capability of the setup, a different dielectric environment was introduced into the capacitor (Fig. 2c). Notably, sapphire is recognized for its exceptional electrical insulating properties and high dielectric strength, typically 48 kV/mm [49]. This high dielectric strength enables sapphire to withstand remarkably high electric field strengths before reaching the point of electrical breakdown, thereby limiting the possibility of damaging the sample and optical fiber.

3. Results and discussion

3.1. Variation of an optical fiber distance from a sample in PR measurements

To thoroughly assess the impact of integrating optical fibers into our PR experimental setup, we conducted a series of measurements. These involved not only placing the fiber in direct contact with the sample but also systematically increasing the distance between the sample and the fiber tip (schematics in Fig. 3d), continuing until we observed a significant decrease in the resonance amplitude. Additionally, the effect of the core diameter on the PR signal was explored using fibers with various core diameters (50 μm, 105 μm, and 400 μm). PR spectra collected on a bulk $ReSe_2$ crystal sample and are presented in Fig. 3. The obtained resonance corresponds to the A exciton transition in this material and is associated with the J1 point in the Brillouin zone [50].

In conducting our measurements, each experiment with a fiber of different core diameters was started from an initial distance of 0 μm, corresponding to the fiber ferrule touching the sample surface. The air gaps between the fiber and the sample were increased by a micrometer screw. As shown in Fig. 3a, several initial spectra reveal oscillations in the air gap (Fabry-Perot oscillations) created by light reflections between the optical fiber tip and the sample surface. These oscillations are directly related to the width of the air gap, with their period increasing as the gap widens. Notably, for fiber cores with diameters of 50 μm and 105 μm, the initial amplitude of the optical transition exhibited a swift reduction (as shown by the green and blue points in Fig. 3d). In contrast, for the fiber with a 400 μm core diameter, the amplitude of the PR signal remained consistent up to a distance of 500 μm, as indicated by the magenta points in Fig. 3d. As the distance was further increased, a simultaneous decrease was observed in both the amplitude of the PR signal and the intensity of the reflected white light. This reduction in

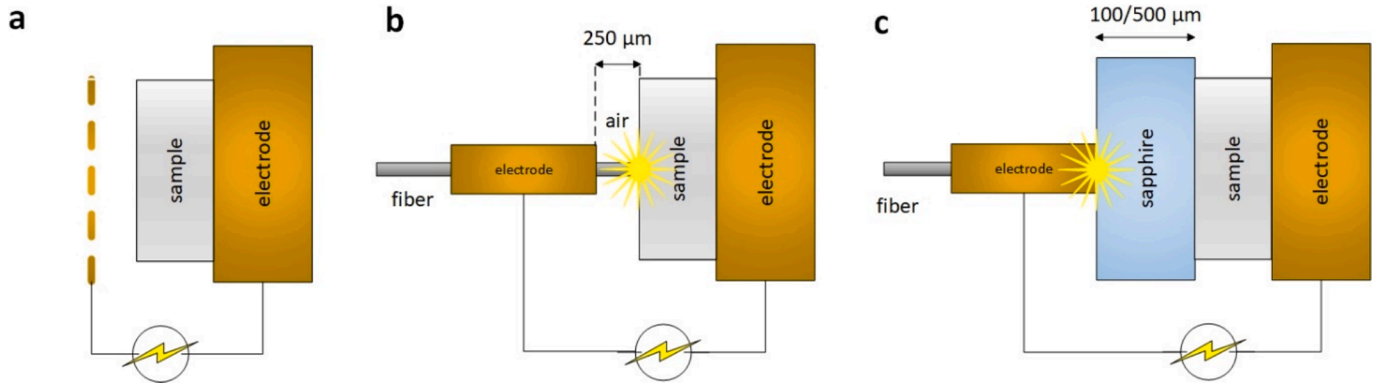

Fig. 2. Different configurations of a homemade capacitor for CER measurements: (a) the conventional configuration where the top electrode consists of a finely structured metal mesh, (b) a capacitor featuring one electrode (ferrule) directly placed in a close proximity to a fiber that passes through it, allowing for separate positioning of each (the direct contact between the electrode and the fiber is crucial for optimizing the sensitivity and accuracy of the measurements), and (c) the third configuration with a sapphire plate added between the capacitor electrodes. By incorporating the sapphire plate, we aimed to capitalize on its superior insulating characteristics to enhance the modulation and control of the electric field within the capacitor.

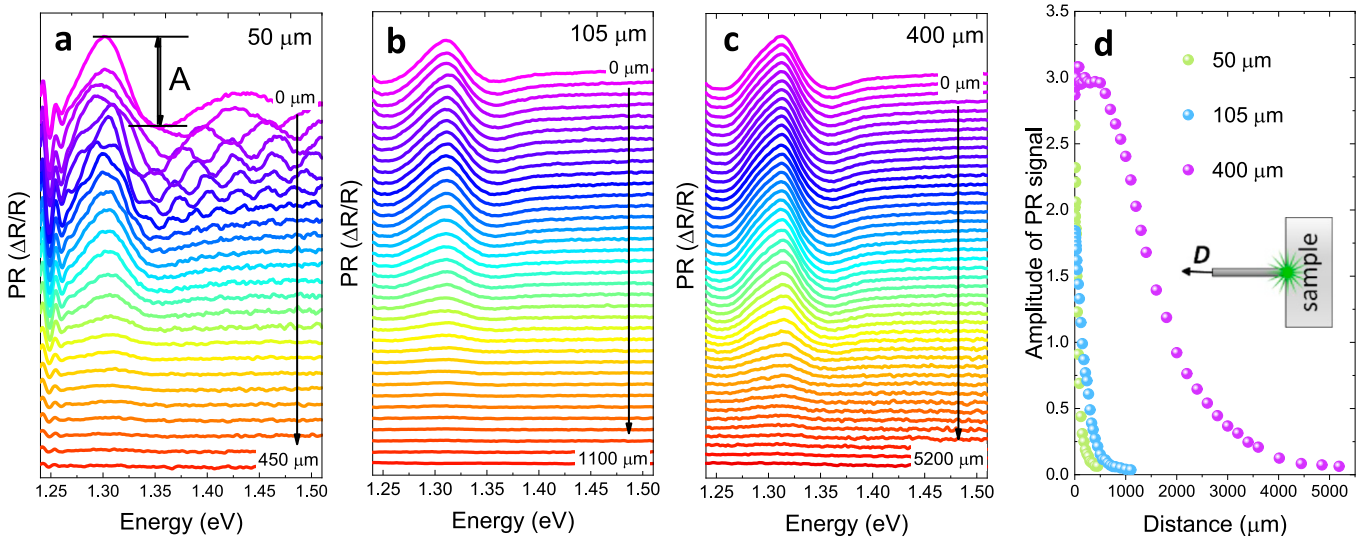

Fig. 3. Photoreflectance spectra of the $ReSe_2$ sample obtained with increasing distances between the sample and fibers of different core diameters (a) 50 μm, (b) 105 μm, and (c) 400 μm. (d) Relationship between the amplitude of the PR signal and distance for each experimental configuration. It can be seen that the signal is still detectable for fiber being moved away from the sample by up to 5200 μm.

amplitude is attributed to weaker modulation, as increasing the distance between the fiber tip and the sample leads to a decrease in the power density of the laser (pump beam). The maximum distance at which optical resonance was still measurable differed across fiber cores. For the 50 μm core, this distance was determined to be 450 μm, and the 105 μm core exhibited resonance up to a distance of 1100 μm. For the 400 μm core diameter, resonance persisted over a much larger distance, reaching 5200 μm. A summary of these measurements is presented in Fig. 3d. It can be clearly seen that in the experiment with the fiber of 400 μm core diameter, the signal amplitude corresponding to the optical transition is the largest. This large amplitude of the PR signal simultaneously results in a better signal-to-noise ratio, which remains constant up to a distance of approximately 600 μm between the fiber tip and the sample surface. This is important in the context of measuring signals from transitions characterized by weak oscillatory strength and from samples with non-uniform surfaces that may affect the contact between the sample and the fiber.

Providing light by optical fibers allowed us to separate the sample from the experimental setup, so we were able to place the studied material independently from the rest of the measuring equipment and demonstrate a configuration enabling remote detection. A comparison of optical fibers with different core diameters revealed that fibers with smaller core diameters could facilitate raster scanning of samples, allowing for the determination of a map of optical properties. On the other hand, fibers with larger core diameters are advantageous for maintaining a greater distance between the fiber tip and the studied material. The choice between these approaches depends on specific experimental requirements.

3.2. *CER measurements with different configurations of a capacitor*

Another objective of these studies was to utilize fiber optics in CER, aiming to achieve stronger resonance signal in comparison to the amplitude of noise, which corresponds to optical transitions. For that purpose, we have collected CER spectra for the three different samples ($ReSe_2$, $MoTe_2$, and InP) using various designs of capacitors, enabling a direct comparison and evaluation of the benefits offered by fiber optics integration. As previously mentioned, the main part of the typical setup for CER measurements is a capacitor, which in the conventional configuration [17] consists of two electrodes: one made of solid metal, serving as the platform for the sample placement, and the other consisting of a metal mesh that exhibits quasi-transparency to white probe light (Fig. 4d). In our experimental investigation, this standard capacitor were compared with the other design based on the fiber optics where the second electrode was a metal ferrule Fig. 4e. The CER spectra obtained with these two different capacitor designs are presented in Fig. 4 and were collected for representative samples from two distinct material systems: transition metal dichalcogenides (TMDCs) and III-V semiconductors. For representative TMDC $ReSe_2$ crystals (Fig. 4a) the obtained optical transition is located at ~ 1.34 eV, which is consistent with the results of our PR measurements as well as previous studies [50]. Regarding CER spectra of $MoTe_2$ and InP, Fig. 4b and c, the positions of observed resonances are in near-infrared at 1.06 eV and 1.35 eV, respectively, which is in good agreement with literature [51,52]. As evident in Fig. 4, the amplitude of resonance for each sample is much stronger than for the standard capacitor (b lue line) when a fiber of a bigger core was used (400 μm – green line). The significant increase in the amplitude of optical transitions in the experiment with 400 μm fiber is related to the stronger modulation of the built-in electric field as well as more light being reflected from the surface of the sample. Additionally, our uniquely designed capacitor depicted in Fig. 4e, with one of its electrodes placed on a fiber, exhibits a distinctive advantage by effectively circumventing the occurrence of the 'shadow', which can impact the measurements and, as already mentioned, the amplitude of the CER signal. Moreover, it is important to note that all spectra were measured with the same voltage applied to the plates of the capacitor, which was 2000 V. Based on the conducted experiments, it can be seen (blue vs. green spectra in Fig. 4a, 4b, and 4c) that the CER setup equipped with an optical fiber provides a stronger amplitude for optical transitions than the traditional non-fiber-based setup.

The fiber optic-based solution gives significantly better results, although it is necessary to remember certain limitations of such a system. The limitations of this approach include the fact that light diverges after exiting the optical fiber. As a result, when the fiber is moved further from the sample, the beam becomes less focused, leading to reduced light intensity on the sample surface. Additionally, the reflected signal may not fully couple back into the fiber, affecting the measurement efficiency. Moreover, the fiber must be precisely aligned perpendicular to the sample surface to ensure optimal signal collection. For the mentioned purposes, it is important to pay careful attention to the positioning of the optical fiber relative to the sample surface.

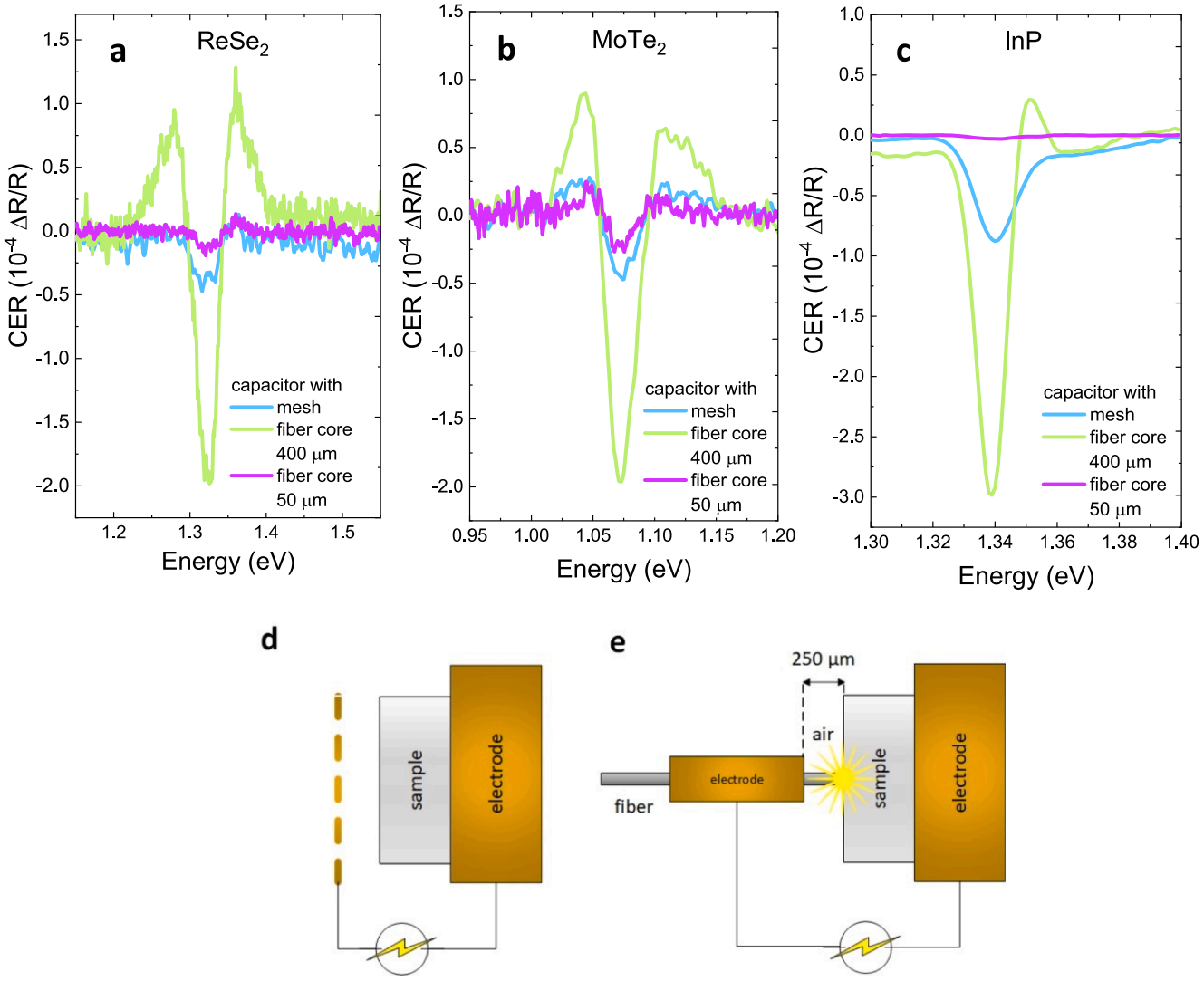

Fig. 4. Two different configurations of the capacitor were employed to measure (a) $ReSe_2$, (b) $MoTe_2$, and (c) InP. These configurations consisted of a standard capacitor with a metal mesh as a top electrode (d) and a capacitor with one electrode directly placed on a fiber (e). The measurements conducted using the fiber with a 400 μm core diameter exhibited a significantly stronger signal compared to the mesh-type capacitor.

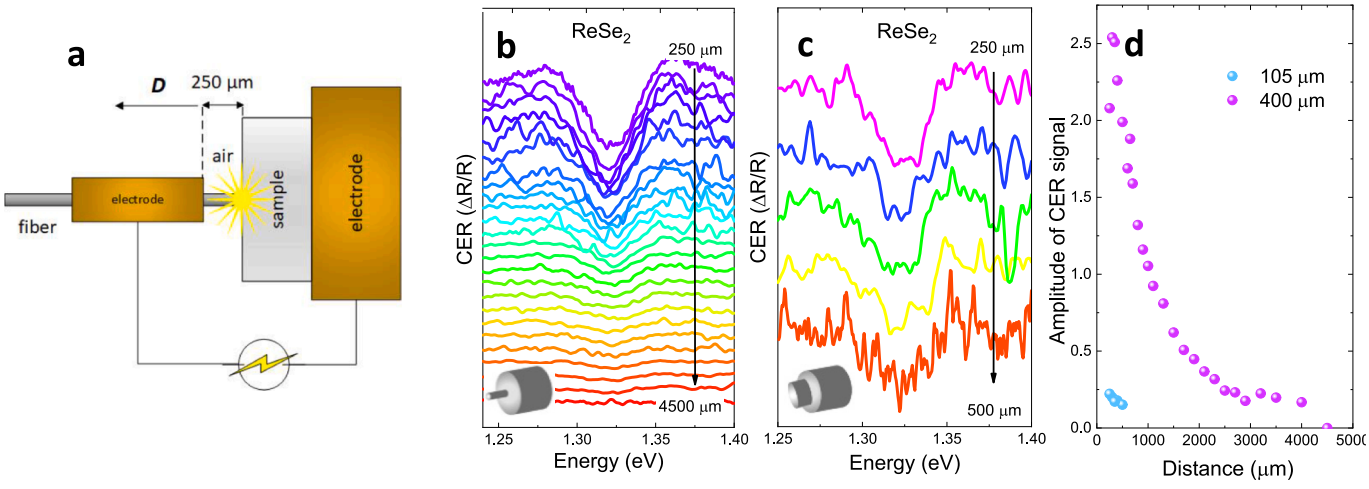

Fig. 5. (a) The scheme of capacitor for CER measurements (D-distance). Contactless electroreflectance spectra of the $ReSe_2$ sample obtained with fibers of core diameter 105 μm (b) and 400 μm (c) for the increasing distance between the electrodes of a capacitor. (d) Amplitude of CER signal versus distance: it can be observed that at a voltage of 2 kV, the signal disappears around the separation of 4500 μm.

3.3. Variation of the distance between electrodes of a capacitor in CER measurements

To further evaluate the usefulness of our new fiber-optics-based capacitor design, we conducted additional experiments. In this case, for a selected material, namely $ReSe_2$, CER spectra were collected in a configuration where the distance between the electrodes of the capacitor was systematically increased while the applied voltage was kept constant. At the same time, the fiber remained fixed in its original position, i.e., in contact with the surface of the sample. Initially, the distance between electrodes was set at 250 μm to avoid a breakdown in the air (Fig. 5a). Subsequently, the mentioned gap was extended to 500 μm for a fiber with a core dimension of 105 μm (Fig. 5b) above that distance, the amplitude of the optical transition for $ReSe_2$ significantly diminished, becoming indistinguishable from the noise. Regarding the same experiment but for a fiber with a core dimension of 400 μm, the distance between plates of the capacitor was increased up to 4500 μm (Fig. 5c), after which the CER resonance weakened beyond measurable levels. The dependence of the amplitude of the resonance on distance for both experiments is shown in Fig. 5d. This variation in the electrode spacing had a direct impact on the decrease in amplitude of the measured optical transition, which was attributed to the reduction of the electric field strength between the capacitor plates as they moved further apart. This conclusion is confirmed since the amount of reflected light to the fiber remained constant throughout the experiment as the fiber tip was placed in contact with the sample and remained unchanged. Therefore, the electric field drop, which leads to weaker internal parameter modulation (built-in electric field), is the primary factor impacting the resonance amplitude. Moreover, by increasing the distance between the electrodes and consequently reducing the electric field strength, we minimized the risk of electrical breakdown, thereby enhancing the safety and protecting both the sample and the fiber tip.

3.4. Comparison of a capacitor with air gap and sapphire plate in CER measurements

In the latest capacitor configuration, Fig. 2c, a significant change was made in the dielectric environment between capacitor plates, transitioning from an air gap to a sapphire. That approach allowed us to increase the amplitude of measured CER resonance further and holds the potential to facilitate CER measurements at low temperatures. The idea of change in the dielectric environment is related to the distinct

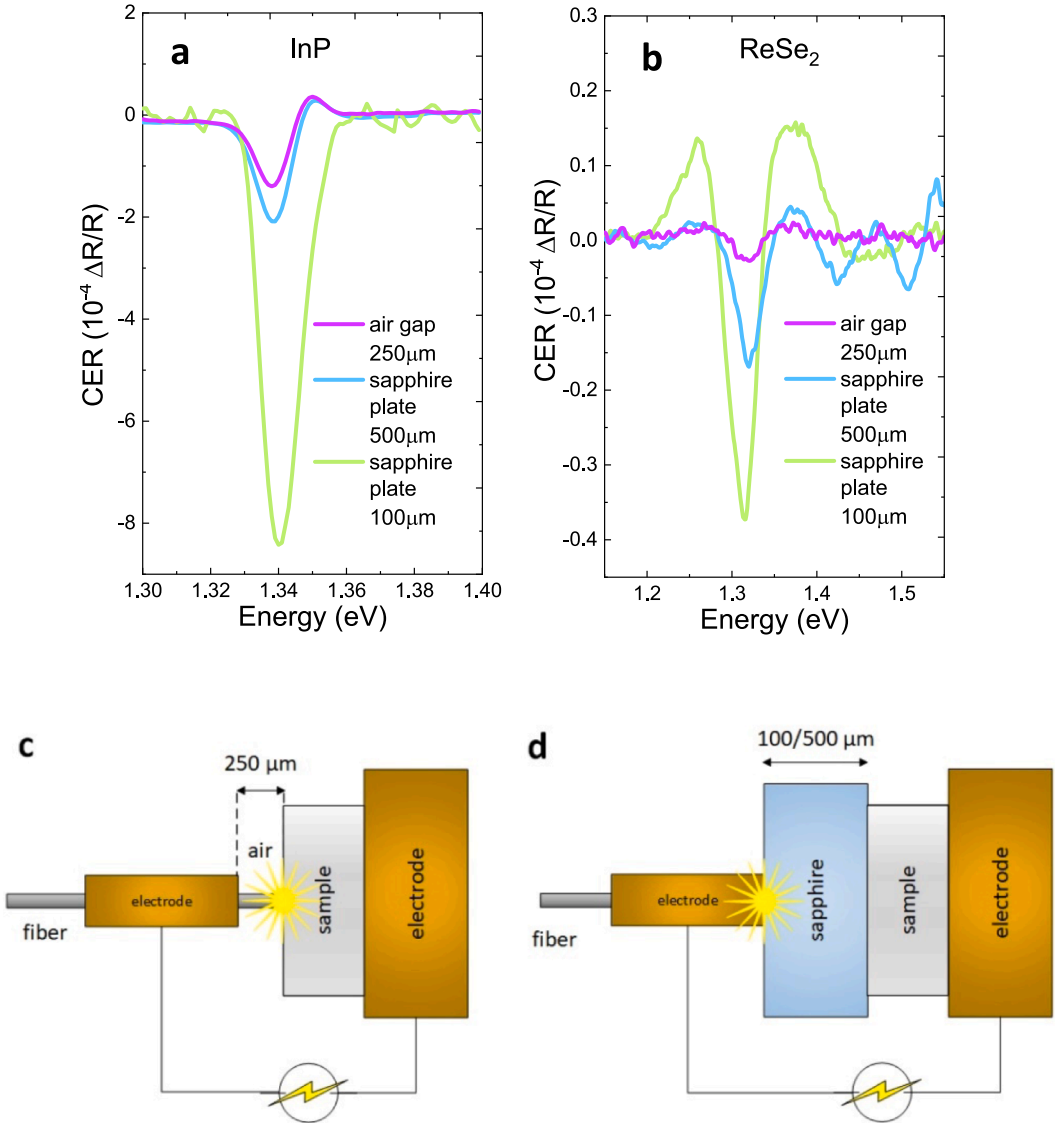

Fig. 6. CER spectra of (a) InP and (b) $ReSe_2$ samples were measured using a capacitor setup with a 250 μm air gap between the electrodes (c) or with a sapphire plate (100/500 μm) placed between the electrodes (d). The inclusion of the 100 μm thick sapphire resulted in notable changes in the spectra for both samples.

electrical breakdown points exhibited by different materials and described by dielectric strength. Air, for instance, experiences breakdown when the electric field is greater than approximately 3 kV/mm under standard atmospheric conditions [48]. However, sapphire, known for its remarkable electrical insulating properties, has a notably higher dielectric strength, typically reaching 48 kV/mm [48]. Within this context, the alteration in dielectric material from air to sapphire is a crucial change in the setup. Throughout this series of experiments, the distance from the sample to the fiber tip remained fixed at 250 μm as well as the voltage applied to capacitor plates. In contrast, when the sapphire plates were employed, that distance was fixed by the thicknesses of the plates, which were 500 μm and 100 μm. The introduction of sapphire, with its increased dielectric strength, evidently influences the amplitude of the observed resonance for InP and $ReSe_2$ crystals. This influence is primarily due to the substantial impact of the dielectric environment on the modulation of the built-in electric field within the studied material [47].

The measured CER spectra, as depicted in Fig. 6a and b, represent the effects of the above-mentioned changes. The purple line corresponds to the configuration with an air gap, while the blue line represents the setup with an integrated 500 μm-thick sapphire plate. Notably, despite the increased distance between the electrodes of the capacitor when employing the sapphire with a larger thickness, a stronger amplitude of resonance is observed for both samples. This behavior is related to a stronger modulation of the built-in electric field in the investigated sample after inserting the sapphire plate. Furthermore, the observed difference in resonance amplitudes can be elucidated by considering the characteristics of sapphire, such as higher relative permittivity affecting the capacitance of the used capacitor [53]. When employing sapphire with a thickness of 100 μm, a gap between the electrodes is reduced, consequently leading to higher perturbation of the built-in electric field. As a result of this increased perturbation, a visibly stronger resonance is observed in the spectra. At the same time, the use of sapphire protects the sample and fiber from damage. This is related to its inherent properties, including exceptional dielectric strength, which shields both the sample and the fiber from potential damage due to electric breakdown. The protective role of sapphire is paramount in ensuring the integrity and longevity of the components involved in the experimental setup. While sapphire offers distinct advantages in terms of high dielectric strength and relative permittivity, other dielectric materials could also be considered for similar setups. For instance, quartz (SiO_2), with a dielectric strength of approximately 20–40 kV/mm and a relative permittivity of around 3.8[54], provides reasonable electrical insulation, but it would result in a weaker modulation of the electric field compared to sapphire due to its lower permittivity. Additionally, magnesium oxide (MgO), with a dielectric strength of 10–35 kV/mm[55], offers good stability and insulation properties. However, its lower dielectric constant and increased hygroscopic nature could pose challenges in maintaining a stable setup. Another potential candidate is hafnium oxide (HfO_2), which boasts a high dielectric constant (~25) [56] but is often more difficult to procure and may not be as thermally stable as sapphire in certain conditions. Boron nitride (BN), known for its high thermal stability, could be used as a dielectric but has a relatively lower dielectric strength (40 kV/mm)[57]. In contrast, sapphire stands out not only due to its superior dielectric strength and high relative permittivity but also for its excellent mechanical properties, such as high thermal stability and resistance to electrical breakdown, making it the optimal choice for this experimental setup. Therefore, while the alteration to sapphire not only influences the observed resonance amplitude, its role as a protective barrier against damage to sensitive components like the sample and the fiber cannot be understated. In this dual capacity of influencing resonance characteristics and providing protection, the selection of sapphire emerges as a critical and beneficial choice within this experimental framework. Overall, all the obtained experimental results are highly reproducible, provided that the studied materials remain stable under ambient conditions.

4. Summary

The results of the studies presented here can advance the methodology of optical spectroscopy for the characterization of semiconductor materials including van der Waals crystals. Incorporating optical fibers into both PR and CER setups allows for decoupling the measurement area, where the sample is located, from the rest of the experimental equipment. In the PR experiments, optical fibers of various core diameters (50 μm, 105 μm, and 400 μm) were used to examine the signal amplitude at different distances of a fiber tip from the sample surface. These measurements demonstrate that smaller core diameter fibers could allow for scanning the optical properties of a sample across it. In comparison, optical fibers with larger core diameters enable maintaining larger distances between the fiber tip and the material. These comprehensive studies together with a diversity of optical fibers, offer valuable insights into selecting the ideal approach based on specific experimental needs.

Moreover, in CER measurements, the comparison between the conventional mesh-type electrode capacitors and fiber-integrated capacitors showed significantly stronger signals when fibers with larger core diameters were used. Additionally, such a capacitor with one electrode (metal ferrule) directly placed on a fiber presents distinct advantages by overcoming the 'shadow effect' and effectively probing only a small area of the studied sample. Variations in the distance between capacitor electrodes in CER experiments showed a direct impact on signal amplitude, emphasizing the importance of precise control over the electrode spacing. Notably, increasing the electrode distance can enhance safety measures against electrical breakdown, thus safeguarding both the sample and measuring fiber. Moreover, the transition from an air gap to sapphire as a dielectric material for the capacitor in CER measurements demonstrated notable improvements in the amplitude of optical transition and protective measures. This is related to the high dielectric strength of sapphire, which acts as a shield, safeguarding the sample and fiber from potential damage due to electric breakdown, a critical issue in fiber-based experimental setups.

Overall, this work introduces a novel approach by integrating optical fibers into PR and CER measurement setups, enabling independent sample positioning/locating and offering comprehensive insights into optimizing experimental conditions. Our findings pave the way for enhanced methodologies in optical spectroscopy, benefiting the characterization and understanding of diverse materials, including van der Waals crystals and group III-V semiconductors while ensuring the safety and integrity of sensitive components within the experimental setup.

CRediT authorship contribution statement

K. Ciesiołkiewicz: Writing – original draft, Visualization, Methodology, Investigation, Conceptualization. **J. Kopaczek:** Writing – review & editing, Visualization, Methodology, Investigation, Conceptualization. **S.J. Zelewski:** Writing – review & editing, Methodology. **R. Kudrawiec:** Writing – review & editing, Visualization, Supervision, Resources, Project administration, Funding acquisition, Conceptualization.

Declaration of competing interest

The authors declare that they have no known competing financial interests or personal relationships that could have appeared to influence the work reported in this paper.

Acknowledgments

This work was supported by project No. 2022/45/B/ST7/02750 (OPUS23) from the National Science Centre.

Data availability

Data will be made available on request.

References

[1] R. Mas-Ballesté, C. Gómez-Navarro, J. Gómez-Herrero, F. Zamora, 2D materials: to graphene and beyond, Nanoscale 3 (2011) 20–30, https://doi.org/10.1039/C0NR00323A.

[2] S.Z. Butler, S.M. Hollen, L. Cao, Y. Cui, J.A. Gupta, H.R. Gutiérrez, T.F. Heinz, S. S. Hong, J. Huang, A.F. Ismach, E. Johnston-Halperin, M. Kuno, V.V. Plashnitsa, R. D. Robinson, R.S. Ruoff, S. Salahuddin, J. Shan, L. Shi, M.G. Spencer, M. Terrones, W. Windl, J.E. Goldberger, Progress, challenges, and opportunities in two-dimensional materials beyond graphene, ACS Nano 7 (2013) 2898–2926, https://doi.org/10.1021/nn400280c.

[3] K.S. Novoselov, A. Mishchenko, A. Carvalho, A.H. Castro Neto, 2D materials and van der Waals heterostructures, Science 353 (2016) aac9439, https://doi.org/10.1126/science.aac9439.

[4] J.H. Kim, J.H. Jeong, N. Kim, R. Joshi, G.-H. Lee, Mechanical properties of two-dimensional materials and their applications, J. Phys. d: Appl. Phys. 52 (2019) 083001, https://doi.org/10.1088/1361-6463/aaf465.

[5] D. Jiang, Z. Liu, Z. Xiao, Z. Qian, Y. Sun, Z. Zeng, R. Wang, Flexible electronics based on 2D transition metal dichalcogenides, J. Mater. Chem. A 10 (2021) 89–121, https://doi.org/10.1039/D1TA06741A.

[6] G. Wang, A. Chernikov, M.M. Glazov, T.F. Heinz, X. Marie, T. Amand, B. Urbaszek, Colloquium: Excitons in atomically thin transition metal dichalcogenides, Rev. Mod. Phys. 90 (2018) 021001, https://doi.org/10.1103/RevModPhys.90.021001.

[7] P. Kumbhakar, C. Chowde Gowda, C.S. Tiwary, Advance Optical Properties and Emerging Applications of 2D Materials, Frontiers in Materials 8 (2021). https://www.frontiersin.org/articles/10.3389/fmats.2021.721514 (accessed October 26, 2023).

[8] T. Dutta, N. Yadav, Y. Wu, G.J. Cheng, X. Liang, S. Ramakrishna, A. Sbai, R. Gupta, A. Mondal, Z. Hongyu, A. Yadav, Electronic properties of 2D materials and their junctions, Nano Mater. Sci. (2023), https://doi.org/10.1016/j.nanoms.2023.05.003.

[9] R. Roldán, J.A. Silva-Guillén, M.P. López-Sancho, F. Guinea, E. Cappelluti, P. Ordejón, Electronic properties of single-layer and multilayer transition metal dichalcogenides MX_2 (M=Mo,W and X=S, Se), Ann. Phys. 526 (2014) 347–357, https://doi.org/10.1002/andp.201400128.

[10] D. Jariwala, V.K. Sangwan, L.J. Lauhon, T.J. Marks, M.C. Hersam, Emerging device applications for semiconducting two-dimensional transition metal dichalcogenides, ACS Nano 8 (2014) 1102–1120, https://doi.org/10.1021/nn500064s.

[11] G. Wang, Y. Zhang, C. You, B. Liu, Y. Yang, H. Li, A. Cui, D. Liu, H. Yan, Two dimensional materials based photodetectors, Infrared Phys. Technol. 88 (2018) 149–173, https://doi.org/10.1016/j.infrared.2017.11.009.

[12] K. Khan, A.K. Tareen, M. Aslam, R. Wang, Y. Zhang, A. Mahmood, Z. Ouyang, H. Zhang, Z. Guo, Recent developments in emerging two-dimensional materials and their applications, J. Mater. Chem. C 8 (2020) 387–440, https://doi.org/10.1039/C9TC04187G.

[13] R. Bian, C. Li, Q. Liu, G. Cao, Q. Fu, P. Meng, J. Zhou, F. Liu, Z. Liu, Recent progress in the synthesis of novel two-dimensional van der Waals materials, Natl. Sci. Rev. 9 (2022) nwab164, https://doi.org/10.1093/nsr/nwab164.

[14] F.H. Pollak, H. Shen, Modulation spectroscopy of semiconductors: bulk/thin film, microstructures, surfaces/interfaces and devices, Mater. Sci. Eng. R. Rep. 10 (1993) xv–374, https://doi.org/10.1016/0927-796X(93)90004-M.

[15] W. Zhao, Z. Ghorannevis, K.K. Amara, J.R. Pang, M. Toh, X. Zhang, C. Kloc, P. H. Tan, G. Eda, Lattice dynamics in mono- and few-layer sheets of WS2 and WSe2, Nanoscale 5 (2013) 9677–9683, https://doi.org/10.1039/C3NR03052K.

[16] Y. Li, A. Chernikov, X. Zhang, A. Rigosi, H.M. Hill, A.M. Van Der Zande, D. A. Chenet, E.M. Shih, J. Hone, T.F. Heinz, Measurement of the optical dielectric function of monolayer transition-metal dichalcogenides: MoS2, Mo S e2, WS2, and WS e2, Phys. Rev. B - Condensed Matter and Mater. Phys. 90 (2014), https://doi.org/10.1103/PhysRevB.90.205422.

[17] R. Kudrawiec, W. Walukiewicz, Electromodulation spectroscopy of highly mismatched alloys, J. Appl. Phys. 126 (2019) 141102, https://doi.org/10.1063/1.5111965.

[18] D.E. Aspnes, A.A. Studna, Dielectric functions and optical parameters of Si, Ge, GaP, GaAs, GaSb, InP, InAs, and InSb from 1.5 to 6.0 eV, Phys. Rev. B 27 (1983) 985–1009. DOI: 10.1103/PhysRevB.27.985.

[19] R. Kudrawiec, M. Rudziński, J. Serafinczuk, M. Zając, J. Misiewicz, Photoreflectance study of exciton energies and linewidths for homoepitaxial and heteroepitaxial GaN layers, J. Appl. Phys. 105 (2009) 093541, https://doi.org/10.1063/1.3125508.

[20] H. Chouaib, M. Murtagh, P. Kelly, A micro-optical modulation spectroscopy technique for local strain measurement, Rev. Sci. Instrum. 82 (2011) 043901, https://doi.org/10.1063/1.3569764.

[21] J. Kopaczek, F. Dybała, S.J. Zelewski, N. Sokołowski, W. Żuraw, K.M. McNicholas, R.H. El-Jaroudi, R.C. White, S.R. Bank, R. Kudrawiec, Photoreflectance studies of temperature and hydrostatic pressure dependencies of direct optical transitions in BGaAs alloys grown on GaP, J. Phys. d: Appl. Phys. 55 (2021) 015107, https://doi.org/10.1088/1361-6463/ac2643.

[22] C.H. Ho, P.C. Liao, Y.S. Huang, K.K. Tiong, Temperature dependence of energies and broadening parameters of the band-edge excitons of ReS2 and ReSe2, Phys. Rev. B 55 (1997) 15608–15613, https://doi.org/10.1103/PhysRevB.55.15608.

[23] C.H. Ho, S.L. Lin, C.C. Wu, Thermoreflectance study of the electronic structure of Ge(Se_1-xS_x)2, Phys. Rev. B 72 (2005) 125313, https://doi.org/10.1103/PhysRevB.72.125313.

[24] B.O. Seraphin, N. Bottka, Band-structure analysis from electro-reflectance studies, Phys. Rev. 145 (1966) 628–636, https://doi.org/10.1103/PhysRev.145.628.

[25] N.F. Zorn, F. Scuratti, F.J. Berger, A. Perinot, D. Heimfarth, M. Caironi, J. Zaumseil, Probing mobile charge carriers in semiconducting carbon nanotube networks by charge modulation spectroscopy, ACS Nano 14 (2020) 2412–2423, https://doi.org/10.1021/acsnano.9b09761.

[26] R. Kudrawiec, Application of contactless electroreflectance to III-nitrides, Physica Status Solidi (b) 247 (2010) 1616–1621, https://doi.org/10.1002/pssb.200983688.

[27] H. Shen, M. Dutta, Franz–Keldysh oscillations in modulation spectroscopy, J. Appl. Phys. 78 (1995) 2151–2176, https://doi.org/10.1063/1.360131.

[28] X. Yin, F.H. Pollak, Novel contactless mode of electroreflectance, Appl. Phys. Lett. 59 (1991) 2305–2307, https://doi.org/10.1063/1.106051.

[29] B. Lee, Review of the present status of optical fiber sensors, Opt. Fiber Technol. 9 (2003) 57–79, https://doi.org/10.1016/S1068-5200(02)00527-8.

[30] J. Chen, Y. Xiong, F. Xu, Y. Lu, Silica optical fiber integrated with two-dimensional materials: towards opto-electro-mechanical technology, Light Sci. Appl. 10 (2021) 78, https://doi.org/10.1038/s41377-021-00520-x.

[31] Front Matter, in: Fiber-Optic Communication Systems, John Wiley & Sons, Ltd, 2010: pp. i–xvii. DOI: 10.1002/9780470918524.fmatter.

[32] S.D. Personick, Fiber Optics: Technology and Applications, Springer Science & Business Media, 2013.

[33] M. Quan, J. Tian, Y. Yao, Ultra-high sensitivity Fabry–Perot interferometer gas refractive index fiber sensor based on photonic crystal fiber and Vernier effect, Opt. Lett., OL 40 (2015) 4891–4894, https://doi.org/10.1364/OL.40.004891.

[34] H. Bae and M. Yu, Miniature Fabry-Perot pressure sensor created by using UV-molding process with an optical fiber based mold, (n.d.).

[35] J. Wang, L. Wang, X. Su, R. Xiao, H. Cheng, Temperature, stress, refractive index and humidity multi parameter highly integrated optical fiber sensor, Opt. Laser Technol. 152 (2022) 108086, https://doi.org/10.1016/j.optlastec.2022.108086.

[36] A.S. Kurkov, V.M. Paramonov, O.I. Medvedkov, Ytterbium fiber laser emitting at 1160 nm, Laser Phys. Lett. 3 (2006) 503, https://doi.org/10.1002/lapl.200610040.

[37] M. Consales, A. Ricciardi, A. Crescitelli, E. Esposito, A. Cutolo, A. Cusano, Lab-on-fiber technology: toward multifunctional optical nanoprobes, ACS Nano 6 (2012) 3163–3170, https://doi.org/10.1021/nn204953e.

[38] M. Consales, M. Pisco, A. Cusano, Lab-on-fiber technology: a new avenue for optical nanosensors, Photonic Sens 2 (2012) 289–314, https://doi.org/10.1007/s13320-012-0095-y.

[39] P. Vaiano, B. Carotenuto, M. Pisco, A. Ricciardi, G. Quero, M. Consales, A. Crescitelli, E. Esposito, A. Cusano, Lab on fiber technology for biological sensing applications, Laser Photonics Rev. 10 (2016) 922–961, https://doi.org/10.1002/lpor.201600111.

[40] G. Kostovski, P.R. Stoddart, A. Mitchell, The optical fiber tip: an inherently light-coupled microscopic platform for micro- and nanotechnologies, Adv. Mater. 26 (2014) 3798–3820, https://doi.org/10.1002/adma.201304605.

[41] Y. Xiong, F. Xu, Multifunctional integration on optical fiber tips: challenges and opportunities, AP 2 (2020) 064001, https://doi.org/10.1117/1.AP.2.6.064001.

[42] D. Kuciauskas, J.N. Duenow, A. Kanevce, J.V. Li, M.R. Young, P. Dippo, D.H. Levi, Optical-fiber-based, time-resolved photoluminescence spectrometer for thin-film absorber characterization and analysis of TRPL data for CdS/CdTe interface, in: 2012 38th IEEE Photovoltaic Specialists Conference, 2012: pp. 001721–001726. DOI: 10.1109/PVSC.2012.6317927.

[43] H. Chouaib, Modeling the time-dependence of the photoreflectance spectroscopy on ultra-shallow As+ ion implanted silicon, Results Opt. 8 (2022) 100256, https://doi.org/10.1016/j.rio.2022.100256.

[44] H. Chouaib, M.E. Murtagh, V. Guènebaut, S. Ward, P.V. Kelly, M. Kennard, Y.M. Le Vaillant, M.G. Somekh, M.C. Pitter, S.D. Sharples, Rapid photoreflectance spectroscopy for strained silicon metrology, Rev. Sci. Instrum. 79 (2008) 103106, https://doi.org/10.1063/1.2999919.

[45] P. Disterhoft, Stability characteristics of 1000 watt FEL-type QTH lamps during the seasoning and screening process, in: Ultraviolet Ground- and Space-Based Measurements, Models, and Effects V, SPIE, 2005: pp. 124–135. DOI: 10.1117/12.614584.

[46] J. Kopaczek, S.J. Zelewski, R. Kudrawiec, Supercontinuum source as a probing beam in photoreflectance and photoacoustic spectroscopy, Measurement 146 (2019) 879–884, https://doi.org/10.1016/j.measurement.2019.07.021.

[47] A. Ślusarz, J. Kopaczek, F. Dybała, A. Wiatrowska, F. Granek, R. Kudrawiec, Contactless electroreflectance spectroscopy with a semitransparent capacitor made of a silver mesh of ultrathin lines, (n.d.).

[48] J.J. Lowke, Theory of electrical breakdown in air-the role of metastable oxygen molecules, J. Phys. D: Appl. Phys. 25 (1992) 202, https://doi.org/10.1088/0022-3727/25/2/012.

[49] E.R. Dobrovinskaya, L.A. Lytvynov, V. Pishchik, Properties of Sapphire, in: V. Pishchik, L.A. Lytvynov, E.R. Dobrovinskaya (Eds.), Sapphire: Material, Manufacturing, Applications, Springer US, Boston, MA, 2009: pp. 55–176. DOI: 10.1007/978-0-387-85695-7_2.

[50] R. Oliva, M. Laurien, F. Dybala, J. Kopaczek, Y. Qin, S. Tongay, O. Rubel, R. Kudrawiec, Pressure dependence of direct optical transitions in ReS2 and ReSe2, Npj 2D Mater Appl 3 (2019) 1–8. DOI: 10.1038/s41699-019-0102-x.

[51] Z. Hang, H. Shen, F.H. Pollak, Temperature dependence of the Eo and Eo + △o gaps of InP up to 600°C, Solid State Commun. 73 (1990) 15–18, https://doi.org/10.1016/0038-1098(90)90005-V.

[52] S.J. Zelewski, R. Kudrawiec, Photoacoustic and modulated reflectance studies of indirect and direct band gap in van der Waals crystals, Sci. Rep. 7 (2017), https://doi.org/10.1038/s41598-017-15763-1.
[53] A.M. Melnychenko, S.J. Zelewski, D. Hlushchenko, K. Lis, A. Bachmatiuk, R. Kudrawiec, Electro-modulation and surface photovoltage spectroscopy with semi-transparent graphene electrodes, Appl. Surf. Sci. 613 (2023) 156020, https://doi.org/10.1016/j.apsusc.2022.156020.
[54] Crystal quartz (SiO2) and Fused Silica, (n.d.). https://www.mt-berlin.com/frames_cryst/descriptions/quartz%20.htm (accessed April 7, 2025).
[55] MAGNESIUM OXIDE (MgO), (n.d.). https://qedfusion.org/LIB/PROPS/PANOS/mgo.html (accessed April 7, 2025).
[56] R. Southwick, An Investigation of Carrier Transport in Hafnium Oxide/Silicon Dioxide MOS Gate Dielectric Stacks from 5.6-400K, Boise State University Theses and Dissertations (2010). https://scholarworks.boisestate.edu/td/149.
[57] Boron Nitride - BN, Precision Ceramics (n.d.). https://precision-ceramics.com/materials/boron-nitride/ (accessed April 7, 2025).

2.2. Thermotransmittance spectroscopy of layered crystals using lab on fiber

Citation:

Published in *Nanoscale*, 2025,17, 16818-16828

DOI: 10.1039/D5NR00301F

Co-authors:

Karolina Ciesiołkiewicz-Klepek, Jan Kopaczek, Robert Kudrawiec

Author's contribution:

Karolina Ciesiołkiewicz-Klepek designed the optical setup and built the complete measurement system, conducted all transmission and photomodulated transmission measurements, collected and analyzed the data, prepared the figures and graphical representations of the results, developed the interpretation of the results, wrote the manuscript, and served as the corresponding author.

Context within the dissertation:

This article presents the introduction and validation of a novel thermotransmittance spectroscopy method for layered crystals based on a lab-on-fiber approach. It extends the fiber-based optical techniques developed earlier by incorporating thermal effects into transmission measurements. The findings illustrate the sensitivity of TMDC materials to temperature-induced changes and form a central part of the dissertation's methodological innovation in optical spectroscopy.

Nanoscale

PAPER

View Article Online
View Journal | View Issue

Cite this: *Nanoscale*, 2025, **17**, 16818

Thermotransmittance spectroscopy of layered crystals using lab on fiber†

K. Ciesiołkiewicz, * J. Kopaczek and R. Kudrawiec *

Received 21st January 2025,
Accepted 29th May 2025

DOI: 10.1039/d5nr00301f

rsc.li/nanoscale

Transition metal dichalcogenides are extensively studied for their unique optical properties, with emission and reflectance techniques commonly used to probe optical transitions. In this context, a thermotransmittance technique is introduced as a novel method to investigate the transmission and absorption properties of thin TMDC crystals transferred onto the core of multimode optical fibers. Using transmission and photomodulated transmission techniques, significant changes in the amount of transmitted light, reaching almost 60%, were detected. These changes, evoked by laser heating and subsequent heat accumulation, correspond to excitonic transitions. The obtained results indicate significant red shifts and changes in absorption coefficients around optical transitions, highlighting the materials' sensitivity to temperature variations. As the laser illumination of the sample causes either an energy shift of optical transition or a change in the amount of transmitted light, these findings demonstrate that the TMDC-coated optical fibers could be utilized as light modulators or temperature sensors.

Introduction

The discovery of graphene in 2004 by scientists Andre Geim and Konstantin Novoselov at the University of Manchester[1] marked the beginning of a new era in materials science and nanotechnology.[2–4] Following the discovery of graphene, interest in other 2D materials soared, leading to the investigation of various materials with unique electronic,[5] optical,[6] and mechanical[7] properties. Among layered materials, transition metal dichalcogenides (TMDCs) have emerged as up-and-coming candidates for a wide range of optoelectronic applications.[8,9] Notable examples include molybdenum (Mo) and tungsten (W) combined with sulfur (S) or selenium (Se), which exhibit intriguing properties that make them attractive for technological advancements. TMDCs are characterized by strong covalent bonds within the layer and weak van der Waals bonds between adjoining layers, which makes them, like graphene, easy to isolate as monolayers through mechanical exfoliation.[10] One of the most important features of TMDCs is their ability to transition from an indirect to a direct bandgap semiconductor when thinned down to monolayer form,[11,12] while still strongly interacting with light.[11] This transition has significant implications for their optoelectronic properties and potential applications.[8,13,14] In particular, the spectral range for these materials typically falls between 1.55 to 2.00 eV,[15] rendering them suitable for various optoelectronic devices.[8,14] Furthermore, TMDCs exhibit compatibility with silicon substrates, facilitating their integration into existing semiconductor technologies.[9,16] The mentioned properties, combined with their ease of manipulation and unique electronic structure,[17] position TMDCs as promising candidates for the development of optoelectronic devices.[18,19]

Another commonly used platform that is highly compatible with TMDC materials is optical fibers. These two scientific areas are increasingly being integrated.[20] Optical fibers, renowned for their proficiency in light propagation, have limited use in applications such as photodetectors and sensors due to their material properties. However, integrating TMDC materials can overcome these limitations and enable new functionalities in optoelectronics.[8,20] Moreover, fiber optics provide an excellent platform for light–matter coupling and, when integrated with 2D materials, allow the fabrication of compact and flexible optoelectronic devices.[8,20–22] The popular ones are optical modulators,[23,24] photodetectors[25,26] and sensors.[23,27,28]

On the other hand, fiber optics, with their numerous advantages, can also be valuable for material characterization. One group of techniques widely used to study the optical properties of semiconductors is modulation spectroscopy, which, due to its differential nature, provides precise information about the optical transitions of the studied materials.[29] Modulation spectroscopy, in its traditional approach, can be performed in both transmission and reflection modes,[30] where internal parameters such as built-in electric field,[31] strain,[32] or

Department of Semiconductor Materials Engineering, Wroclaw University of Science and Technology, Wybrzeże Wyspiańskiego 27, 50-370 Wrocław, Poland.
E-mail: karolina.ciesiolkiewicz@pwr.edu.pl, robert.kudrawiec@pwr.edu.pl

† Electronic supplementary information (ESI) available. See DOI: https://doi.org/10.1039/d5nr00301f

temperature[33] are slightly perturbed to obtain differential-like spectra with so-called resonances corresponding to optical transitions. Moreover, modulation techniques, alongside other commonly used optical methods such as PL, reflectance, or Raman spectroscopy, can be equally well employed to study material properties under the influence of various external factors, such as strain,[34] temperature,[35] and pressure,[15,36] as well as magnetic fields,[37,38] with each parameter varied across a broad range. These techniques provide detailed insights into the optical response of semiconductors and other materials. As mentioned, a commonly used approach to obtain modulation spectra is temperature perturbation (thermoreflectance), where the material is typically heated using a Peltier element[39] or resistive heater.[40] In addition, it has been shown that lasers can also be used to induce both significant and subtle changes in material properties.[41–43]

In this work, we propose a novel approach to lab-on-fiber measurements. Here, one of the methods that could benefit from combining it with optical fibers is optical transmission, based on which it is possible to estimate the absorption characteristics of studied materials.[44] Furthermore, photomodulated transmission, a differential technique that allows obtaining information about direct optical transitions over a broad spectral range,[45] could also be coupled with fibers. So far, these techniques have primarily been used to determine the fundamental band gap of semiconducting materials, as it is challenging to obtain a sample thin enough to allow light with energy higher than the band gap to transmit through due to stronger absorption.[30] As mentioned, this phenomenon is related to the energy dependence of the absorption coefficient. Namely, a large increase in absorption is observed just above the bandgap and at higher energies, significantly reducing the initial intensity of light to a non-measurable level. Thinning down materials like van der Waals (vdW) crystals allows higher energy light to pass through and, therefore, to observe the transmission signal for this spectral range. In such a case, when analyzing the absorption spectra, optical transitions A and B (and even C) in TMDC crystals can be clearly observed, as shown in our studies. One of the approaches to the problems discussed above is the use of optical fibers in transmission measurements. Optical fiber, when light is introduced into its core, provides an attractive platform for creating microlaboratories, known as lab-on-fiber (LOF).[21,46] In our study, the standard surface of a flat optical fiber tip is 125 μm in diameter, and the core itself is 50 μm. Generally, obtaining a thin sample of these dimensions is not challenging. By covering the entire surface of the core with a thin layer of vdW crystals, the absorption of the light transmitted through it can be easily measured across a broad spectral range. Moreover, this approach allows for the measurement from a few layers down to even monolayers. Additionally, using fibers in optical measurements can simplify the experimental setup and enable the decoupling of the measurement zone from the sample location. So far, this approach, *i.e.*, placing TMDCs on fiber, has been utilized once in optical measurements of WSe_2 monolayer in a magnetic field.[47] However, modulation spectroscopy techniques in such an experimental configuration have not been studied and reported.

Furthermore and most importantly, we demonstrate the use of an illuminating laser beam in transmission measurements to induce reversible changes in absorption spectra through controlled heating, thereby providing insight into the effects of temperature changes in the studied sample. All the measurements were conducted on the four most commonly studied TMD crystals, namely, MoS_2, $MoSe_2$, WS_2, and WSe_2, allowing us to focus on the thermal effects evoked by laser heating, as their optical properties are already well known. Each sample was measured at room temperature, with the power of the backlighting laser varying from 0 to 40 mW. The changes in the optical response, in terms of light absorbed by the studied material and induced by laser heating, were measured using a portable spectrometer. Moreover, modulation measurements, in which the laser light was periodically blocked and unblocked using a mechanical chopper, were employed. This approach subsequently allowed us to directly measure the effect of temperature variations on the intensity of transmitted light using the lock-in technique. We, therefore, propose a new thermotransmittance method that involves directly heating the sample using only a laser, eliminating the need for an additional heater. This approach allows precise local temperature control and uniquely enables these measurements to be performed in transmission mode using optical fibers.

Sample preparation and experimental setup

In this study, we employed a widely utilized multimode optical fiber characterized by a core dimension of 50 μm and a cladding of 125 μm, the selected for this study optical fibers operate in the spectral range of 400–2400 nm. To prepare the crystals for measurements, the mechanical exfoliation method was used, as it is known for its efficiency in obtaining thin layers of vdW materials.[12] Through this method, it was possible to achieve the desired reduction in sample thickness in order to make them semitransparent for light. Following the preparation stage, samples with optimal dimensions to align with the core diameter of the fiber and reduced thickness, enabling light to transmit through the crystals and still be detectable, were selected. Once the appropriate samples were identified on PDMS, a transfer process was carried out under the microscope. In this case, we relied on the well-known deterministic transfer method, commonly used for placing crystals on desired substrates such as *e.g.*, Si/SiO_2.[48] Establishing this approach in the context of optical fibers yields good results and demonstrates new possibilities. The materials were positioned onto the cleaved end-face of the optical fiber, a task that required precision to ensure proper alignment and adherence. The final alignment procedure was performed using a stage equipped with *x*–*y*–*z* adjustments controlled by micrometer screws.

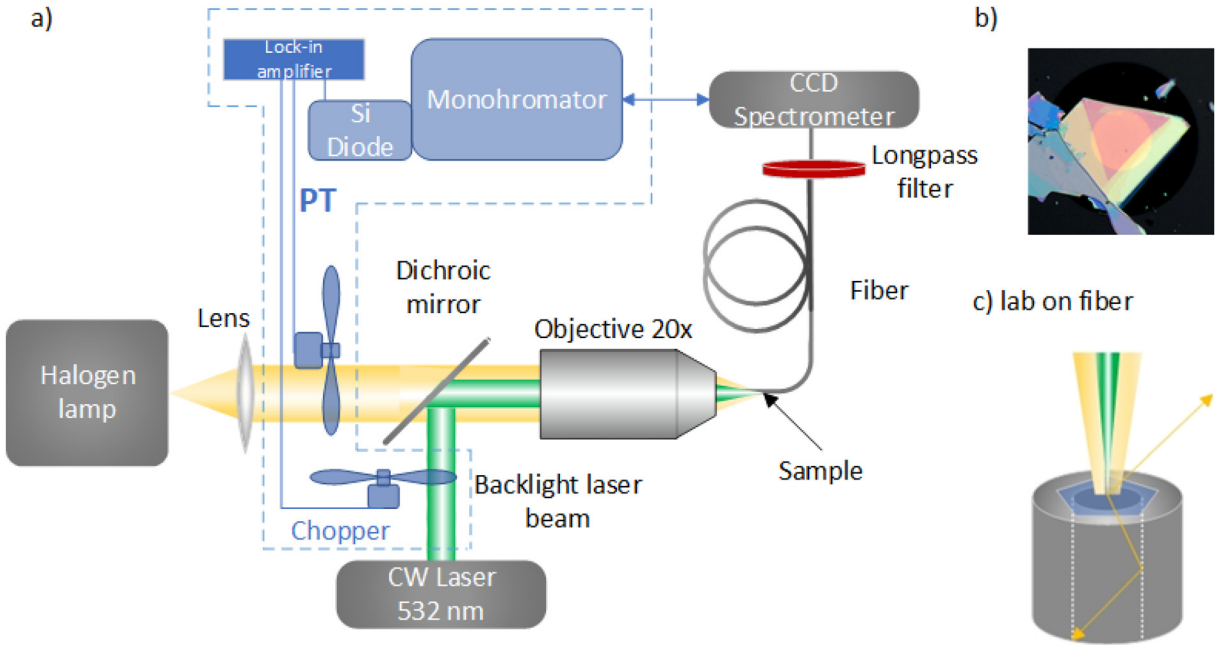

Fig. 1 (a) Schematic of the experimental setup for transmission measurements using an integrated optical fiber. Blue elements in dashed frames correspond to the configuration of the setup for modulated transmission. (b) Detailed view of the end face of the optical fiber, showing the measured sample. The bright orange circle represents the light transmitted through the sample. (c) Close-up schematic of the fiber tip, illustrating how the thin samples of the measured materials are positioned to cover the core of the optical fiber. The green and yellow cones represent the laser (pump beam, inducing changes in the transmitted light) and the light emitted from the halogen lamp (probe beam), respectively.

The optical fiber with the sample placed on it using the methodology described above was integrated into a transmission setup (Fig. 1). In this setup, a quartz tungsten halogen (QTH) lamp was used as the source of the probe beam, and the light transmitted through the sample was directly detected by a portable CCD spectrometer. On the other hand, conducting a modulated experiment requires adding the elements enclosed in the blue dotted frame to the setup. The continuous wave (CW) laser operating at 532 nm was used to induce changes in the internal parameters of the studied materials, thereby causing modulation of the transmitted light. Moreover, the lock-in technique was utilized to collect mentioned changes in the transmission spectra, which correspond to optical transitions. Both the light from the laser and the QTH lamp were precisely focused onto the end face of the optical fiber, with the sample on it, using a 20× micro-objective lens. The size of the laser spot focused on the sample is 10 μm in diameter (this value is above the diffraction limit and is attributed to the underfilling effect[49,50]). To ensure that the laser did not disturb the spectral range of interest, a 550 nm long-pass filter was implemented. The use of optical fiber in the experimental setup offered several significant advantages, including improved signal quality and flexibility in positioning the sample zone. Additionally, it allowed us to eliminate numerous optical components, such as mirrors and lenses, which are typically necessary to direct light in conventional setups without optical fibers. This simplified experimental arrangement and also reduced potential sources of alignment errors. Consequently, the optical fiber facilitated the direct guidance of the signal from the sample to the detector, thereby enhancing the efficiency of our measurements.

Rapid optical transmission determination and thermal effects in TMDCs integrated with optical fiber

Firstly, transmission measurements on several well-known TMDC crystals using a spectrometer configuration (Fig. 1a) were conducted. The materials investigated included thin film (10–100 nm) of MoS_2, $MoSe_2$, WS_2, and WSe_2, which are semi-transparent for light. In the absorption spectra shown in Fig. 2, we observed distinct excitonic transitions, exciton A_K and exciton B_K for MoS_2 and $MoSe_2$, and exciton A_K for WS_2 and WSe_2. Observing these features indicates strong excitonic absorption within the studied materials and provides insight into their optical properties. For MoS_2 Fig. 2a, in the room temperature absorption spectra, the two measured features corresponding to the A_K and B_K excitonic transitions are located at approximately 1.843 eV and 2.003 eV, respectively. Similarly, $MoSe_2$ exhibited A and B excitonic transitions but at lower energies, around 1.543 eV and 1.803 eV, Fig. 2b. All these transitions are characterized by a significant increase in absorption coefficient, highlighting the presence of strong excitonic absorption. The absorption spectra calculated from

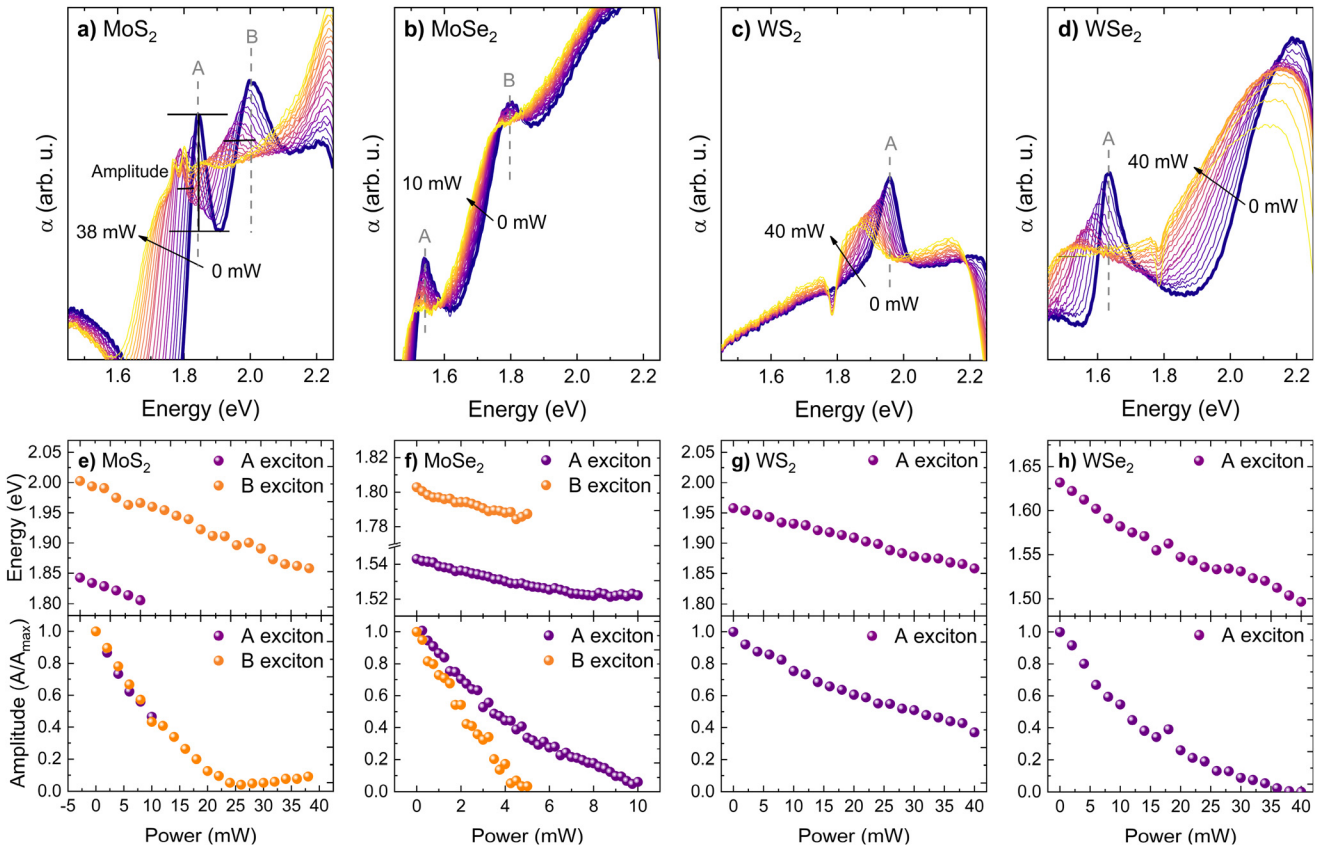

Fig. 2 Absorption spectra of the MoS_2 (a), $MoSe_2$ (b), WS_2 (c), and WSe_2 (d) obtained with the increasing power of the backlight laser beam. The dependence of energy of excitonic transitions and the absorption coefficient at these energies on applied laser power is shown in the panel: (e) for MoS_2, (f) for $MoSe_2$, (g) for WS_2, and (h) for WSe_2.

transmission measurements of WS_2 and WSe_2 (Fig. 2c and d) showed a single excitonic transition, the A exciton, at 1.958 eV for WS_2 and 1.632 eV for WSe_2. The absence of the B transition for tungsten-based crystals is related to a lower sensitivity of the experimental setup in this spectral range. All the energies of the excitonic transitions estimated from room temperature absorption spectra are summarized in Table 1.

Table 1 Energies (E_0) of excitonic transitions obtained at room temperature. The α and β coefficients describe energy shifts induced by temperature or laser power. The γ coefficient indicates the relationship between laser power and the temperature change it evokes

Sample	Transition	E_0 (eV)	α (10^{-4} eV K^{-1}) (ref. 51)	β (10^{-3} eV mW^{-1})	γ (K mW^{-1})
MoS_2	A_K	1.843	4.8	3.7	7.8
	B_K	2.003	6.2	3.8	6.1
$MoSe_2$	A_K	1.543	4.4	2.1	4.8
	B_K	1.803	5.7	3.1	5.4
WS_2	A_K	1.958	4.5	2.5	5.5
WSe_2	A_K	1.632	4.4	3.4	7.7

To induce and study changes in optical response, specifically in the absorption coefficient, a laser beam was employed with incremental power steps tailored to each material: a 2 mW step for MoS_2, WSe_2, and WS_2, and a finer 0.25 mW step for $MoSe_2$. The laser beam illuminated the sample while transmission spectra were collected using a portable spectrometer, allowing the entire spectrum to be obtained at once after a set accumulation time. Throughout these measurements, a redshift in the energy of excitonic transitions for all studied materials was consistently observed, as shown in Fig. 2e–h. This redshift was attributed to the heating of the samples that were located at the tip of the optical fiber. In this case, the focused laser beam induces localized heating, leading to observed changes in the optical properties of the materials, referred to later in the text as the thermal effect. Despite the redshift of exciton energies with temperatures, a decrease in absorption coefficient at these energies was observed and is shown quantitatively in the bottom part of Fig. 2e–h. The changes in both energy and amplitude induced by heating the studied crystals were accompanied by spectral broadening of the optical transitions. To investigate this effect further, the linewidth of a selected TMDC sample (WSe_2) was analyzed at different laser powers corresponding to increasingly higher

temperatures. For example, at 0 mW, the linewidth was calculated to be 84 meV. At 10 mW, it increased to 107 meV, reaching a maximum value of 153 meV at 40 mW (which corresponds to ~607 K). Fig. S2 of the ESI† presents the excitonic transitions with increasing broadening.

The mentioned thermal effect was observed because (i) the studied thin TMDC materials have a low heat capacity, resulting from the small volume of the crystals due to their low thickness, and (ii) poor thermal conductivity between the crystal and the optical fiber. In such a situation, when a laser illuminates material, the absorbed energy causes rapid and high temperature variations. This occurs since, as mentioned, limited thickness restricts heat conduction away from the spot where the laser illuminates the material. Moreover, the small area of the sample, which is only slightly larger than the diameter of the core of the optical fiber and laser beam, further limits lateral heat dissipation. These spatial constraints, specifically the small sample volume, result in high heat accumulation, significantly increasing the local temperature. Additionally, the optical fiber on which the TMDC thin layer is placed is made of glass, which has low thermal conductivity. This makes it less effective at drawing heat away from the vdW crystal. Consequently, the heat generated by the laser also remains within the TMDC layer rather than being conducted away through the glass substrate. In this case, the glass substrate acts more like an insulator, hindering the transfer of heat away from the material (a more detailed discussion on thermal effect is added in the ESI†). The maximum laser power reached in this study was 40 mW, corresponding to a temperature of 607 K, as estimated based on the energy shift of optical transitions and their temperature coefficients reported in previous studies.[51] Above this threshold, sample degradation or thinning was observed. Importantly, within the 0–40 mW range, no damage is expected. Moreover, the observed degradation at 40 mW (~607 K) is consistent with other studies reporting that temperatures exceeding 600 K are required to induce sample thinning.[52] For these reasons, it can be concluded that the observed energy shift of excitonic transitions is primarily related to thermal effects.

For the purpose of quantifying the thermal effect on the exciton energy redshift shown in Fig. 2, a linear fit was used for each dependency. Table 1 shows the β coefficients representing the energy shift per 1 mW of laser power obtained from the linear fit for each optical transition and material. For example, for MoS_2, the energy shift, *i.e.*, β coefficient, is equal to 3.72 meV mW^{-1} for transition A_k and 3.8 meV mW^{-1} for transition B_k. These values highlight the pronounced responsiveness of the studied materials to changes in laser power. On the other hand, the temperature coefficient α, which describes the energy shift in TMDC materials with temperature, was determined in our previous studies.[51] This allowed us to establish a direct relationship between laser power and the induced temperature changes, represented by the γ coefficient in Table 1. The performed analysis indicated that MoS_2 is highly sensitive to both laser power and, at the same time, temperature fluctuations, as evidenced by the largest energy shift. Additionally, we observed that for MoS_2 and WSe_2, the changes in absorption spectra were most prominent, with optical features corresponding to excitonic transitions completely diminishing at the highest laser power.

The findings described above show that an optical fiber with a TMDC crystal placed on its tip could serve as either a light modulator or a sensor. For light modulation, it was demonstrated that the amount of transmitted light can be significantly reduced by simply illuminating the material with a laser. On the other hand, tracking the energy position could possibly allow for temperature determination. However, regardless of the application, it is crucial to calibrate such a device, as its optical response can vary slightly based on material composition or thickness.

Modulated transmission for optical transition analysis in TMDC crystals

Modulated transmission is one of the methods used to measure optical transitions of semiconductors. These transitions are represented in spectra by features that correspond to changes in absorption coefficient.[45,53,54] Moreover, the mentioned changes are obtained with respect to the amount of light transmitted when the sample is not illuminated by the laser, *i.e.*, the unperturbed absorption coefficient shown by the thick blue lines in Fig. 2a–d. The modulated measurements were performed at room temperature using the experimental system configuration, incorporating elements from the blue-dashed frame shown in Fig. 1. In this case, the spectrometer was replaced by a monochromator (Triax 320), to which an optical fiber was coupled. The dispersed signal from the monochromator was detected subsequently by a Si diode in the point-by-point mode. Furthermore, the signal, representing a change in the intensity of light transmitted through the sample, was measured using the lock-in technique with a reference signal from a mechanical chopper. Finally, the obtained results were compared with their simulated spectra obtained using $(T - T_0)/T$ formula, where T and T_0 are transmission spectra collected with and without the backlight 532 nm laser beam, respectively. Notably, both T and T_0 were collected across the entire spectral range at once using the portable spectrometer.

Moreover, it is important to note that the shape of the spectra collected using the two approaches mentioned above will, in general, differ (compare, *e.g.*, Fig. 3a *vs.* 3b). In the case of the method based on a portable spectrometer, the rapidly determined $\Delta T/T$ spectrum is also influenced by background signals across the entire energy range, which is not fully eliminated by normalization to a reference spectrum. In contrast, modulated transmission measurements rely on lock-in detection, where only the signal modulated at the chopper frequency (280 Hz in this case) is recorded. Furthermore, changes in the transmission spectrum appear only at energies corresponding to optical transitions. As a result, the background signal is suppressed, and the resonance appears cen-

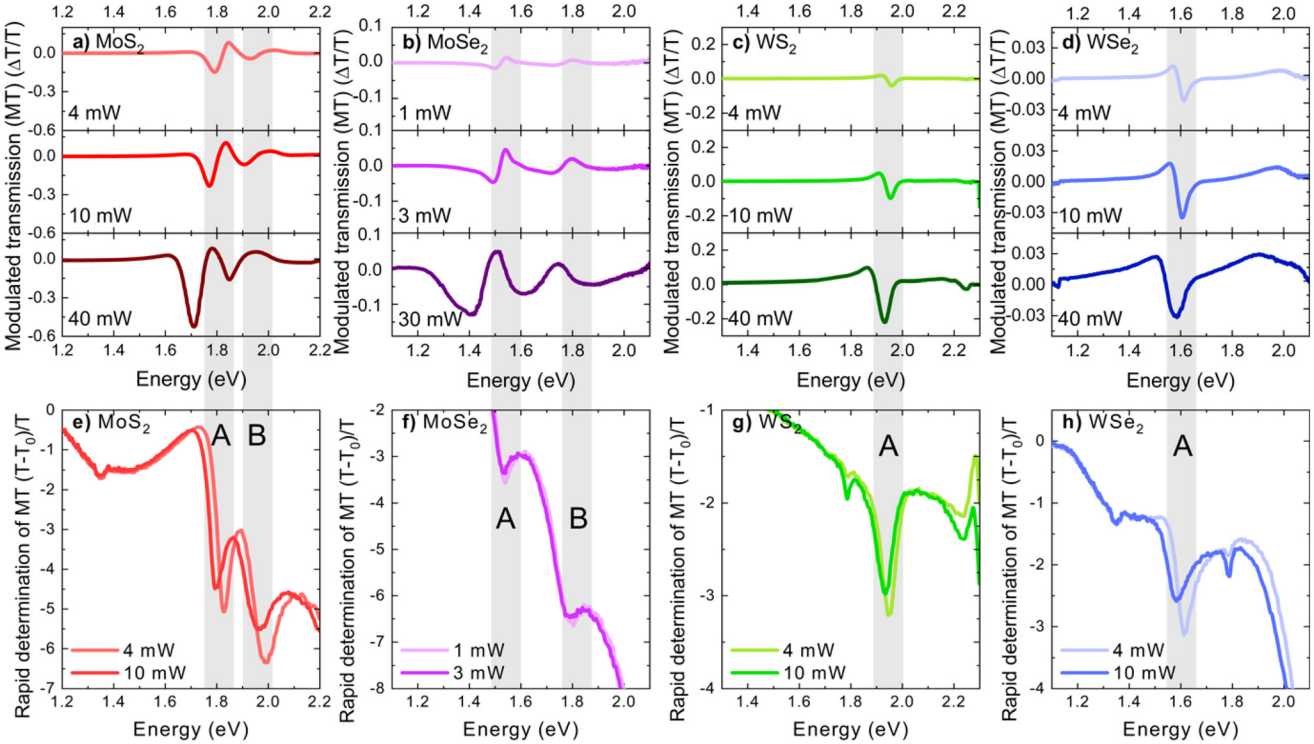

Fig. 3 Modulation spectra of four different transition metal dichalcogenides: MoS_2 (a), $MoSe_2$ (b), WS_2 (c), and WSe_2 (d) collected at different laser powers, and results of simulated modulation experiments performed for the MoS_2 (e), $MoSe_2$ (f), WS_2 (g), and WSe_2 (h) with the use of a spectrometer. The gray rectangular area represents the energy position of the A and B excitonic transitions obtained with low laser power.

tered around zero on the signal (y) axis, leading to a different spectral shape.

The results of the modulated experiment conducted with different laser powers for each of the studied crystals are shown in Fig. 3. As previously mentioned, the observed changes in the intensity of transmitted light in the spectra correspond to direct optical transitions. Here, these are the A and B excitonic transitions for Mo-based TMDCs and the A transition for W-based crystals. The energies of observed transitions agree well with the absorption spectra (Fig. 2) derived from measurements obtained using the first experimental configuration with a CCD spectrometer. It is also worth noting that the amplitude of the optical features/resonances is significant. Changes in the transmitted light for MoS_2 are the largest, reaching up to 60% with a laser beam power of 40 mW, and even at 4 mW, they are around 20% at the energy of the A transitions. This was also observed in Fig. 2 for MoS_2, where the reduction of the absorption coefficient at higher laser power was significant. In the modulation experiment, that change, *i.e.*, between the amount of light transmitted at, *e.g.*, 0 and 40 mW, was directly measured. Additionally, each optical transition is redshifted due to the increased laser power and stronger heating. These results demonstrate the high efficiency of the modulation method in directly determining changes in the intensity of transmitted light and observing optical transitions. Furthermore, the measurements revealed that, in addition to built-in electric field modulation, thermomodulation is the dominant factor in inducing changes in the transmission spectra (this aspect is discussed in the following section).

When comparing the two experimental methods, namely, modulation measurements and their simulated counterparts, it was concluded that the results and observed effects were highly consistent. However, for a quick assessment and determination of any changes in the material properties, the simulated approach using a spectrometer takes much less time, completing measurements within milliseconds. The only requirement is that the measured changes are at least on the order of around 0.3%. On the other hand, the modulation method, which utilizes the lock-in technique, is very sensitive, as modulated reflectance, detecting changes at the level of 10^{-5} to 10^{-6}. However, collecting each spectrum requires more time, ranging from minutes to hours. Lastly and most importantly, the evoked changes are reversible within the applied laser power range, allowing for re-measurement and re-use of the fiber with the sample on it.

Effect of temperature and built-in electric field modulation on absorption

In order to separate the influences of internal electric field modulation and thermal effects induced by laser heating, com-

prehensive experiments were devised. This is because illuminating the studied crystal with a laser induces not only temperature changes but also modulates the internal built-in electric field in the semiconductor crystal. The presence of the built-in field arises from the difference in the Fermi level position at the surface compared to its energy location within the sample caused by surface states.[55] As a result, when the laser shines on the sample and excites the electron–hole pairs, they are separated spatially by the internal electric field, causing a reduction in the strength of that built-in field. This is the basic principle of photoreflectance spectroscopy.[30] Here, in the first experiment, two laser beams were directed onto the $MoSe_2$ sample simultaneously: one with 1 mW power modulated by a mechanical chopper for direct determination of absorption changes using the lock-in technique and the second unmodulated backlight beam but with incrementally increased power for each separate measurement (from 0 to 16 mW with steps of 4 mW). The results of this experiment are presented in Fig. 4a, with the quantitative analysis included in Fig. 4d. It was revealed that the additional backlight (not modulated) beam is causing a redshift of optical transitions due to the laser heating. At higher backlight beam power (*e.g.*, 16 mW), the amplitude of both transitions decreases because the energy provided by the modulated beam (1 mW), which induces changes in transmission, no longer causes significant temperature modulation compared to the constant temperature increase from the backlight beam. Furthermore, due to the photovoltaic effect, the reduction of the internal electric field would also lead to a smaller amplitude of optical transitions. However, such a large energy shift, as observed in Fig. 4d, is not expected in this case, suggesting that temperature modulation plays a more dominant role in evoking absorption changes.

Results of the second experiment, where only one beam, modulated by a mechanical chopper, was used to illuminate

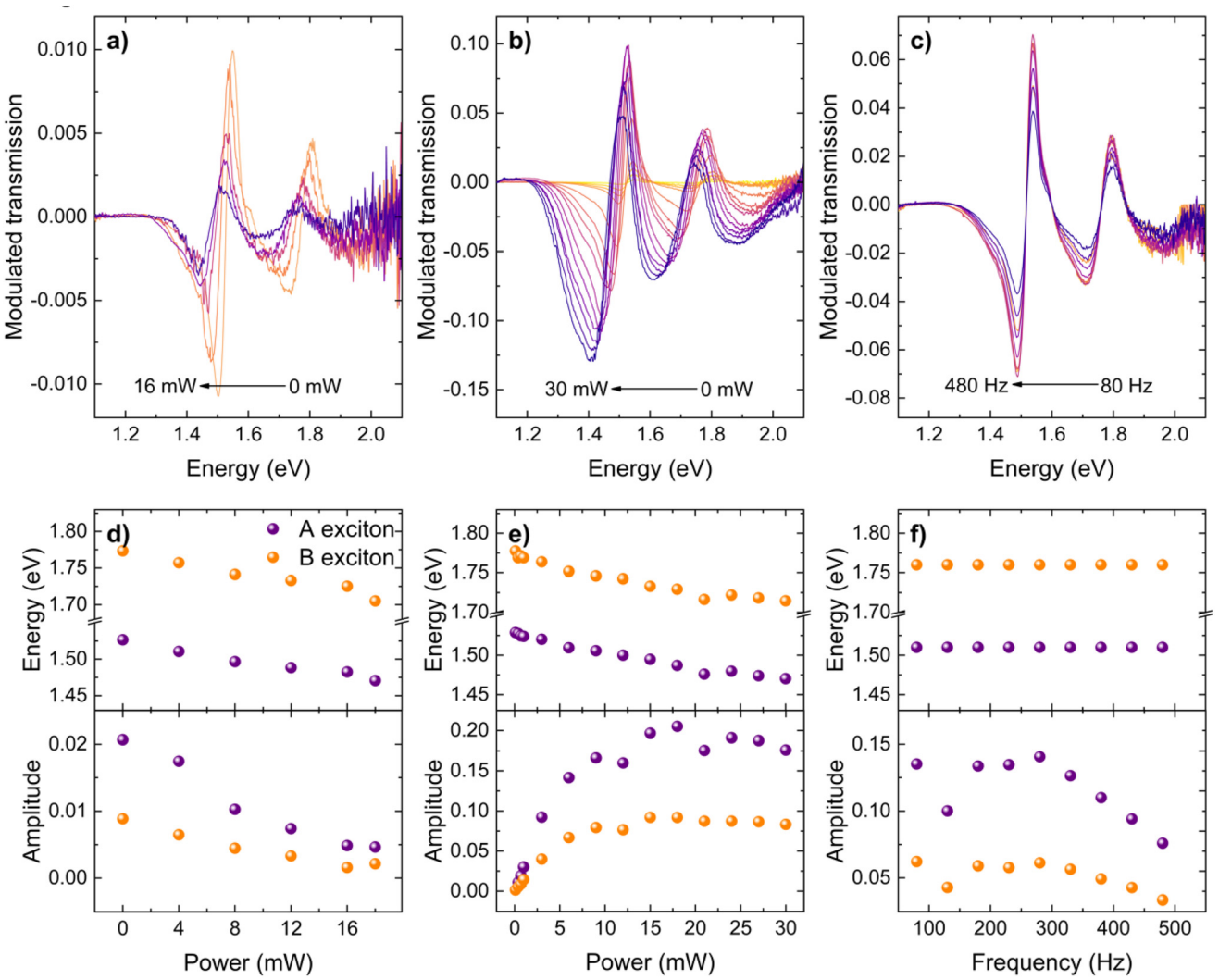

Fig. 4 (a) Modulation spectra of $MoSe_2$ crystal obtained in the configuration with an additional heating (backlight) laser beam. (b) Dependence of the spectra on the laser power of one modulated laser beam. (c) Modulation spectra obtained at different frequencies in the one-beam experiment. (d), (e) and (f) present the results of the analysis for the spectra included in panels (a), (b), and (c), respectively.

the sample, are shown in Fig. 4b. The presented spectra were collected with laser power steps of 3 mW. It can be seen that changes in the amount of transmitted light increase with the power of the laser beam, reaching around 12% for 30 mW. These changes occur at the energy of optical transitions, which redshift as a result of the thermal effect, as shown in the top panel of Fig. 4e. Moreover, the amplitude of these changes increases and then starts to saturate at around 15 mW (Fig. 4e, bottom panel). At this power, the rate of energy redshift also decreases. Such behavior may indicate that the maximum temperature variation is reached at a power of around 15 mW. Remarkably, even at relatively low powers, like 100 μW, significant changes are observed in the spectrum, including the amount of transmitted light and the redshift of the corresponding optical transitions. The observed changes in transmitted light at the energy of the optical transition in the experiment with 100 μW laser power reached approximately 3% (Fig. S5 in the ESI†). This proves the high sensitivity of the studied system, which consists of a TMDC crystal placed on top of the fiber tip. Furthermore, the applied range of low laser powers ensures the safety of the sample from potential damage due to overheating, making it invaluable for experimental and practical applications. It is also important to note that all of the observed changes were reversible.

Further studies focused on measurements with varying modulation frequencies in the one-beam experiment, the results of which are included in Fig. 4c and f. The spectra were collected with frequencies in the range of 80 to 480 Hz, while the power of the laser was set to 4 mW. It was shown that the observed changes in transmission do not shift spectrally, and the energy of the optical transitions remains nearly constant. This indicates that the average temperature of the sample is independent of the modulation frequencies, as shown schematically in Fig. S1 in the ESI.† Although the energy of the transitions remained constant, the signal amplitude started to decrease at 280 Hz following initial saturation (Fig. 4f, bottom panel). The decrease in signal amplitude can be caused by the decrease in the modulation amplitude of temperature and/or the modulation amplitude of the built-in electric field. In general, it can be expected that thermal processes are slower than electrical processes, which in this case are determined by the dynamics of occupation of defect states at the crystal surface/interface. To check this, photoreflectance measurements were performed for various frequencies for bulk $MoSe_2$ crystals. In this experiment, the studied samples were millimeter-sized and placed on a copper holder using silver paint to minimize thermal effects. Similarly, the results obtained for the bulk crystal showed decreased signal intensity with frequency (Fig. S2†). Since temperature modulation can be excluded, the reduction in signal is attributed to changes in the modulation amplitude of the built-in electric field. This occurs because when the excited electron–hole pair is spatially separated by the internal electric field, causing its simultaneous reduction, one of the carriers moves toward the surface, where a trap state captures it. However, at higher frequencies, this trap state may not empty before the next laser pulse illuminates the sample due to time constraints, reducing signal intensity.[56] That observation indicates that in addition to temperature modulation, internal electric field perturbation contributes to the measured changes in the intensity of transmitted light. The contributions of both effects cannot be easily quantified; nonetheless, it is expected that temperature modulation will become increasingly dominant at higher laser power. For these reasons – *i.e.*, the unknown relative contributions of temperature modulation (the dominant component) *versus* built-in electric field modulation – it is difficult to predict the maximum modulation frequency at which the signal will remain detectable. This is especially true given that other factors, such as the quality of the interface between the fiber and the studied crystal or the volume of the crystal, can affect temperature modulation. However, based on the conducted experiment, it can be estimated that for a thin $MoSe_2$ crystal, the maximum frequency at which it is still possible to distinguish the signal corresponding to optical transitions from background noise could reach around 800 Hz.

Line shape of thermotransmittance

As discussed in the previous section, the influence of both the modulation of the internal electric field and the thermal effect induced by the laser are observed in the transmission spectra. The thermal effect resulting from localized heating of the material leads to changes in the absorption coefficients and other optical properties. These effects have a significantly stronger impact on the transmission spectrum compared to electric field modulation. As the laser power increases, the heat generated by the absorbed laser energy becomes the dominant factor driving changes in the optical characteristics of the studied materials, making the electric field modulation irrelevant at higher powers. The total contribution to the changes in the transmission spectrum can be described by the following equation:

$$\frac{\Delta T}{T} = \left(\frac{\Delta T}{T}\right)_{\Delta F} + \left(\frac{\Delta T}{T}\right)_{\Delta T_K} \quad (1)$$

where T represents transmission, ΔT denotes changes in the transmission, ΔF indicates perturbation of the electric field, and ΔT_K represents the temperature variation. In our case, as previously mentioned, the following inequality can be assumed:

$$\left(\frac{\Delta T}{T}\right)_{\Delta F} \ll \left(\frac{\Delta T}{T}\right)_{\Delta T_K} \quad (2)$$

The resonance profile (related to optical transition) follows a Lorentzian shape, characterized by three key parameters: the center energy E_0 (corresponding to the energy measured without the laser), the resonance broadening Γ (peak half-width, FWHM), and the resonance strength A (oscillator strength)[57,58] (3):

$$L(E) = \frac{A}{{E_0}^2 - E^2 + i\Gamma E} \quad (3)$$

All these three parameters change due to the temperature variation induced by illuminating the studied sample with the laser beam. While Gaussian functions may better describe material inhomogeneities in some cases, Lorentzian fitting is commonly employed due to its simpler mathematical structure, which enables more efficient computation and faster convergence of fitting algorithms. For van der Waals crystals, which under ideal conditions exhibit high structural uniformity, Lorentzian fitting provides sufficiently accurate results while allowing effective analysis of experimental data.[58] In the results, relative changes in transmission can also be described by the following equation:

$$\frac{\Delta T}{T} \propto \frac{\partial T}{\partial A}\frac{\partial A}{\partial T_K}\Delta T_K + \frac{\partial T}{\partial E_0}\frac{\partial E_0}{\partial T_K}\Delta T_K + \frac{\partial T}{\partial \Gamma}\frac{\partial \Gamma}{\partial T_K}\Delta T_K \quad (4)$$

Below, in Fig. 5, the A optical transition measured for WS_2 is presented. This excitonic transition was obtained from transmission measurements with a laser beam of 0 mW and 20 mW power illuminating the studied sample. The graph clearly shows how the spectrum shifts towards lower energies, broadens, and decreases in intensity as the laser power increases according to the expectation. Both of the obtained transitions were fitted with the Lorentzian function to quantify the changes induced by heating. The fitting highlights the gradual broadening of the resonance peak and the reduction in peak intensity, consistent with the expected thermal effects induced by laser heating. Differential signal has the resonance shape, which is approximated by the Aspnes formula:[57]

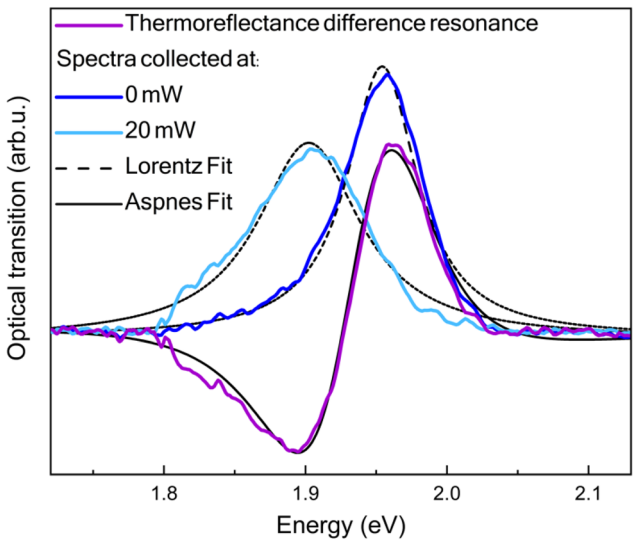

Fig. 5 The optical transition of WS_2 obtained from transmission measurements conducted with laser powers of 0 mW and 20 mW. The spectra exhibit a shift towards lower energies, broadening, and a decrease in amplitude with increasing laser power. The overlaid Lorentzian fitting (dashed lines) was applied to illustrate the changes in the transition shape.

$$\frac{\Delta T}{T}(E) = \mathrm{Re}[Ae^{i\theta}(E - E_0 + i\Gamma)^{-m}] \quad (5)$$

where θ is the phase factor, and m represents the type of optical transition.[30] The effect of varying individual parameters of the Lorentzian function (Fig. S4) is discussed in the ESI.†

Summary

This study introduces a novel measurement technique, *i.e.*, thermotransmittance spectroscopy of layered crystals, using a lab-on-fiber approach. Thin, semitransparent samples of MoS_2, $MoSe_2$, WS_2, and WSe_2 were prepared using mechanical exfoliation and deterministically transferred onto the fiber end-face. Subsequently, rapid transmission measurements, performed using a portable spectrometer, allowed for the extraction of absorption spectra while the studied samples were illuminated with increasingly higher laser power. Due to the low heat capacity of thin TMDC materials and poor thermal dissipation to glass optical fibers, the laser caused localized heating, leading to a significant temperature increase. This thermal effect resulted in the redshift of A and B excitonic transitions and a decrease in the absorption coefficient (reaching almost 60%) at energies corresponding to these transitions.

The laser-induced changes in transmitted light were also directly measured using modulated transmission spectroscopy, employing different configurations and varying laser powers. The obtained results were compared with their simulated counterparts, both of which demonstrated significant changes in light transmission at energies corresponding to optical transitions. Furthermore, the laser power strongly affected the spectral position of these transitions, with the shift associated with thermal effects. Additionally, changes in transmitted light were primarily driven by temperature modulation, with a negligible contribution from internal electric field modulation, which is why the applied method is referred to as thermotransmittance. Moreover, in the studied material system, the sensitivity of the spectrometer measurements enabled the rapid determination of spectral shifts or changes in transmitted light intensity.

Overall, our comprehensive study demonstrated that TMDC crystals positioned on the core of an optical fiber tip could serve as temperature sensors or optical modulators. In the future, this system holds potential for further development in various applications, including measurements under external electric and magnetic fields, where the interaction between the magnetic field and excitonic transitions as a function of temperature could be explored. Lastly, it can expand the range of experimental conditions available for the study of TMDC materials.

Data availability

The data supporting this article are included in the ESI.† This includes a diagram illustrating temperature variations over time at two different modulation frequencies, as well as a figure presenting the photoreflectance spectra of $MoSe_2$ obtained in the one-beam experiment.

Conflicts of interest

The authors declare no conflicts of interest.

Acknowledgements

This work was supported by project No. 2020/39/B/ST3/02704 (OPUS20) from the National Science Centre in Poland.

References

1 A. K. Geim and K. S. Novoselov, *Nat. Mater.*, 2007, **6**, 183–191.
2 R. Mas-Ballesté, C. Gómez-Navarro, J. Gómez-Herrero and F. Zamora, *Nanoscale*, 2011, **3**, 20–30.
3 S. Z. Butler, S. M. Hollen, L. Cao, Y. Cui, J. A. Gupta, H. R. Gutiérrez, T. F. Heinz, S. S. Hong, J. Huang, A. F. Ismach, E. Johnston-Halperin, M. Kuno, V. V. Plashnitsa, R. D. Robinson, R. S. Ruoff, S. Salahuddin, J. Shan, L. Shi, M. G. Spencer, M. Terrones, W. Windl and J. E. Goldberger, *ACS Nano*, 2013, **7**, 2898–2926.
4 F. H. L. Koppens, T. Mueller, Ph. Avouris, A. C. Ferrari, M. S. Vitiello and M. Polini, *Nat. Nanotechnol.*, 2014, **9**, 780–793.
5 T. Dutta, N. Yadav, Y. Wu, G. J. Cheng, X. Liang, S. Ramakrishna, A. Sbai, R. Gupta, A. Mondal, Z. Hongyu and A. Yadav, *Nano Mater. Sci.*, 2024, **6**(1), 1–23.
6 G. Wang, A. Chernikov, M. M. Glazov, T. F. Heinz, X. Marie, T. Amand and B. Urbaszek, *Rev. Mod. Phys.*, 2018, **90**, 021001.
7 J. H. Kim, J. H. Jeong, N. Kim, R. Joshi and G.-H. Lee, *J. Phys. D: Appl. Phys.*, 2019, **52**, 083001.
8 S. Yu, X. Wu, Y. Wang, X. Guo and L. Tong, *Adv. Mater.*, 2017, **29**, 1606128.
9 J. Y. Lee, J.-H. Shin, G.-H. Lee and C.-H. Lee, *Nanomaterials*, 2016, **6**, 193.
10 R. Bian, C. Li, Q. Liu, G. Cao, Q. Fu, P. Meng, J. Zhou, F. Liu and Z. Liu, *Natl. Sci. Rev.*, 2022, **9**, nwab164.
11 E. M. Vogel and J. A. Robinson, *MRS Bull.*, 2015, **40**, 558–563.
12 M. Tamulewicz-Szwajkowska, S. J. Zelewski, J. Serafińczuk and R. Kudrawiec, *AIP Adv.*, 2022, 12, 025328.
13 K. Thakar and S. Lodha, *Mater. Res. Express*, 2020, **7**, 014002.
14 Electronics and optoelectronics of two-dimensional transition metal dichalcogenides | Nature Nanotechnology, https://www.nature.com/articles/nnano.2012.193, (accessed July 10, 2024).
15 F. Dybała, M. P. Polak, J. Kopaczek, P. Scharoch, K. Wu, S. Tongay and R. Kudrawiec, *Sci. Rep.*, 2016, **6**, 26663.
16 N. Youngblood and M. Li, *Nanophotonics*, 2017, **6**, 1205–1218.
17 A. Castellanos-Gomez, X. Duan, Z. Fei, H. R. Gutierrez, Y. Huang, X. Huang, J. Quereda, Q. Qian, E. Sutter and P. Sutter, *Nat. Rev. Methods Primers*, 2022, **2**, 1–19.
18 B. Sun, J. Xu, M. Zhang, L. He, H. Zhu, L. Chen, Q. Sun and D. W. Zhang, *Crystals*, 2018, **8**, 252.
19 H.-L. Liu, T. Yang, J.-H. Chen, H.-W. Chen, H. Guo, R. Saito, M.-Y. Li and L.-J. Li, *Sci. Rep.*, 2020, **10**, 15282.
20 Silica optical fiber integrated with two-dimensional materials: towards opto-electro-mechanical technology | Light: Science & Applications, https://www.nature.com/articles/s41377-021-00520-x, (accessed December 3, 2023).
21 Y. Xiong and F. Xu, *Adv. Photonics*, 2020, **2**, 064001.
22 G. Kostovski, P. R. Stoddart and A. Mitchell, *Adv. Mater.*, 2014, **26**, 3798–3820.
23 H. Ahmad, H. S. Lim, M. Z. MatJafri, Y. Q. Ge, H. Zhang and Z. C. Tiu, *Infrared Phys. Technol.*, 2019, **102**, 103002.
24 J. Du, Q. Wang, G. Jiang, C. Xu, C. Zhao, Y. J. Xiang, Y. Chen and S. Wen, *Sci. Rep.*, 2014, **4**, 6346.
25 Y.-F. Xiong, J.-H. Chen, Y.-Q. Lu and F. Xu, *Adv. Electron. Mater.*, 2019, **5**, 1800562.
26 J. Chen, Z. Liang, L. Yuan, C. Li, M. Chen, Y. Xia, X. Zhang, F. Xu and Y. Lu, *Nanoscale*, 2017, **9**, 3424–3428.
27 Y. Dogan and I. Erdogan, *Opt. Quantum Electron.*, 2023, **55**, 1066.
28 D. Hlushchenko, J. Olszewski, T. Martynkien, M. Łukomski, K. Gemza, P. Karasiński, M. Zięba, T. Baraniecki, Ł. Duda, A. Bachmatiuk, M. Guzik and R. Kudrawiec, *ACS Appl. Mater. Interfaces*, 2024, **16**, 28874–28885.
29 M. Cardona, in *Advances in Solid State Physics*, ed. O. Madelung, Pergamon, 1970, pp. 125–173.
30 R. Kudrawiec and W. Walukiewicz, *J. Appl. Phys.*, 2019, **126**, 141102.
31 J. Misiewicz and R. Kudrawiec, *Opto-Electron. Rev.*, 2012, **20**, 101–119.
32 J. Kopaczek, R. Bartoszewicz, K. Ciesiołkiewicz, A. P. Herman, V. Mazánek, I. Plutnarova, Z. Sofer and R. Kudrawiec, *ACS Appl. Electron. Mater.*, 2024, **6**, 7857–7864.
33 C. H. Ho, S. L. Lin and C. C. Wu, *Phys. Rev. B: Condens. Matter Mater. Phys.*, 2005, **72**, 125313.
34 Z. Li, Y. Lv, L. Ren, J. Li, L. Kong, Y. Zeng, Q. Tao, R. Wu, H. Ma, B. Zhao, D. Wang, W. Dang, K. Chen, L. Liao, X. Duan, X. Duan and Y. Liu, *Nat. Commun.*, 2020, **11**, 1151.
35 J. Kopaczek, M. K. Rajpalke, W. M. Linhart, T. S. Jones, M. J. Ashwin, R. Kudrawiec and T. D. Veal, *Appl. Phys. Lett.*, 2014, **105**, 112102.
36 R. Oliva, M. Laurien, F. Dybala, J. Kopaczek, Y. Qin, S. Tongay, O. Rubel and R. Kudrawiec, *npj 2D Mater. Appl.*, 2019, **3**, 1–8.

37 A. A. Mitioglu, P. Plochocka, Á. Granados del Aguila, P. C. M. Christianen, G. Deligeorgis, S. Anghel, L. Kulyuk and D. K. Maude, *Nano Lett.*, 2015, **15**, 4387–4392.
38 K. Posmyk, N. Zawadzka, M. Dyksik, A. Surrente, D. Maude, T. Kazimierczuk, A. Babiński, M. Molas, W. Paritmongkol, M. Maczka, W. Tisdale, P. Plochocka and M. Baranowski, *J. Phys. Chem. Lett.*, 2022, **13**, 4463–4469.
39 D. Pierścińska, *J. Phys. D: Appl. Phys.*, 2017, **51**, 013001.
40 A. M. Ślusarz, K. Komorowska, T. Baraniecki, S. J. Zelewski and R. Kudrawiec, *ACS Sustainable Chem. Eng.*, 2022, **10**, 8196–8205.
41 Anisotropic Thermal Conductivity of Crystalline Layered SnSe2 | Nano Letters, **https://pubs.acs.org/doi/10.1021/acs.nanolett.1c03018**, (accessed November 18, 2024).
42 J. Judek, A. P. Gertych, M. Świniarski, A. Łapińska, A. Dużyńska and M. Zdrojek, *Sci. Rep.*, 2015, **5**, 12422.
43 Temperature-Dependent Thermal Boundary Conductance of Monolayer MoS2 by Raman Thermometry | ACS Applied Materials & Interfaces, **https://pubs.acs.org/doi/10.1021/acsami.7b11641**, (accessed January 8, 2025).
44 J. Kopaczek, F. Dybała, S. J. Zelewski, N. Sokołowski, W. Żuraw, K. M. McNicholas, R. H. El-Jaroudi, R. C. White, S. R. Bank and R. Kudrawiec, *J. Phys. D: Appl. Phys.*, 2021, **55**, 015107.
45 F. Iikawa, A. A. Bernussi, A. G. Soares, F. O. Plentz, P. Motisuke and M. A. Sacilotti, *J. Appl. Phys.*, 1994, **75**, 3071–3074.
46 P. Vaiano, B. Carotenuto, M. Pisco, A. Ricciardi, G. Quero, M. Consales, A. Crescitelli, E. Esposito and A. Cusano, *Laser Photonics Rev.*, 2016, **10**, 922–961.
47 A. V. Stier, N. P. Wilson, G. Clark, X. Xu and S. A. Crooker, *Nano Lett.*, 2016, **16**, 7054–7060.
48 A. Castellanos-Gomez, M. Buscema, R. Molenaar, V. Singh, L. Janssen, H. S. J. van der Zant and G. A. Steele, *2D Mater.*, 2014, **1**, 011002.
49 F. Helmchen and W. Denk, *Nat. Methods*, 2005, **2**, 932–940.
50 L. Wawrezinieck, P.-F. Lenne, D. Marguet and H. Rigneault, in *Biophotonics Micro- and Nano-Imaging*, SPIE, 2004, vol. 5462, pp. 92–102.
51 J. Kopaczek, S. Zelewski, K. Yumigeta, R. Sailus, S. Tongay and R. Kudrawiec, *J. Phys. Chem. C*, 2022, **126**, 5665–5674.
52 L. Hu, X. Shan, Y. Wu, J. Zhao and X. Lu, *Sci. Rep.*, 2017, **7**, 15538.
53 K. Zelazna, M. Gladysiewicz, M. P. Polak, S. Almosni, A. Létoublon, C. Cornet, O. Durand, W. Walukiewicz and R. Kudrawiec, *Sci. Rep.*, 2017, **7**, 15703.
54 V. Karpus, B. Čechavičius, S. Tumėnas, S. Stanionytė, R. Butkute, M. Skapas and T. Paulauskas, *J. Phys. D: Appl. Phys.*, 2021, **54**, 504001.
55 M. Gladysiewicz, R. Kudrawiec, J. Misiewicz, G. Cywinski, M. Siekacz, P. Wolny and C. Skierbiszewski, *Appl. Phys. Lett.*, 2011, **98**, 231902.
56 H. Shen, Z. Hang, S. H. Pan, F. H. Pollak and J. M. Woodall, *Appl. Phys. Lett.*, 1988, **52**, 2058–2060.
57 D. E. Aspnes, *Surf. Sci.*, 1973, **37**, 418–442.
58 J. N. Hilfiker and T. Tiwald, in *Spectroscopic Ellipsometry for Photovoltaics: Volume 1: Fundamental Principles and Solar Cell Characterization*, ed. H. Fujiwara and R. W. Collins, Springer International Publishing, Cham, 2018, pp. 115–153.

Supporting information file for:

Thermotransmittance spectroscopy of layered crystals using lab on fiber

K. Ciesiołkiewicz[1]*, J. Kopaczek[1], R. Kudrawiec[1]

[1]*Department of Semiconductor Materials Engineering,*

Wroclaw University of Science and Technology,

Wybrzeże Wyspiańskiego 27, 50-370 Wrocław, Poland

* Corresponding author: *karolina.ciesiolkiewicz@pwr.edu.pl*

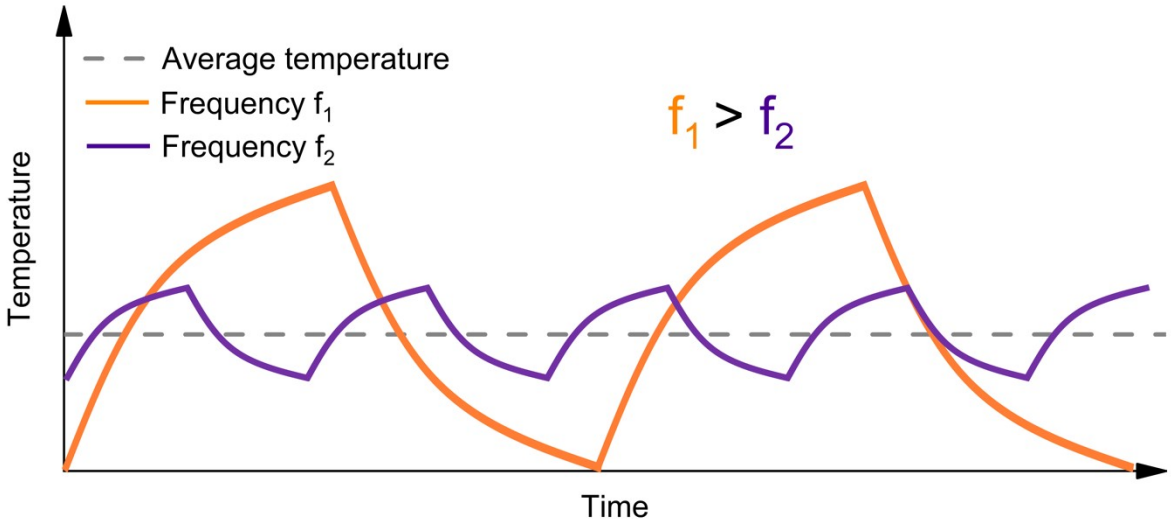

Figure S1. The diagram illustrates the temperature variations over time at two different frequencies. At lower frequencies, the fluctuations have a larger amplitude, leading to stronger resonance, while at higher frequencies, the amplitude decreases, resulting in weaker resonance. The average temperature stays consistent, maintaining the same energy position.

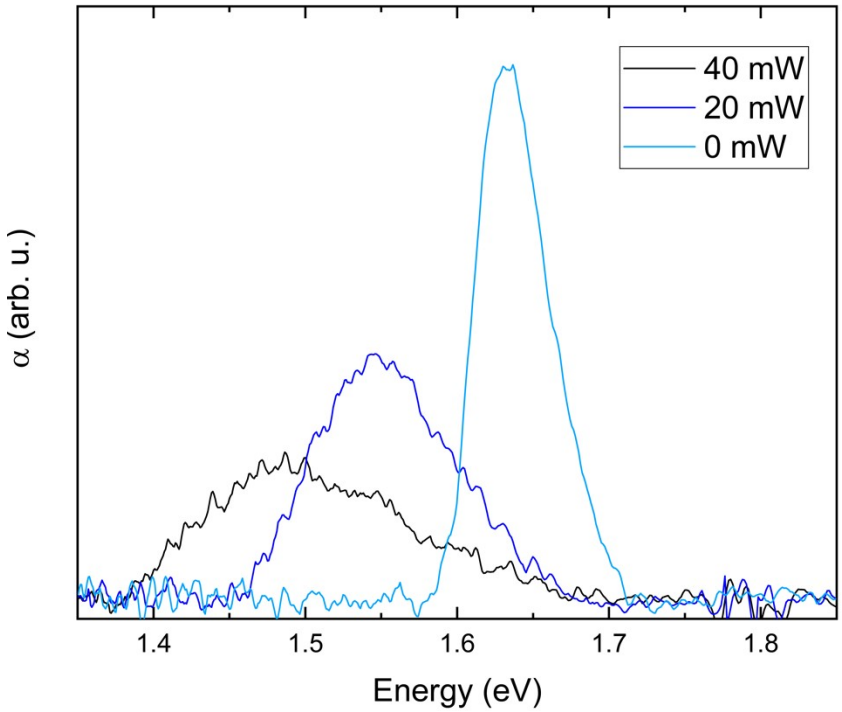

Figure S2. Variation of broadening in the WSe_2 sample with the change of laser power, at 0 mW, the linewidth is 84 meV, increasing to 107 meV at 10 mW, and further widening to 153 meV at 40 mW.

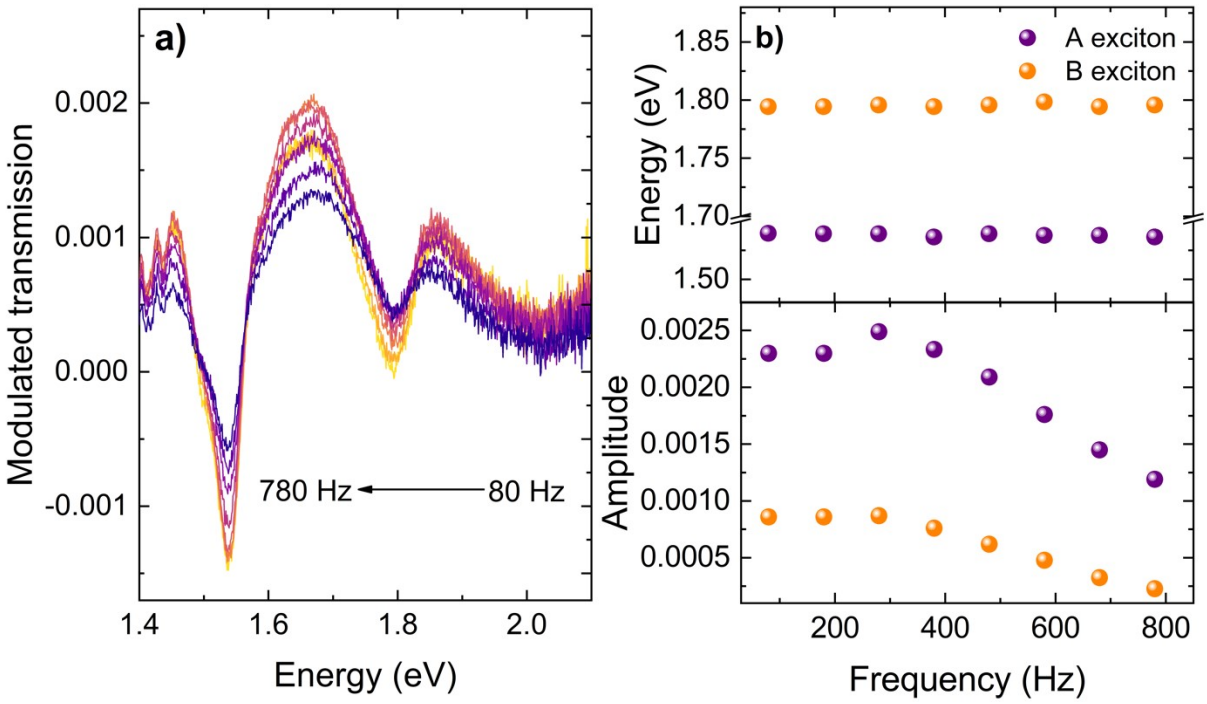

Figure S3. (a) Photoreflectance spectra of $MoSe_2$ obtained at different frequencies in the one-beam experiment, (b) present the results of the analysis for the spectra included in panel (a), i.e., energy and amplitude of optical transitions in the function of frequency.

Detailed Discussion on the Thermal Effects in the TMDC Samples

1. **Low Heat Capacity and Rapid Heating**

The thermal behavior of the TMDC sample is strongly influenced by its low heat capacity, given its small volume due to the thinness of the material and limited lateral size. The heat capacity (C) of the material can be described by:

$$C=c_p m=c_p \rho V$$

where c_p is the specific heat capacity, ρ is the material density, and V is the volume. Due to the extremely small volume of the TMDC layer, the energy required to raise its temperature is minimal. As a result, even small amounts of absorbed laser radiation can cause significant temperature fluctuations in the material. This relationship can be further understood by the equation:

$$Q=C\Delta T$$

where Q is the energy absorbed by the sample, and ΔT represents the temperature change. Since, as already mentioned, the TMDC layer has a low heat capacity, even a small amount of absorbed energy leads to a large temperature increase, resulting in rapid heating.

2. **Limited Thermal Conductivity and Heat Diffusion**

The other important factor is the limited thermal conductivity in TMDC materials, which significantly contributes to the thermal effects observed during the experiments. Heat conduction is described by Fourier's law:

$$q=-k\nabla T$$

where q is the heat flux, k is the thermal conductivity, and ∇T is the temperature gradient. In the case of TMDC materials, the thermal conductivity is much lower in the direction perpendicular to the plane compared to the direction parallel to the plane due to the weak van der Waals bonds between the layers. This affects the heat dissipation from the spot illuminated by the laser. The last factor that also plays a critical role in the thermal effect is the quality of the interface between the studied crystal and the fiber, which, together with the poor thermal conductivity of the fiber, leads to heat accumulation within the TMDC material.

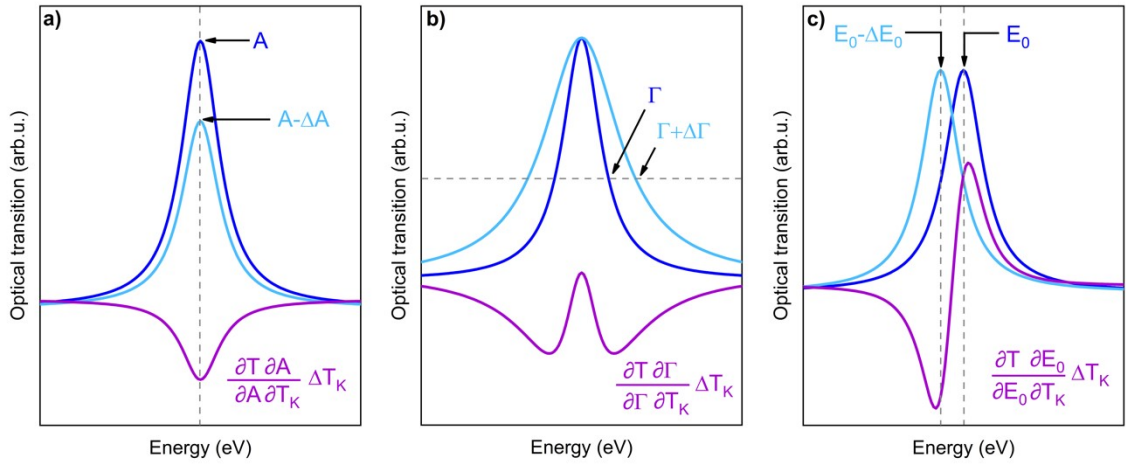

Figure S4. The impact of varying individual parameters of the Lorentzian function on the spectral shape related to temperature variation, along with their corresponding differential spectra (purple line). Results of: (a) a decrease in amplitude A, (b) an increase of broadening Γ, which progresses with temperature, and (c) a change in energy position, specifically, a redshift of the resonance energy E0.

In Fig. S4, we present the impact of varying individual parameters of the Lorentzian function o the spectral shape as a function of temperature, along with their corresponding differential spectra. This analysis helps to illustrate how each parameter contributes to the observed changes in the measured transmission spectra under varying thermal conditions. The first parameter, shown in Fig. 5a, is the amplitude A. As temperature increases, a gradual decrease in the amplitude of the optical transition (light blue line) is observed, resulting in a higher resonance intensity (purple line). This behavior is accompanied by the thermal broadening of the optical transitions and is attributed to a weakening of oscillator strength at elevated temperatures. The second parameter (Fig. 5b), which, as mentioned, is the broadening Γ, increases significantly with temperature. This broadening arises from enhanced phonon interactions and other scattering mechanisms at elevated temperatures, which effectively smear the resonance peak and reduce its sharpness. Finally, Fig. 5c illustrates the shift in the resonance energy E0 with temperature. In our measurements, this parameter exhibits a redshift as the temperature rises, corresponding to the temperature-dependent bandgap narrowing commonly observed in van der Waals crystals and other semiconducting materials.[1,2]

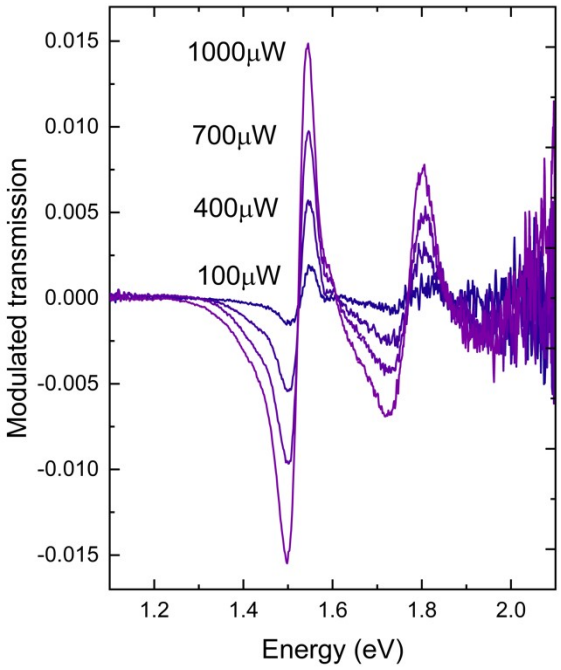

Figure S5. Modulated transmission spectra collected for the WSe_2 crystal at low laser power, showing that even at lower powers, the changes in transmitted light can be significant (e.g., ~3% for 100 μW and ~15% for 1000 μW).

References:

1 D. E. Aspnes, *Surface Science*, 1973, **37**, 418–442.

2 J. N. Hilfiker and T. Tiwald, in *Spectroscopic Ellipsometry for Photovoltaics: Volume 1: Fundamental Principles and Solar Cell Characterization*, eds. H. Fujiwara and R. W. Collins, Springer International Publishing, Cham, 2018, pp. 115–153.

2.3. Optical Fiber System for Precise Cryogenic Spectroscopy of 2D Materials

Citation:

Published in *ACS Applied Optical Materials, 2025*

DOI: 10.1021/acsaom.5c00220

Co-authors:

Karolina Ciesiołkiewicz-Klepek, Jan Kopaczek, Robert Kudrawiec

Author's contribution:

Karolina Ciesiołkiewicz-Klepek designed the optical setup and built the complete measurement system, conducted all measurements, including photoluminescence, transmission, photomodulated transmission, and photoreflectance, collected and analyzed the data, prepared the figures and graphical representations of the results, developed the interpretation of the results, wrote the manuscript, and served as the corresponding author.

Context within the dissertation:

This article presents an advanced fiber-based system tailored for low-temperature optical measurements of two-dimensional materials. It consolidates and applies the methods developed in earlier studies to perform comprehensive spectroscopic characterization at cryogenic temperatures. The work serves as a crucial experimental demonstration of the optical capabilities of lab-on-fiber platforms, particularly for probing excitonic phenomena in TMDC monolayers.

ACS APPLIED OPTICAL MATERIALS

pubs.acs.org/acsaom

Article

Optical Fiber System for Precise Cryogenic Spectroscopy of 2D Materials

Karolina Ciesiołkiewicz,* Jan Kopaczek, and Robert Kudrawiec

Cite This: https://doi.org/10.1021/acsaom.5c00220

Read Online

ACCESS | Metrics & More | Article Recommendations

ABSTRACT: An optical fiber-based system is presented for investigating the optical properties of layered van der Waals materials. This approach enables precise transmission, photoluminescence, photomodulated transmission, and photoreflectance measurements of monolayers and thin films, even at cryogenic temperatures. By placing the samples directly on the core of an optical fiber inside a cryostat, stable and reproducible measurements are achieved while minimizing thermal drift and mechanical vibrations. Using WSe_2 as a model system, excitonic transitions, trions, and interlayer excitons are observed. The results highlight the advantages of fiber-based spectroscopy in studying ultrathin materials, offering a versatile platform for exploring fundamental optical phenomena and band structure modifications in 2D materials.

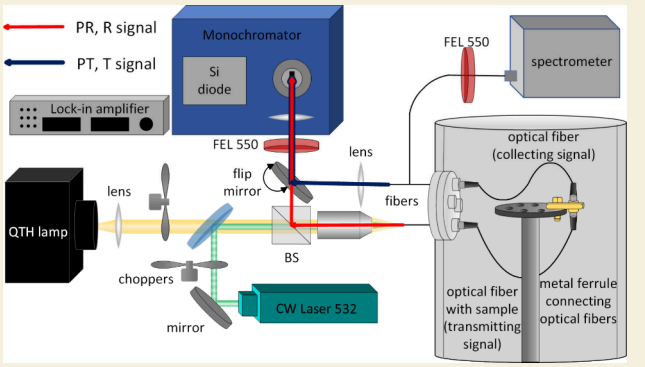

KEYWORDS: *modulation spectroscopy, TMDC crystals, mechanical exfoliation, temperature modulation, optical fiber*

1. INTRODUCTION

Semiconductors play a fundamental role in the technology of the modern world. We are surrounded by them-from smartphones and solar panels to advanced electronic devices.[1−3] Their unique properties, such as the ability to control the flow of electrical charges and absorb light, form the foundation of modern photonics and optoelectronics.[4−6] This enhances the need for progress in research on two-dimensional materials, which reveal increasingly complex mechanisms governing their optical and electronic properties.[7,8] Recently discovered two-dimensional materials, such as transition metal dichalcogenides (TMDs), represent a unique class of materials where reducing the thickness to a single atomic layer leads to fundamental changes in their electronic band structure.[9,10] Monolayers of these materials transition from an indirect to a direct bandgap, significantly influencing their optical properties, such as strong photoluminescence (PL) associated with excitonic transitions.[11,12]

Optical methods play a crucial role in the study of two-dimensional materials, providing insights into their electronic band structure, carrier dynamics, and the influence of the environment on their properties.[13] Transmission/reflectance methods are commonly used to determine absorption coefficients and analyze excitonic transitions.[14−16] Moreover, PL measurements enable the study of optical emission as a function of temperature, facilitating the identification of carrier localization processes, exciton−phonon interactions, and the effects of defects on emission.[17,18] Among different methods, modulated optical techniques, such as photomodulated transmission (PT) and photoreflectance (PR), offer even more advanced analyses.[19,20] These techniques involve optical modulation of the sample using an external light source, leading to changes in its optical properties, thus allowing the study of the electronic transitions across a broad spectral range and even their dynamics.[14] Optical transitions can also be modulated by an external electric field[13,14,21−24] but this requires appropriate electrical contacts[24] or placing the sample in a suitable capacitor.[23]

One of the fundamental challenges in optical studies of two-dimensional materials is conducting measurements at low temperatures, which reduce thermal effects and allow for a more precise examination of excitonic transitions and the influence of defects.[25,26] This, however, introduces technological challenges. Mechanical exfoliation is one of the most commonly used methods to obtain sufficiently thin samples, allowing for the isolation of monolayers from bulk crystals. In the initial stages of exfoliation, large fragments of material are

Received: June 13, 2025
Revised: August 11, 2025
Accepted: August 11, 2025

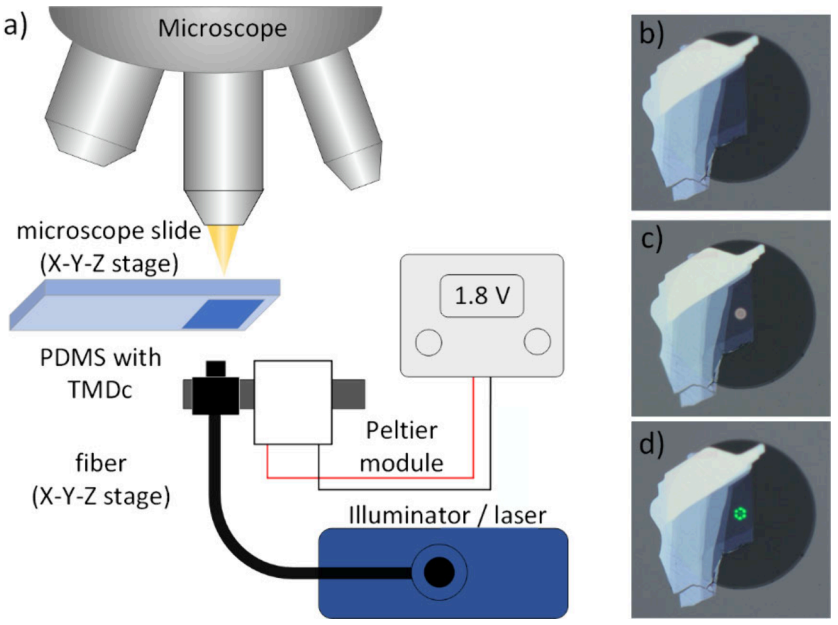

Figure 1. Microsetup to transfer TMDC on the flat tip of the fiber (a), fiber core with monolayer MoS_2 (b), with white light core illumination (c), and with laser core illumination (d).

obtained, but as the process progresses, flakes become smaller and thinner.[27,28] As mentioned, monolayer dimensions are often small, ranging from a few to several tens of micrometers, which significantly complicates precise measurements. For that reason, monolayers are more sensitive to vibrations, and accurate optical alignment becomes more challenging. In that case, the traditional cryogenic systems, although widely used in optical studies, introduce additional limitations. Cryostat pumps generate vibrations that can interfere with measurements, especially for small monolayers. Moreover, sample drift often occurs during long-term experiments, such as temperature-dependent measurements. This is a significant problem because obtaining consistent results requires studying the exact same fragment of the material, which may contain different densities of local defects affecting the signal. Traditional cryostats, while widely used in microscale measurements, require expensive vibration-reducing equipment or complex alignment systems, which consume a lot of cryogenic liquid and make the measurements very costly.

Currently, several studies report the use of fiber-based measurement systems, primarily for PL and transmission experiments under magnetic fields.[29−32] In those works, the main focus was placed on the properties of the studied materials rather than on the methodology or the measurement system itself, which was typically based on a continuous-flow cryostat. Moreover, there is a lack of studies employing fiber-based systems in which the material is placed directly on the fiber core to investigate how the transmission spectra evolve with thickness, starting from the bulk regime, where signal saturation occurs above the absorption edge. Finally, there is little to no information regarding the application of such systems in modulation spectroscopy techniques, which can reveal direct optical transitions with enhanced sensitivity.

In this work, we developed and described in details innovative measurement system that integrates optical techniques using an optical fiber core as a research platform coupled with the coldfinger of a helium cryostat operating in a closed cycle. The fiber enables stable placement of monolayers and thin layers of van der Waals materials onto its core, minimizing the impact of mechanical vibrations. The constructed system allows for easy integration with various spectroscopic methods. Here, we demonstrate transmission/reflection measurements, PL, and more advanced modulated optical techniques. Selected experiments were conducted over a wide temperature range, opening new possibilities in the optical study of 2D materials. The presented approach not only simplifies the measurement process of monolayer or thin crystals but also enables the study of more complex heterostructures, such as TMDs encapsulated with hBN layers or consisting of layers of different materials. An additional goal of our studies was to provide a detailed description of the system, as previously mentioned, to facilitate reproducibility by other researchers.

2. EXPERIMENTAL SETUP

The monolayers or thin films of the investigated materials were prepared by mechanical exfoliation and subsequently transferred onto the fiber tip under a microscope using PDMS (Figure 1). To ensure precise alignment of the sample with the fiber, a laser or white light was coupled into the fiber. This approach enabled accurate localization of the fiber core and verification of whether the material fully covered its surface. To enhance adhesion and minimize mechanical stress, the optical fiber was heated to approximately 60 °C during transfer using a Peltier module. An additional advantage of this configuration is the ability to observe photoluminescence on the camera when a laser is directed onto the sample from the fiber side, which can be useful for identifying monolayers.

The designed measurement system, shown in Figure 2, is multifunctional, adapting both transmission and reflection measurement configurations. Moreover, its modular configuration facilitates straightforward coupling with other experimental methods, such as PL. The easy replacement of detectors and light sources enables adaptation to various spectral ranges. Additionally, the system integrates light source modulation, which is essential for modulated transmission/reflection measurements and other advanced spectroscopic techniques. The main part of the setup consists of a standard cryostat working with a helium closed-cycle refrigerator. Such cryostat, typically employed in macroscopic measurements due to

https://doi.org/10.1021/acsaom.5c00220
ACS Appl. Opt. Mater. XXXX, XXX, XXX−XXX

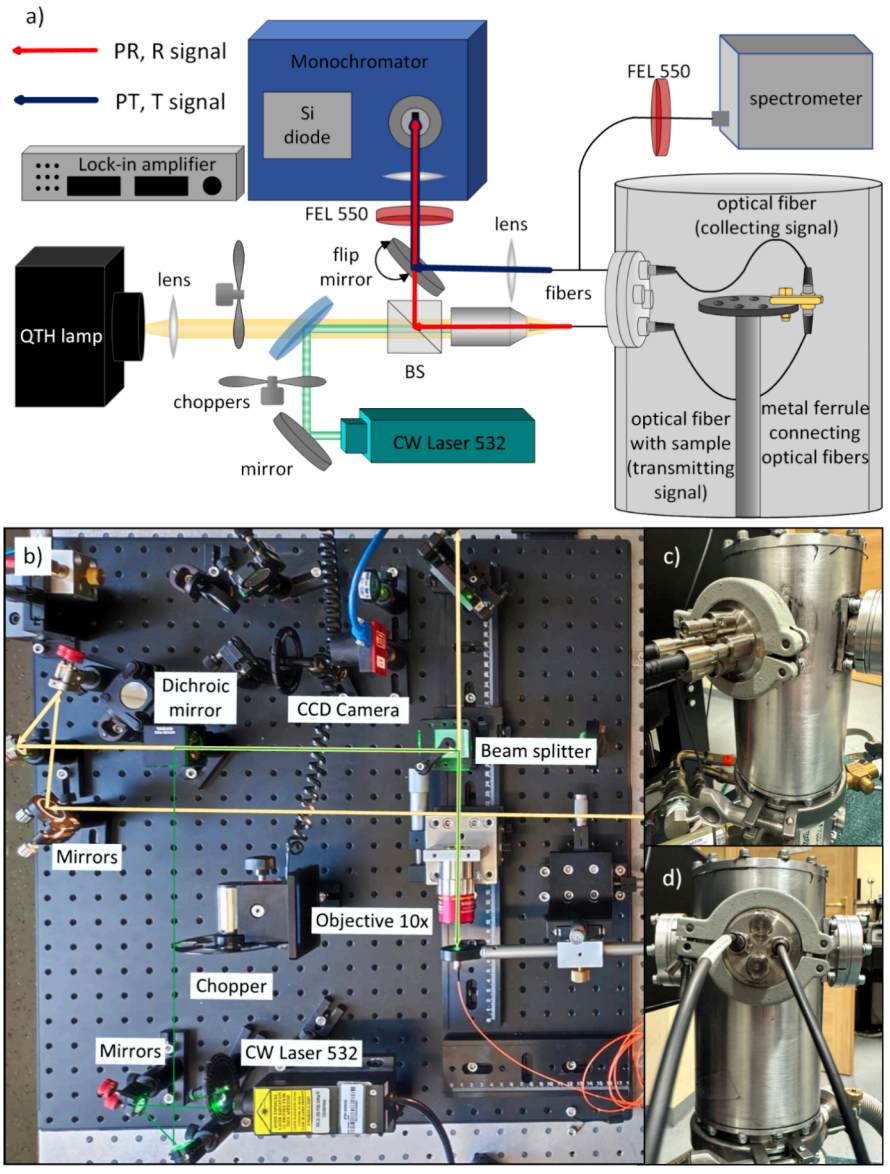

Figure 2. Schematic diagram of the experimental setup for measurements: red arrows indicate the signal pathway in the reflection configuration for photoreflectance, while dark blue arrows represent the transmission configuration for photomodulated transmission (a). Photograph of the experimental setup; yellow lines indicate the white light path, and green lines indicate the laser beam (b). Photographs of the vacuum shroud of the cryostat with fiber adapters, shown from different angles (c) and (d).

significant mechanical vibrations, has been adapted here for precise microscale measurements. This adaptation provides a cost-effective alternative to flow or closed-cycle cryostats with reduced vibrations. A key feature of this adaptation is the use of optical fibers, which optically connect the experimental setup with the cryostat and another fiber located within the cryostat with the studied sample placed on its core. The employment of fibers minimizes optical alignment issues and allows for efficient measurements under cryogenic conditions. All the optical fibers used in the system are interchangeable, further enhancing its flexibility.

The two main components of the measurement system are (1) the experimental setup adopted for selected spectroscopic techniques and (2) the previously mentioned low-temperature cryostat. The light coupling, one of the major parts of the experimental setup, is positioned on the optical table with light sources and beam modulation systems. Optical elements, including a objective lens, are used to introduce white light and laser beams into the fiber. Moreover, portable spectrometers and a monochromator with interchangeable detectors enable signal acquisition over a wide spectral range. Another central component is the cryostat, along with a compressor and cryogenic pump system that enable the attainment of low temperatures. The vacuum shroud of the cryostat is equipped with adapters that connect external fibers to internal ones, ensuring measurement stability. Inside the vacuum chamber, a fiber optic holder is mounted directly on the coldfinger. The holder comprises a metal tube designed to ensure optimal thermal contact with the coldfinger, facilitating efficient temperature transfer from fiber with the sample on it. It is crucial that the temperature sensor maintains direct contact with the holder to provide accurate measurements of the sample's temperature. Local heating of the sample at the fiber core, caused by excessive illumination, can easily occur due to the low thermal conductivity of the fiber. However, such heating is also readily detectable through the spectral shift in the emission or absorption.[33,34] To prevent this, all measurements were conducted at illumination intensities at least an order of magnitude lower than those for which such sample heating was observed.

As a probe beam, either for transmission or reflection measurement, a quartz tungsten halogen (QTH) lamp was employed, providing stable white light.[35] Furthermore, a continuous wave (CW) laser with a wavelength of 532 nm was used as a pump beam in

https://doi.org/10.1021/acsaom.5c00220
ACS Appl. Opt. Mater. XXXX, XXX, XXX−XXX

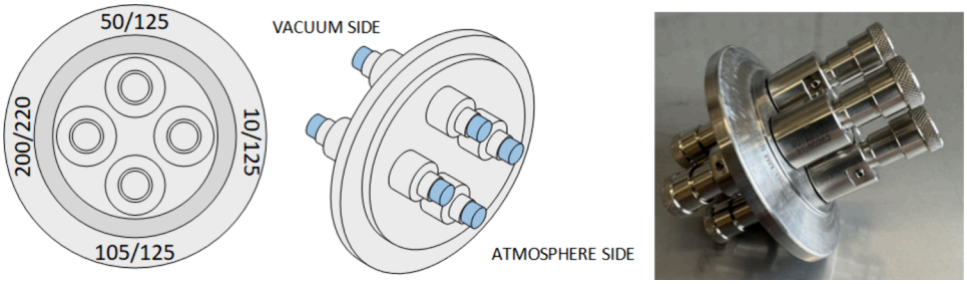

Figure 3. Schematics and photograph of a vacuum shroud window equipped with optical fiber adapters. The cryostat insert connects the outer atmospheric part of the measurement system to the vacuum section. The four adapters are compatible with optical fibers featuring the following specifications: a 10 μm core with a 125 μm cladding, a 50 μm core with a 125 μm cladding, a 105 μm core with a 125 μm cladding, and a 200 μm core with a 220 μm cladding.

modulation experiments or as an excitation source in PL measurements. Both sources are combined using a dichroic mirror and then focused into the fiber input via an objective lens. During most measurements, the light was introduced through an external input fiber with a 50 μm core. The external fiber was then connected to the internal one (inside the cryostat) by an adapter located in the cryostat window. The first internal fiber held the sample directly on its core. If a reflection signal was being collected, it returned along the same path and was directed to the monochromator via a beam splitter (BS). In transmission mode, the signal was collected by a second internal fiber with a 105 μm core, which effectively captured the divergent light cone transmitted through the sample. The adapter then connected the internal fiber to the second of the external ones, directing the signal to either the spectrometer or monochromator. A flip mirror allowed for the selection of whether the monochromator received the reflection or transmission signal.

In PR and PT measurements, which are differential techniques, the laser beam was modulated using a chopper. At the same time, the sample was illuminated by a white beam detecting any changes evoked by the laser in a reflected/transmitted light. Subsequently, the signal collected by the fiber was directed to the monochromator for spectral analysis and recorded using the lock-in technique. The mentioned changes in the reflected/transmitted light correspond to optical transition. For PL or standard transmission measurements, the signal could alternatively be analyzed using a portable spectrometer. Depending on the measurement type, a long pass 550 nm filter was positioned in front of the appropriate detector to suppress spectral components originating from the laser.

Custom multimode (MM) optical fibers from Thorlabs (model FG010LDA Low-Autofluorescence Custom Patch Cord) with unique properties were employed to significantly enhance measurement accuracy. These fibers were designed to minimize autofluorescence (by photobleaching), which could interfere with PL signals. Furthermore, the employed fibers are more resistant to degradation under intense light exposure, ensuring signal stability during prolonged measurements. The spectral range of the fibers spans from 400 to 2400 nm, enabling the study of a wide variety of materials. Additionally, one of the windows in the vacuum shroud was replaced with a specially designed insert with fiber optic adapters, ensuring the vacuum integrity of the cryostat. Additionally, having four adapters allows for various experimental configurations, as described earlier. The insert, as illustrated in Figure 3, was equipped with four adapters dedicated to MM optical fibers with core diameters of 10, 50, 105, and 200 μm. The sample was directly deposited on the polished end of the optical fiber, which served as both the carrier and the optical element in the measurement system.

The described system enables the investigation of a wide range of materials, including thin films and monolayers, focusing on their optical and PL properties. With innovations such as reduced autofluorescence fibers and the adaptation of the cryostat for microscale measurements, the system represents a significant advancement in precise optical measurements under cryogenic conditions. Furthermore, in the design setup, the measurement zone was decoupled from the rest of the experimental setup. The most important aspect of the proposed system is its ability to utilize an optical system with a standard cryogenic refrigerator, where the coldfinger vibrates, thereby preventing measurements with micrometer spatial resolution. The cost of adopting such a system includes the purchase of appropriate optical fibers, connectors, and other optical components, the total cost of which is less than $1,000.

3. RESULTS AND DISCUSSION

3.1. Studies of the Emission Properties: Photoluminescence Measurements

Here, we demonstrate the application of a low-temperature cryostat equipped with optical fibers, where a fiber with a monolayer transferred on its core is in thermal contact with the coldfinger. In this configuration, the external fibers (on the ambient side) connected to the adapter (Figure 3) enable PL measurements, i.e., the experimental setup is configured for PL studies. A CW laser at 532 nm serves as the excitation source, introduced into the system through one of the optical fibers. The emitted PL is then collected by a separate fiber and directed to a spectrometer for spectral analysis. This dual-fiber approach minimizes optical losses and ensures efficient signal collection while maintaining stable cryogenic conditions, enabling precise temperature-dependent PL measurements.

All the measurements included in this and later sections were performed on WSe_2, a TMD material. The choice of this material was dictated by the fact that it is a well-known and extensively studied semiconductor. This allowed us to focus strictly on the novel methodology proposed in this work to study optical properties and to evaluate whether the obtained results are as detailed as those from conventional approaches. The PL spectra were collected as a function of temperature, from 20 to 320 K (Figure 4a). In this case, the area of the flake that covers the core of the optical fiber is excited, and PL is collected from this area. In the low-temperature range, two peaks are visible in the spectra: one corresponding to the exciton (X_0), which is observed across the entire temperature range, and the other corresponding to the trion (T), detectable up to 100 K. At 20 K, the position of the trion and excitonic transition are approximately 1.704 and 1.737 eV, respectively, which is in good agreement with previous work.[26,36,37] The overall temperature dependence of the exciton and trion energy positions, shown in Figure 4b, reveals a decrease in energy with increasing temperature, where the energy shift of neutral exciton is around 70 meV from low to room temperature. Moreover, the emission intensity of the exciton is consistently stronger than that of the trion. Additionally, it is important to note that at low temperatures, PL spectra are free

https://doi.org/10.1021/acsaom.5c00220
ACS Appl. Opt. Mater. XXXX, XXX, XXX−XXX

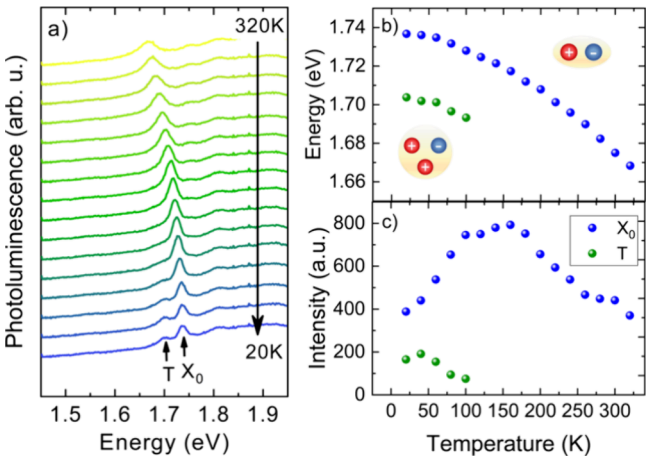

Figure 4. PL spectra of WSe_2 monolayer measured as a function of temperature. The spectra reveal the presence of two distinct peaks corresponding to the X_0 neutral exciton and T trion (a). Temperature dependence of their energy positions (b), and temperature dependence of the PL intensity (c).

from defect-related (trapped exciton) recombination, which indicates that the studied monolayer is of good quality.

The observed intensity of the exciton emission (Figure 4c) exhibits a nonmonotonic behavior: first, it increases up to 100 K, remains relatively stable until 180 K, and then begins to decrease. This behavior reflects the interplay of several factors influencing the recombination dynamics in 2D materials. At low temperatures, excitons and excess charge carriers tend to thermalize at specific sites, which promotes trion formation and enhances their emission relative to excitons. However, as the temperature increases, trions may dissociate into excitons and free carriers, leading to a gradual reduction in trion intensity and a more prominent exciton emission. Furthermore, since the excitonic ground state in W-based TMD materials is dark, an increase in temperature can populate a higher-energy bright state, resulting in increased emission.[38−40] The observed drop in intensity beyond 180 K may be attributed to a stronger contribution of nonradiative recombination processes. When comparing these results with those from the literature, it is also important to remember that the WSe_2 flake is not coated with an hBN layer, which typically improves optical properties by narrowing the line width and reducing nonradiative recombination.[41,42]

The results described above demonstrate the viability of the proposed configuration, where PL spectra are collected using a set of optical fibers. This approach eliminates the need for systems with reduced vibration and drift, as the studied monolayer is located directly on the core of the optical fiber, through which the excitation laser is simultaneously delivered. Additionally, the use of optical fibers decouples the experimental setup from the measurement zone, i.e., the location of the sample from a detector, which in this case is a portable spectrometer. Lastly, and most importantly, the obtained results were as detailed as those from a typical experimental setup dedicated to micro-PL studies.

3.2. Optical Absorption Determination: Transmission Measurements

In transmission measurements, the system utilizes a broadband QTH lamp as the probe beam, ensuring stable illumination. The incident light is coupled into an external optical fiber and

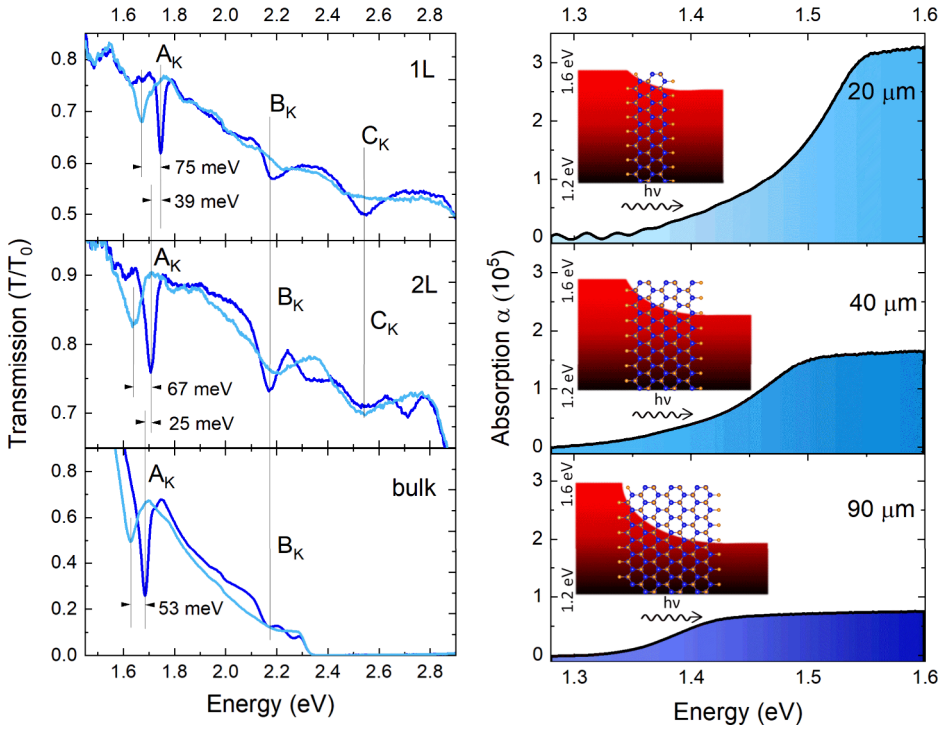

Figure 5. Evolution of the transmission spectrum of WSe_2 as a function of sample thickness, from bulk material to bilayer (2L) and monolayer (1L), left panel. For each sample, the dark blue line represents the spectrum measured at 20 K, while the light blue line corresponds to the spectrum measured at room temperature (RT). The right panel shows how the absorption spectrum changes with sample thickness for samples of 20, 40, and 90 μm, respectively. The spectral range in which light is transmitted through the sample varies with thickness. T_0 is the light transmission through the system without a flake on the fiber.

https://doi.org/10.1021/acsaom.5c00220
ACS Appl. Opt. Mater. XXXX, XXX, XXX−XXX

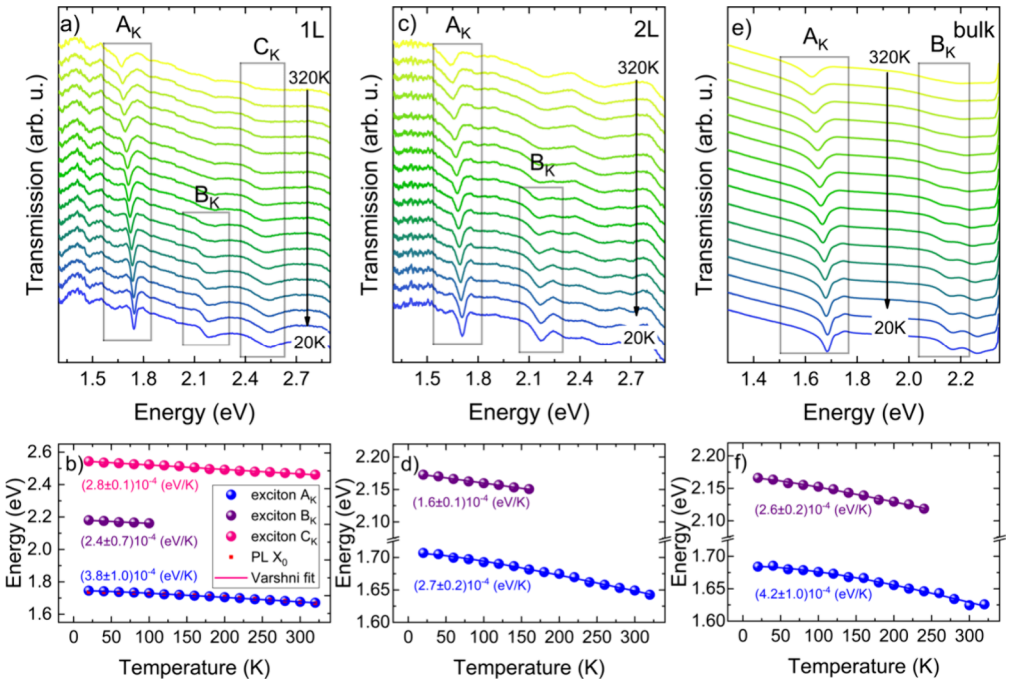

Figure 6. Temperature-dependent transmission spectra for monolayer (1L) (a), bilayer (2L) (c), and bulk (e) WSe_2, along with the corresponding exciton energy positions as a function of temperature (b, d, f).

directed onto the monolayer sample positioned on the fiber core inside the cryostat. A second internal fiber collects the transmitted light, which is then analyzed using either a spectrometer or a monochromator. This fiber-integrated setup ensures efficient light collection while maintaining stable cryogenic conditions, enabling precise studies of absorption features and optical transitions in van der Waals materials.

According to the Beer−Lambert law, the intensity of light transmitted through a material depends on the initial intensity (before passing through the material) and the thickness of the sample.[43] Therefore, preparing samples for such measurements often involves thinning them to maximize the observable spectral range. For indirect bandgap measurements, a thickness of tens of micrometers is typically sufficient. The relationship between sample thickness and the transmission spectrum is experimentally illustrated in Figure 5. However, to measure direct transitions in the semiconducting materials, the sample thickness, depending on the absorption coefficient, must not exceed hundreds of nanometers. This poses challenges in sample preparation and in focusing light to ensure it fully passes through the sample area.

To overcome these challenges, we propose a solution where a thin layer, bilayer, and monolayer of WSe_2 were deposited onto an optical fiber with a 10 μm core, which was then placed in a cryostat in direct contact with a coldfinger. Moreover, this setup allowed us to measure such thin and small samples even at low temperatures. The results of transmission experiments conducted at 20 K for samples of different thicknesses are shown in Figure 5. The positions of excitons A, B, and C shift with layer thickness, with each optical transition observed at the highest energy for the monolayer compared to samples of other thicknesses.[44] For example, the position of exciton A is 1.747 eV for the monolayer, 1.706 eV for the bilayer, and 1.686 eV for the bulk (a similar trend is observed at room temperature, Figure 6). Exciton B shifts from 2.185 eV in the monolayer to 2.167 eV in the bilayer at 20 K, while exciton C shifts from 2.544 to 2.529 eV. This observed redshift is associated with changes in the band structure as the number of layers increases.[45−47] In monolayer WSe_2, the material exhibits a direct bandgap at the K-point of the Brillouin zone, where electrons in the conduction band and holes in the valence band are located at the same momentum point. Moreover, the monolayer has the largest bandgap among all structures due to the absence of interlayer interactions, which allows for stronger quantum confinement. In bilayer WSe_2, the band structure begins to exhibit characteristics of an indirect bandgap. The transition from a direct bandgap in monolayers to an indirect bandgap in bulk is a key structural change driven by interlayer interactions, which modify the distribution of electronic states.[48]

Temperature-dependent changes in transmission spectra are presented in Figure 6, with measurements performed for the monolayer, bilayer, and bulk. For all samples, a blueshift of exciton energies is observed as the temperature decreases, which is consistent with the typical temperature dependence of the bandgap in semiconductors including WSe_2.[37,49] In the case of the monolayer, Figure 6b also includes energy positions obtained from PL measurements. These positions align well with the exciton A energy observed in transmission measurements, indicating that the same excitonic transitions are being probed in both experimental techniques. This alignment highlights the direct bandgap nature of the monolayer, where excitons dominate both absorption and emission processes. The blueshift observed in the bilayer, and bulk samples follow a similar trend with the decrease in temperature. Additionally, as discussed earlier, increasing the number of layers causes the excitonic features to shift to lower energies due to interlayer interactions that modify the band structure. Despite this, the temperature dependence of the excitonic transitions remains evident, underscoring the intrinsic properties of the material across different thicknesses.

https://doi.org/10.1021/acsaom.5c00220
ACS Appl. Opt. Mater. XXXX, XXX, XXX−XXX

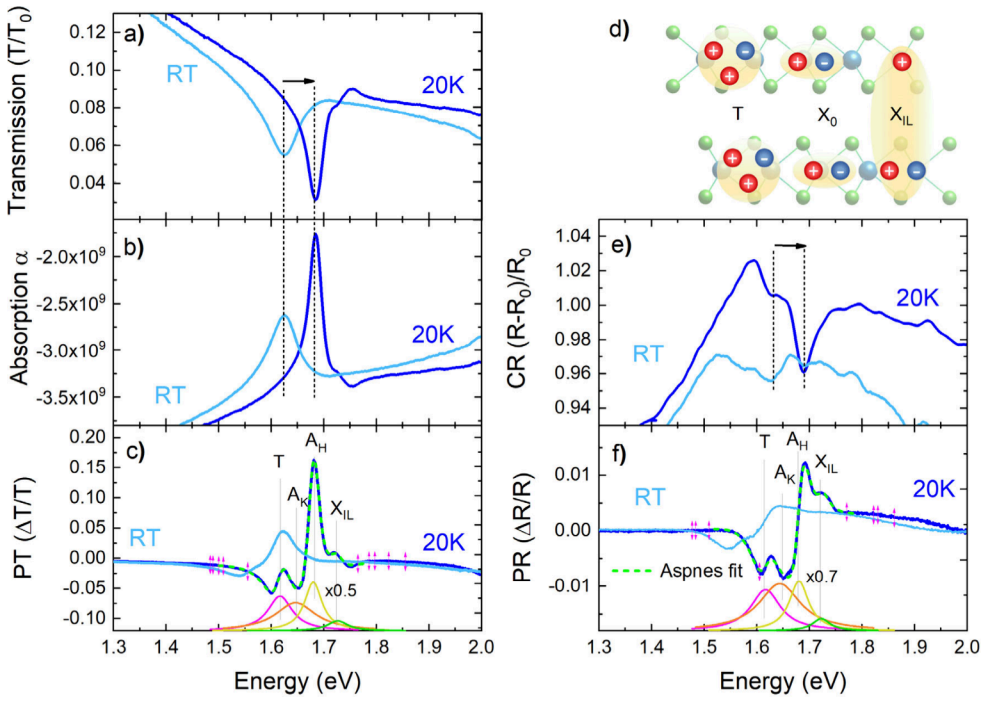

Figure 7. A summary of the results obtained using different measurement techniques: transmission (a), the resulting absorption (b), and photomodulated transmission (c). The observed trion, exciton, and interlayer exciton in WSe_2 are schematically illustrated on a bilayer crystal (d). Additionally, contrast reflectance (e) and PR (f) are shown. The signal noise level in PT/PR was on the order of 10^{-4}. All techniques consistently confirmed the position of the A_K transition at room temperature and 20 K, while PT and PR further revealed the presence of the trion and interlayer exciton at 20 K. Absorption spectra were determined from transmission spectra.[59] T_0/R_0 is the light transmission/reflection through/from the system without a flake on the fiber.

The temperature dependencies in Figure 6 were analyzed using the Varshni model, given by the equation

$$E_0(T) = E_0(0) - \frac{\alpha T^2}{\beta + T}$$

where $E_0(0)$ represents the bandgap or optical transition energy at 0 K, while the parameters α and β correspond, respectively, to the energy shift per kelvin related to electron–phonon coupling and the characteristic phonon temperature.[50] The fits presented in Figure 6 indicate that the values of α are lower in the monolayer, which aligns with the general trend observed for TMDs: exciton transitions in 2D layers exhibit less temperature sensitivity compared to the bulk material. Moreover, the significantly higher α value for transition A_K in the bulk compared to the monolayer suggests stronger electron–phonon coupling. These results confirm that the transition from bulk to monolayer not only shifts the energy band positions but also affects phonon interactions.[37]

The experimental setup, which involved transferring the studied material onto an optical fiber with a 10 μm core, enabled precise measurements of transmission for such thin samples, including monolayers. This approach ensured that the light fully interacted with the sample while minimizing scattering and maximizing the collected signal. The inclusion of a cryostat allowed for accurate control of the temperature over a broad range, from cryogenic conditions to room temperature, facilitating a detailed investigation of the temperature-dependent optical properties of WSe_2.

3.3. Determination of Optical Transitions: Modulation Spectroscopy (Photomodulated Transmission and Photoreflectance)

The measurements described in this section were performed using a spectroscopic setup that included a monochromator and a detection system based on a lock-in amplifier, where the chopping frequency of a laser beam determined the reference signal. A CW laser at 532 nm was used to induce periodic perturbations of the internal parameter, which was a built-in electric field, while the probe beam (white light) was simultaneously introduced to monitor changes in the reflected (PR) or transmitted (PT) signal. The collected modulated signal was then directed to the monochromator and analyzed using a lock-in technique, allowing for enhanced signal detection and noise suppression. This configuration is particularly suited for detecting subtle changes ($\Delta R/R$ ($\Delta T/T$) $\sim 10^{-5}$–10^{-6}) in reflection or transmission signal related to optical transitions, making it a powerful tool for studying excitonic and band-structure modifications in 2D materials.[14,19,33,51] Furthermore, modulation spectroscopy, which is the primary research method in our laboratory, provides additional insights into the studied materials, particularly in the context of various optical transitions that are not always easily identified using other spectroscopic techniques. This method is primarily sensitive to direct optical transitions, allowing for the identification of so-called resonance features in modulation spectra associated with band-to-band transitions related to, e.g., direct bandgap or excitonic complexes. Most importantly, modulation spectroscopy allows for precise (spectrally resolved) and direct observation of these transitions, which is particularly evident in low-temperature PR and PT measurements. This is due to the differential-like character of these

https://doi.org/10.1021/acsaom.5c00220
ACS Appl. Opt. Mater. XXXX, XXX, XXX−XXX

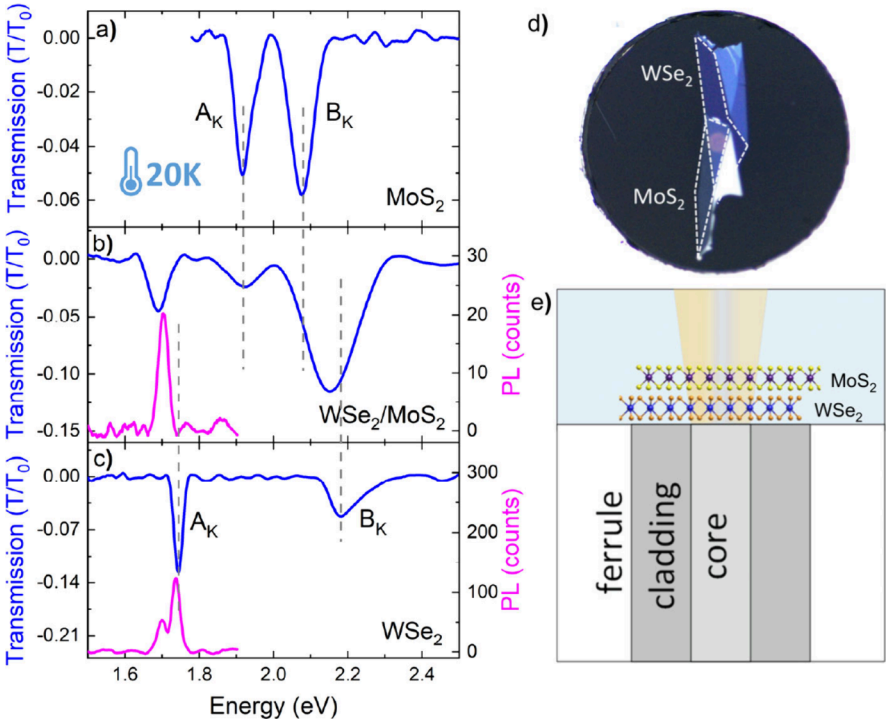

Figure 8. Low-temperature transmission (T, dark blue line) and photoluminescence (PL, pink line) spectra of (a) a monolayer MoS_2, (b) a WSe_2/MoS_2 heterostructure, and (c) a monolayer WSe_2, demonstrating the optical response of these materials. (d) Top-view microscopic image of the flat tip of an optical fiber, where a WSe_2 monolayer is positioned at the bottom, covering the fiber core (10 μm in diameter), while a MoS_2 monolayer is placed on top, also covering the core. (e) A schematic representation of the multimode optical fiber, illustrating the placement of exfoliated crystals used in the experiment.

techniques and, consequently, the lack of background signal.[52,53]

For very thin samples, such as those used in our study, transmission-mode measurements prove to be more effective than reflection-mode measurements in terms of the signal strength corresponding to optical transitions. This is because, in thin samples, the transmitted signal is determined by absorption through the entire crystal, whereas in reflection, the signal is influenced primarily by the surface and is also affected by a phase shift. As a result, transitions in transmission measurements are more pronounced, enabling better spectral separation of these resonances/optical features. In thicker samples (bulk crystals), transmission mode cannot be effectively used because the light, after passing through the material, is reduced to a nonmeasurable level. At the same time, the reflection signal can be weaker (due to the reasons described above), making the separation of transitions less clear. For these reasons, when comparing our results with data obtained from thicker samples presented in the works of refs 49 and 22, where a reflection configuration was applied, we observed a clearer separation of neutral exciton and trion for thin-film samples, Figure 7c (PT) and 7f (PR). Additionally, in this case, we also observe interlayer exciton (X_{IL}).[54−57] Moreover, all the results obtained here are, to some extent, consistent when comparing transmission, absorption, and contrast reflection measurements, as shown in Figure 7a, 7b, and 7e, respectively. However, in these results, not all optical transitions are as easily distinguishable as in the case of modulation measurements (Figure 7c and 7f). The use of modulation spectroscopy in conjunction with thin-film samples allows for more precise results, particularly in studying optical transitions in two-dimensional materials such as WSe_2. These results are crucial for understanding the mechanisms responsible for optical transitions and can contribute to the further development of measurement techniques that enable more accurate investigations of the electronic structures of these materials.

Figure 7 presents a detailed comparison of various spectroscopic techniques, providing comprehensive results from our investigations. The left panels illustrate the transmission, absorption, and PT spectra recorded at room temperature and 20 K, while panels (e) and (f) display the contrast reflectance (CR) and PR spectra under the same temperature conditions. Across all these methods, the observed optical transitions consistently occur at the same energies, with a clear trend of shifting toward higher energies as the temperature decreases. The Aspnes formula was fitted to the PT results in panel (c) and PR spectra in panel (f) to extract energy and broadening of optical transitions:

$$\frac{\Delta T}{T}(E) = Re[Ae^{i\theta}(E - E_0 + i\Gamma)^{-m}]$$

where θ is the phase factor, while m is related to the type of optical transition; for excitonic transitions, it is equal to 2.[58] Moreover, A, E, and Γ represent the amplitude, energy, and broadening of optical transitions, respectively.

This behavior, i.e., the temperature-induced energy shift, reflects the fundamental temperature dependence of the electronic band structure and the associated optical transitions. Moreover, due to an increased phonon population at higher temperatures, the optical transitions become weaker and broader, making them less spectrally distinguishable. Despite the agreement in transition energies, each technique exhibits unique characteristics that make it particularly advantageous

https://doi.org/10.1021/acsaom.5c00220
ACS Appl. Opt. Mater. XXXX, XXX, XXX−XXX

for specific experimental contexts. For instance, PT offers enhanced sensitivity to subtle optical features, while contrast reflectance provides a straightforward and quick method for identifying transitions in materials with high reflectivity. Similarly to PT, PR excels at spectrally separating transitions by leveraging its modulation nature, which, in this case, is the modulation of the built-in electric field. As a result, the obtained PR and PT spectra have a differential character with so-called resonances corresponding to optical transitions. These complementary strengths underscore the importance of having a versatile experimental setup capable of accommodating multiple measurement techniques.

In general, our system has been specifically designed to support a wide range of spectroscopic techniques, ensuring the flexibility needed to tailor experiments to the specific properties of the materials under investigation. This adaptability not only enhances the reliability of our results but also allows for a more comprehensive characterization of the materials, enabling us to capture a complete picture of their optical and electronic properties under varying experimental conditions. Such versatility is essential for advancing our understanding of complex materials and optimizing their potential for various technological applications.

3.4. Fabrication of Heterostructures on a Fiber Tip

To demonstrate the versatility of the approach presented in this work for optical studies of layered materials, we also prepared a WSe_2/MoS_2 heterostructure directly on the optical fiber tip using the same transfer technique as before (Figure 8d,e). Transmission measurements at 20 K reveal that the heterostructure exhibits a superposition of excitonic transitions from both WSe_2 and MoS_2, with increased broadening of A exciton in the constituent monolayers, indicating strong interlayer coupling (Figure 8a-c).[60,61] Notably, the A excitonic transition of WSe_2 undergoes a significant redshift compared to its monolayer form, while the MoS_2 excitonic transitions remain nearly unchanged. Additionally, the excitonic peaks in the heterostructure, observed through transmission and PL measurements, are broader than those in the individual monolayers. Furthermore, the B exciton transitions of both WSe_2 and MoS_2 merge in the heterostructure, forming a single broadened peak at approximately 2.08 eV. Moreover, as previously mentioned, the A exciton of WSe_2 shifts from 1.745 eV in the monolayer to 1.683 eV in the heterostructure, while the A exciton of MoS_2 remains nearly unchanged at approximately 1.923 eV. The redshift in transmission for WSe_2 in the heterostructure is primarily due to the change in the dielectric environment. This is because the experimental system consisted of an optical fiber core, on which WSe_2 was placed, followed by MoS_2, and finally, vacuum/air. As a result, WSe_2 in the heterostructure experienced a significant change in its surrounding dielectric constant, leading to the observed energy shift. In contrast, the change in the dielectric environment had a much weaker effect on MoS_2 because the dielectric constants of the fiber core and WSe_2 are more similar to each other compared to the difference between the dielectric constants of MoS_2 and vacuum/air when WSe_2 on the fiber is considered either as an individual monolayer or as part of the heterostructure.[61] Such an approach, using an optical fiber as a platform for heterostructure assembly and PL measurements, has been demonstrated in the literature for WSe_2 encapsulated in hBN.[29−32]

4. CONCLUSIONS

We present, a comprehensive optical fiber-based system dedicated to investigating and characterizing layered van der Waals materials, such as dichalcogenides, trichalcogenides, or monochalcogenides. This system offers a cost-effective and versatile solution, leveraging conventional optical techniques while enabling precise measurements of thin layers and monolayers, even at cryogenic temperatures. Here, the studied samples are placed directly on the flat end of an optical fiber, which is in contact with a coldfinger inside a cryostat operating in a helium closed-cycle refrigerator. Such a setup minimizes common challenges, including thermal drift and mechanical vibrations. The use of a fiber-to-fiber adapter, which directly couples the light-delivering fiber with the signal-collecting fiber, ensures stable alignment and eliminates signal fluctuations caused by external disturbances. The fiber-to-fiber adapters are integrated into an element placed within the vacuum shroud, in the position typically used for optical windows. Additionally, sample preparation and transfer onto the optical fiber are straightforward, and the prepared crystals adhere well to the fiber surface, ensuring stable and reproducible measurements.

Using this approach, we successfully performed photoluminescence, transmission, photomodulated transmission, and photoreflectance measurements. In each case, experiments were conducted at both room temperature and low temperatures around 20 K. The high sensitivity of the system allowed us to clearly resolve the most common excitonic optical transitions in layered materials. In WSe_2, used as a well-known example of TMD crystals, we identified direct A, B, and C excitonic transitions, observed the presence of not only excitons but trions, and detected an interlayer k-exciton in a thin sample. The results demonstrate that even extremely thin samples can be effectively studied with this setup, highlighting its capability for exploring excitonic phenomena and band structure modifications in two-dimensional materials.

AUTHOR INFORMATION

Corresponding Author

Karolina Ciesiołkiewicz − *Department of Semiconductor Materials Engineering, Wroclaw University of Science and Technology, 50-370 Wrocław, Poland;* orcid.org/0000-0003-0898-8095; Email: karolina.ciesiolkiewicz@pwr.edu.pl

Authors

Jan Kopaczek − *Department of Semiconductor Materials Engineering, Wroclaw University of Science and Technology, 50-370 Wrocław, Poland;* orcid.org/0000-0003-4851-9568

Robert Kudrawiec − *Department of Semiconductor Materials Engineering, Wroclaw University of Science and Technology, 50-370 Wrocław, Poland;* orcid.org/0000-0003-2593-9172

Complete contact information is available at: https://pubs.acs.org/10.1021/acsaom.5c00220

Notes

The authors declare no competing financial interest.

https://doi.org/10.1021/acsaom.5c00220
ACS Appl. Opt. Mater. XXXX, XXX, XXX−XXX

■ ACKNOWLEDGMENTS

This work was supported by the National Science Centre (NCN) Poland OPUS 23 no. 2022/45/B/ST7/02750.

■ REFERENCES

(1) Pan, Y.; Yang, B. Comprehensive Analysis of Advancements and Challenges in Smartphone Semiconductor Technology. *Highlights in Science, Engineering and Technology* **2024**, *87*, 214−218.
(2) Martí, A.; López, N.; Antolín, E.; Cánovas, E.; Stanley, C.; Farmer, C.; Cuadra, L.; Luque, A. Novel Semiconductor Solar Cell Structures: The Quantum Dot Intermediate Band Solar Cell. *Thin Solid Films* **2006**, *511−512*, 638−644.
(3) Lee, J. Y.; Shin, J.-H.; Lee, G.-H.; Lee, C.-H. Two-Dimensional Semiconductor Optoelectronics Based on van Der Waals Heterostructures. *Nanomaterials* **2016**, *6* (11), 193.
(4) Shanmugam, V.; Mensah, R. A.; Babu, K.; Gawusu, S.; Chanda, A.; Tu, Y.; Neisiany, R. E.; Försth, M.; Sas, G.; Das, O. A Review of the Synthesis, Properties, and Applications of 2D Materials. *Particle & Particle Systems Characterization* **2022**, *39* (6), 2200031.
(5) Jin, L.; Wang, H.; Cao, R.; Khan, K.; Tareen, A. K.; Wageh, S.; Al-Ghamdi, A. A.; Li, S.; Li, D.; Zhang, Y.; Zhang, H. The Rise of 2D Materials/Ferroelectrics for next Generation Photonics and Optoelectronics Devices. *APL Materials* **2022**, *10*, 060903.
(6) Salehi, S.; Saffarzadeh, A. Optoelectronic Properties of Defective MoS2 and WS2Monolayers. *J. Phys. Chem. Solids* **2018**, *121*, 172−176.
(7) Dutta, T.; Yadav, N.; Wu, Y.; Cheng, G. J.; Liang, X.; Ramakrishna, S.; Sbai, A.; Gupta, R.; Mondal, A.; Hongyu, Z.; Yadav, A. Electronic Properties of 2D Materials and Their Junctions. *Nano Materials Science* **2024**, *6* (1), 1−23.
(8) Wang, G.; Chernikov, A.; Glazov, M. M.; Heinz, T. F.; Marie, X.; Amand, T.; Urbaszek, B. Colloquium: Excitons in Atomically Thin Transition Metal Dichalcogenides. *Rev. Mod. Phys.* **2018**, *90* (2), No. 021001.
(9) Bian, R.; Li, C.; Liu, Q.; Cao, G.; Fu, Q.; Meng, P.; Zhou, J.; Liu, F.; Liu, Z. Recent Progress in the Synthesis of Novel Two-Dimensional van Der Waals Materials. *National Science Review* **2022**, *9* (5), No. nwab164.
(10) Chaves, A.; Azadani, J. G.; Alsalman, H.; da Costa, D. R.; Frisenda, R.; Chaves, A. J.; Song, S. H.; Kim, Y. D.; He, D.; Zhou, J.; Castellanos-Gomez, A.; Peeters, F. M.; Liu, Z.; Hinkle, C. L.; Oh, S.-H.; Ye, P. D.; Koester, S. J.; Lee, Y. H.; Avouris, P.; Wang, X.; Low, T. Bandgap Engineering of Two-Dimensional Semiconductor Materials. *npj 2D Mater. Appl.* **2020**, *4* (1), 1−21.
(11) Brem, S.; Ekman, A.; Christiansen, D.; Katsch, F.; Selig, M.; Robert, C.; Marie, X.; Urbaszek, B.; Knorr, A.; Malic, E. Phonon-Assisted Photoluminescence from Indirect Excitons in Monolayers of Transition-Metal Dichalcogenides. *Nano Lett.* **2020**, *20* (4), 2849−2856.
(12) Mueller, T.; Malic, E. Exciton Physics and Device Application of Two-Dimensional Transition Metal Dichalcogenide Semiconductors. *npj 2D Mater. Appl.* **2018**, *2* (1), 1−12.
(13) Cardona, M. Modulation Spectroscopy of Semiconductors. In *Advances in Solid State Physics*; Madelung, O., Ed.; Pergamon, 1970; pp 125−173. DOI: 10.1016/B978-1-4831-2427-8.50007-3.
(14) Kudrawiec, R.; Walukiewicz, W. Electromodulation Spectroscopy of Highly Mismatched Alloys. *J. Appl. Phys.* **2019**, *126* (14), 141102.
(15) Zhang, C.; Wang, H.; Chan, W.; Manolatou, C.; Rana, F. Absorption of Light by Excitons and Trions in Monolayers of Metal Dichalcogenide $\mathrm{Mo}{\mathrm{S}}_{2}$: Experiments and Theory. *Phys. Rev. B* **2014**, *89* (20), No. 205436.
(16) Frisenda, R.; Niu, Y.; Gant, P.; Molina-Mendoza, A. J.; Schmidt, R.; Bratschitsch, R.; Liu, J.; Fu, L.; Dumcenco, D.; Kis, A.; De Lara, D. P.; Castellanos-Gomez, A. Micro-Reflectance and Transmittance Spectroscopy: A Versatile and Powerful Tool to Characterize 2D Materials. *J. Phys. D: Appl. Phys.* **2017**, *50* (7), No. 074002.
(17) Kim, J. H.; Jeong, J. H.; Kim, N.; Joshi, R.; Lee, G.-H. Mechanical Properties of Two-Dimensional Materials and Their Applications. *J. Phys. D: Appl. Phys.* **2019**, *52* (8), No. 083001.
(18) Tongay, S.; Suh, J.; Ataca, C.; Fan, W.; Luce, A.; Kang, J. S.; Liu, J.; Ko, C.; Raghunathanan, R.; Zhou, J.; Ogletree, F.; Li, J.; Grossman, J. C.; Wu, J. Defects Activated Photoluminescence in Two-Dimensional Semiconductors: Interplay between Bound, Charged and Free Excitons. *Sci. Rep* **2013**, *3* (1), 2657.
(19) Iikawa, F.; Bernussi, A. A.; Soares, A. G.; Plentz, F. O.; Motisuke, P.; Sacilotti, M. A. Luminescence and Photomodulated Transmission Measurements in InGaAs/GaAs Modulation Doped Single Quantum Wells. *J. Appl. Phys.* **1994**, *75* (6), 3071−3074.
(20) Kudrawiec, R.; Sęk, G.; Ryczko, K.; Misiewicz, J.; Harmand, J. C. Photoreflectance Investigations of Oscillator Strength and Broadening of Optical Transitions for GaAsSb−GaInAs/GaAs Bilayer Quantum Wells. *Appl. Phys. Lett.* **2004**, *84* (18), 3453−3455.
(21) Yin, X.; Pollak, F. H. Novel Contactless Mode of Electroreflectance. *Appl. Phys. Lett.* **1991**, *59* (18), 2305−2307.
(22) Kopaczek, J.; Polak, M. P.; Scharoch, P.; Wu, K.; Chen, B.; Tongay, S.; Kudrawiec, R. Direct Optical Transitions at K- and H-Point of Brillouin Zone in Bulk MoS2, MoSe2, WS2, and WSe2. *J. Appl. Phys.* **2016**, *119* (23), 235705.
(23) Ciesiołkiewicz, K.; Kopaczek, J.; Zelewski, S. J.; Kudrawiec, R. Optical Fiber-Enhanced Photoreflectance and Contactless Electroreflectance Measurements of van Der Waals Crystals and III-V Semiconductor Materials. *Measurement* **2025**, *253*, No. 117678.
(24) Polovnikov, B.; Scherzer, J.; Misra, S.; Huang, X.; Mohl, C.; Li, Z.; Göser, J.; Förste, J.; Bilgin, I.; Watanabe, K.; Taniguchi, T.; Högele, A.; Baimuratov, A. S. Field-Induced Hybridization of Moir\'e Excitons in ${\mathrm{MoSe}}_{2}/{\mathrm{WS}}_{2}$ Heterobilayers. *Phys. Rev. Lett.* **2024**, *132* (7), No. 076902.
(25) Pataniya, P. M.; Tannarana, M.; Zankat, C. K.; Bhakhar, S. A.; Narayan, S.; Solanki, G. K.; Patel, K. D.; Jha, P. K.; Pathak, V. M. Low-Temperature Raman Investigations and Photoresponse of a Detector Based on High-Quality WSe2 Crystals. *J. Phys. Chem. C* **2020**, *124* (4), 2251−2257.
(26) Huang, J.; Hoang, T.; Mikkelsen, M. Probing the Origin of Excitonic States in Monolayer WSe2. *Sci. Rep.* **2016**, *6*, 22414.
(27) Tamulewicz-Szwajkowska, M.; Zelewski, S. J.; Serafińczuk, J.; Kudrawiec, R. Geometric Progress in the Thickness of Exfoliated van Der Waals Crystals on the Example of MoS2. *AIP Advances* **2022**, *12* (2), No. 025328.
(28) Li, Y.; Kuang, G.; Jiao, Z.; Yao, L.; Duan, R. Recent Progress on the Mechanical Exfoliation of 2D Transition Metal Dichalcogenides. *Mater. Res. Express* **2022**, *9* (12), 122001.
(29) Battesti, R.; Beard, J.; Böser, S.; Bruyant, N.; Budker, D.; Crooker, S. A.; Daw, E. J.; Flambaum, V. V.; Inada, T.; Irastorza, I. G.; Karbstein, F.; Kim, D. L.; Kozlov, M. G.; Melhem, Z.; Phipps, A.; Pugnat, P.; Rikken, G.; Rizzo, C.; Schott, M.; Semertzidis, Y. K.; ten Kate, H. H. J.; Zavattini, G. High Magnetic Fields for Fundamental Physics. *Phys. Rep.* **2018**, *765−766*, 1−39.
(30) Crooker, S. A. Fiber-Coupled Antennas for Ultrafast Coherent Terahertz Spectroscopy in Low Temperatures and High Magnetic Fields. *Rev. Sci. Instrum.* **2002**, *73* (9), 3258−3264.
(31) Stier, A. V.; Wilson, N. P.; Clark, G.; Xu, X.; Crooker, S. A. Probing the Influence of Dielectric Environment on Excitons in Monolayer WSe2: Insight from High Magnetic Fields. *Nano Lett.* **2016**, *16* (11), 7054−7060.
(32) Stier, A. V.; Wilson, N. P.; Velizhanin, K. A.; Kono, J.; Xu, X.; Crooker, S. A. Magnetooptics of Exciton Rydberg States in a Monolayer Semiconductor. *Phys. Rev. Lett.* **2018**, *120* (5), No. 057405.
(33) Ciesiołkiewicz, K.; Kopaczek, J.; Kudrawiec, R. Thermotransmittance Spectroscopy of Layered Crystals Using Lab on Fiber. *Nanoscale* **2025**, *17* (28), 16818−16828.
(34) Hu, L.; Shan, X.; Wu, Y.; Zhao, J.; Lu, X. Laser Thinning and Patterning of MoS2 with Layer-by-Layer Precision. *Sci. Rep* **2017**, *7* (1), 15538.

(35) Disterhoft, P. Stability Characteristics of 1000 W FEL-Type QTH Lamps during the Seasoning and Screening Process. In *Ultraviolet Ground- and Space-based Measurements, Models, and Effects V*; SPIE, 2005; Vol. *5886*, pp 124−135. DOI: 10.1117/12.614584.
(36) Guerra Davila, Y.; Silva, F. W. N.; Oliveira, M. C. D.; Yu, Z.; Carvalho, T. C. V.; dos Santos, C. C.; Souza Filho, A. G.; Terrones, M.; Alencar, R. S.; Viana, B. C. Temperature and Power-Dependent Photoluminescence Spectroscopy in Suspended WSe2Monolayer. *J. Phys. D: Appl. Phys.* **2024**, *57* (16), 165304.
(37) Arora, A.; Koperski, M.; Nogajewski, K.; Marcus, J.; Faugeras, C.; Potemski, M. Excitonic Resonances in Thin Films of WSe2: From Monolayer to Bulk Material. *Nanoscale* **2015**, *7* (23), 10421−10429.
(38) Zhang, X.-X.; You, Y.; Zhao, S. Y. F.; Heinz, T. F. Experimental Evidence for Dark Excitons in Monolayer ${\mathrm{WSe}}_{2}$. *Phys. Rev. Lett.* **2015**, *115* (25), No. 257403.
(39) Wang, G.; Robert, C.; Suslu, A.; Chen, B.; Yang, S.; Alamdari, S.; Gerber, I. C.; Amand, T.; Marie, X.; Tongay, S.; Urbaszek, B. Spin-Orbit Engineering in Transition Metal Dichalcogenide Alloy Monolayers. *Nat. Commun.* **2015**, *6* (1), 10110.
(40) Jadczak, J.; Kutrowska-Girzycka, J.; Kapuściński, P.; Huang, Y. S.; Wójs, A.; Bryja, L. Probing of Free and Localized Excitons and Trions in Atomically Thin WSe2, WS2, MoSe2 and MoS2 in Photoluminescence and Reflectivity Experiments. *Nanotechnology* **2017**, *28* (39), 395702.
(41) Jadczak, J.; Glazov, M.; Kutrowska-Girzycka, J.; Schindler, J. J.; Debus, J.; Ho, C.-H.; Watanabe, K.; Taniguchi, T.; Bayer, M.; Bryja, L. Upconversion of Light into Bright Intravalley Excitons via Dark Intervalley Excitons in hBN-Encapsulated WSe2Monolayers. *ACS Nano* **2021**, *15* (12), 19165−19174.
(42) Ryu, H.; Hong, S. C.; Kim, K.; Jung, Y.; Lee, Y.; Lee, K.; Kim, Y.; Kim, H.; Watanabe, K.; Taniguchi, T.; Kim, J.; Kim, K.; Cheong, H.; Lee, G.-H. Optical Grade Transformation of Monolayer Transition Metal Dichalcogenides via Encapsulation Annealing. *Nanoscale* **2024**, *16* (11), 5836−5844.
(43) 2 - PHOTOPHYSICS. In *Handbook of UV Degradation and Stabilization*, 2nd ed.; Wypych, G., Ed.; ChemTec Publishing, 2015; pp 9−35. DOI: 10.1016/B978-1-895198-86-7.50004-8.
(44) Niu, Y.; Gonzalez-Abad, S.; Frisenda, R.; Marauhn, P.; Drüppel, M.; Gant, P.; Schmidt, R.; Taghavi, N. S.; Barcons, D.; Molina-Mendoza, A. J.; De Vasconcellos, S. M.; Bratschitsch, R.; Perez De Lara, D.; Rohlfing, M.; Castellanos-Gomez, A. Thickness-Dependent Differential Reflectance Spectra of Monolayer and Few-Layer MoS2, MoSe2, WS2 and WSe2. *Nanomaterials* **2018**, *8* (9), 725.
(45) Li, Y.; Li, X.; Yu, T.; Yang, G.; Chen, H.; Zhang, C.; Feng, Q.; Ma, J.; Liu, W.; Xu, H.; Liu, Y.; Liu, X. Accurate Identification of Layer Number for Few-Layer WS2 and WSe2 via Spectroscopic Study. *Nanotechnology* **2018**, *29* (12), 124001.
(46) Zhao, W.; Ghorannevis, Z.; Chu, L.; Toh, M.; Kloc, C.; Tan, P.-H.; Eda, G. Evolution of Electronic Structure in Atomically Thin Sheets of WS2 and WSe2. *ACS Nano* **2013**, *7* (1), 791−797.
(47) Stevens, C. E.; Stroucken, T.; Stier, A. V.; Paul, J.; Zhang, H.; Dey, P.; Crooker, S. A.; Koch, S. W.; Karaiskaj, D. Superradiant Coupling Effects in Transition-Metal Dichalcogenides. *Optica, OPTICA* **2018**, *5* (6), 749−755.
(48) Yeh, P.-C.; Jin, W.; Zaki, N.; Zhang, D.; Liou, J. T.; Sadowski, J. T.; Al-Mahboob, A.; Dadap, J. I.; Herman, I. P.; Sutter, P.; Osgood, R. M. Layer-Dependent Electronic Structure of an Atomically Heavy Two-Dimensional Dichalcogenide. *Phys. Rev. B* **2015**, *91* (4), No. 041407.
(49) Kopaczek, J.; Zelewski, S.; Yumigeta, K.; Sailus, R.; Tongay, S.; Kudrawiec, R. Temperature Dependence of the Indirect Gap and the Direct Optical Transitions at the High-Symmetry Point of the Brillouin Zone and Band Nesting in MoS2, MoSe2, MoTe2, WS2, and WSe2 Crystals. *J. Phys. Chem. C* **2022**, *126* (12), 5665−5674.
(50) Varshni, Y. P. Temperature Dependence of the Energy Gap in Semiconductors. *Physica* **1967**, *34* (1), 149−154.
(51) Kopaczek, J.; Dybała, F.; Zelewski, S. J.; Sokołowski, N.; Żuraw, W.; McNicholas, K. M.; El-Jaroudi, R. H.; White, R. C.; Bank, S. R.; Kudrawiec, R. Photoreflectance Studies of Temperature and Hydrostatic Pressure Dependencies of Direct Optical Transitions in BGaAs Alloys Grown on GaP. *J. Phys. D: Appl. Phys.* **2022**, *55* (1), No. 015107.
(52) Tołłoczko, A.; Zelewski, S. J.; Błaszczak, M.; Woźniak, T.; Siudzińska, A.; Bachmatiuk, A.; Scharoch, P.; Kudrawiec, R. Optical Properties of Orthorhombic Germanium Selenide: An Anisotropic Layered Semiconductor Promising for Optoelectronic Applications. *Journal of Materials Chemistry C* **2021**, *9* (41), 14838−14847.
(53) Tołłoczko, A.; Oliva, R.; Woźniak, T.; Kopaczek, J.; Scharoch, P.; Kudrawiec, R. Anisotropic Optical Properties of GeS Investigated by Optical Absorption and Photoreflectance. *Mater. Adv.* **2020**, *1* (6), 1886−1894.
(54) Kopaczek, J.; Sayyad, M. Y.; Sailus, R.; Wu, C.-L.; Moosavy, S. T. R.; Ruddick, H.; Kudrawiec, R.; Tongay, S. A. Promoting Interlayer Exciton in Janus/Transition Metal Dichalcogenide Heterostructures by Annealing. *ACS Appl. Electron. Mater.* **2025**, *7* (3), 997−1003.
(55) Gerber, I. C.; Courtade, E.; Shree, S.; Robert, C.; Taniguchi, T.; Watanabe, K.; Balocchi, A.; Renucci, P.; Lagarde, D.; Marie, X.; Urbaszek, B. Interlayer Excitons in Bilayer ${\mathrm{MoS}}_{2}$ with Strong Oscillator Strength up to Room Temperature. *Phys. Rev. B* **2019**, *99* (3), No. 035443.
(56) Arora, A.; Deilmann, T.; Marauhn, P.; Drüppel, M.; Schneider, R.; Molas, M. R.; Vaclavkova, D.; Michaelis de Vasconcellos, S.; Rohlfing, M.; Potemski, M.; Bratschitsch, R. Valley-Contrasting Optics of Interlayer Excitons in Mo- and W-Based Bulk Transition Metal Dichalcogenides. *Nanoscale* **2018**, *10* (33), 15571−15577.
(57) Barré, E.; Karni, O.; Liu, E.; O'Beirne, A. L.; Chen, X.; Ribeiro, H. B.; Yu, L.; Kim, B.; Watanabe, K.; Taniguchi, T.; Barmak, K.; Lui, C. H.; Refaely-Abramson, S.; da Jornada, F. H.; Heinz, T. F. Optical Absorption of Interlayer Excitons in Transition-Metal Dichalcogenide Heterostructures. *Science* **2022**, *376* (6591), 406−410.
(58) Aspnes, D. E. Third-Derivative Modulation Spectroscopy with Low-Field Electroreflectance. *Surf. Sci.* **1973**, *37*, 418−442.
(59) Yu, P. Y.; Cardona, M. *Fundamentals of Semiconductors: Physics and Materials Properties*; Graduate Texts in Physics; Springer: Berlin. *Heidelberg* **2010**, DOI: 10.1007/978-3-642-00710-1.
(60) Xiao, J.; Zhang, Y.; Chen, H.; Xu, N.; Deng, S. Enhanced Performance of a Monolayer MoS2/WSe2 Heterojunction as a Photoelectrochemical Cathode. *Nano-Micro Lett.* **2018**, *10* (4), 60.
(61) Rigosi, A. F.; Hill, H. M.; Li, Y.; Chernikov, A.; Heinz, T. F. Probing Interlayer Interactions in Transition Metal Dichalcogenide Heterostructures by Optical Spectroscopy: MoS2/WS2 and MoSe2/WSe2. *Nano Lett.* **2015**, *15* (8), 5033−5038.

2.4. Sensitivity of excitonic transitions to temperature in monolayers of TMD alloys

Citation:

Published in *arXiv,* 2025

DOI: 10.48550/arXiv.2509.03209

Co-authors:

Karolina Ciesiołkiewicz-Klepek, Jan Kopaczek, Jarosław Serafińczuk, Robert Kudrawiec

Author's contribution:

Karolina Ciesiołkiewicz designed the optical setup and built the complete measurement system, conducted all transmission measurements, collected and analyzed the data, prepared the figures and graphical representations of the results, developed the interpretation of the results, wrote the manuscript, and served as the corresponding author.

Context within the dissertation:

This article presents a comprehensive optical transmission study of monolayer alloys based on MoS_2, focusing on the temperature evolution of excitonic transitions in $Mo_{1-x}W_xS_2$ and $Mo(S_{1-x}Se_x)_2$. Using a lab-on-fiber system placed in a cryostat, the work provides detailed insights into the effects of composition and temperature on the band structure, exciton energies, and spin-orbit coupling strength. The findings contribute to the broader understanding of band gap engineering in TMDC monolayers and demonstrate the experimental capabilities of fiber-based transmission spectroscopy across a wide temperature range.

Sensitivity of excitonic transitions to temperature in monolayers of TMD alloys

K. Ciesiołkiewicz-Klepek[1, a)], J. Kopaczek[1], J. Serafińczuk[2], R. Kudrawiec[1, b)]

[1]*Department of Semiconductor Materials Engineering, Wroclaw University of Science and Technology, Wybrzeże Wyspiańskiego 27, 50-370 Wrocław, Poland*

[2]*Department of Nanometrology, Wroclaw University of Science and Technology, Wybrzeże Wyspiańskiego 27, 50-370 Wrocław, Poland*

[a)] *e-mail address: karolina.ciesiolkiewicz@pwr.edu.pl*
[b)] *e-mail address: robert.kudrawiec@pwr.edu.pl*

Two-dimensional transition metal dichalcogenides (TMDs) offer tunable optical and electronic properties, making them highly promising for next-generation optoelectronic devices. One effective approach to engineering these properties is through alloying, which enables continuous control over the bandgap energy and excitonic transitions. In this study, we perform temperature-dependent transmission spectroscopy on monolayers of $Mo_{1-x}W_xS_2$ and $Mo(S_{1-x}Se_x)_2$ alloys, transferred onto the core of an optical fiber and measured within a cryostat over a temperature range of 20–320 K. The use of an all-fiber configuration allowed us to probe interband transitions A, B, and C with high stability and precision. We observe a systematic redshift of excitonic transitions with increasing Se content, and a blueshift when Mo is replaced with W. These spectral shifts correlate with alloy composition and enable the tuning of bandgap energies between ~1.6 eV and ~2.0 eV at room temperature. Furthermore, we analyze the temperature sensitivity of the excitonic transitions, revealing that Se incorporation enhances thermal response in a non-monotonic manner, while W substitution results in a more monotonic and stronger temperature dependence. The splitting between A and B transitions, associated with spin-orbit coupling, also varies with composition. Our findings underscore the potential of compositional engineering in 2D TMD alloys to achieve both spectral and thermal control of optical properties, relevant for the design of robust and tunable optoelectronic systems.

Introduction

Two-dimensional (2D) transition metal dichalcogenides (TMDs) materials have attracted considerable attention due to their unique electronic[1–3] and optical properties[4], as well as their potential for applications in modern optoelectronic devices.[5] A key aspect in designing such devices – including light-emitting diodes, lasers, sensors, and modulators – is the ability to control the bandgap.[6,7] This control can be achieved either externally, through parameters such as temperature,[8] mechanical strain,[9] or internally, by modifying the material itself. Such internal modifications include the introduction of defects[10–12] or dopants,[13,14] variation in the number of layers[15,16], or alloying.[13,17,18] For instance, it is well known that reducing the thickness of TMDs from bulk to a monolayer changes their band structure from indirect to direct.[19,20] Commonly studied TMDs such as MoS_2 and WS_2 exhibit a fundamental direct bandgap at the K point of the Brillouin zone in the monolayer limit, with pronounced optical transitions labeled A and B.[21,22] These transitions arise from the valence band splitting caused by strong spin-orbit coupling.[23]

One promising route for tailoring the properties of 2D materials is through alloying, either on the cationic or the anionic sublattice.[13] This allows for continuous tuning of optical and electronic properties, including band edge positions, bandgap energies, spin-orbit interaction strength, and transition intensities.[18,24] While photoluminescence (PL) studies of two-dimensional alloys have been extensive, providing insights into neutral exciton, bound states, and carrier dynamics,[25] relatively little attention has been paid to absorption properties, particularly as a function of temperature and for well-defined monolayers.[26,27] Transmission spectroscopy enables the estimation of absorption spectra and offers a direct probe of the band structure, which can reveal phenomena that may be inaccessible through emission-based techniques, such as higher-energy interband transitions.[28] Additionally, temperature-dependent studies can reveal the strength of electron-phonon interactions and how they evolve across alloys of different compositions.

Performing transmission measurements over a broad temperature range remains technically challenging, especially for atomically thin layers. In this study, we utilize an optical fiber-based configuration, in which mechanically exfoliated monolayers of either $Mo_{1-x}W_xS_2$ or $Mo(S_{1-x}Se_x)_2$ are transferred onto the flat tip of the fiber, covering the entire core region. The fiber with a 2D crystal is placed inside a temperature-controlled cryostat, enabling stable and precise measurements in the range of 20 to 320 K. This allowed us to extract the energies of the interband transitions A, B, and C, and analyze temperature evolution of transition A and B using both Varshni and Bose-Einstein models.[29,30] Moreover, we show that by mixing materials such as MoS_2, WS_2, and $MoSe_2$, the bandgap can be tuned in the range of approximately 1.6 eV to 2.0 eV at room temperature, and from 1.65 eV to 2.09 eV at cryogenic temperatures. Special attention is also given to the temperature- and composition-dependent splitting between transitions A and B, which provides insights into the variation of spin-orbit interaction strength. Furthermore, we investigate how the choice of transition metal and chalcogen atoms influences the temperature sensitivity of the excitonic transitions and the overall tunability of the optical properties.

Experimental methods

Studied materials were obtained from commercially available bulk crystals with known compositions. However, to confirm the composition and crystalline quality of the materials, the $Mo(S_{1-x}Se_x)_2$ and $Mo_{1-x}W_xS_2$ alloys were investigated by X-ray diffraction (XRD) spectroscopy on a Malvern Panalytical Empyrean diffractometer equipped with a copper X-ray tube (λ = 1.540598 Å, $CuK\alpha_1$ radiation). Data were collected in the Bragg–Brentano geometry over a 2θ range of 10° - 80°. For the $Mo(S_{1-x}Se_x)_2$ sample, a fragment of the bulk crystal was placed on a Si/SiO_2 substrate and measured over the previously specified scan range. For the $Mo_{1-x}W_xS_2$ alloy, thin flakes were mechanically exfoliated from the bulk crystal, transferred onto the same type of substrate, and then measured. The exfoliation step was necessary because compositional inhomogeneity in the bulk $Mo_{1-x}W_xS_2$ crystal led to ambiguous results when the intact crystal was measured. Lattice parameters were calculated from the (00.6) reflection of $Mo(S_{1-x}Se_x)_2$ and the (00.2) reflection of $Mo_{1-x}W_xS_2$. Assuming a linear dependence of the lattice constant on composition, and taking the lattice parameter of MoS_2 as the 0% reference and that of WS_2 (or $MoSe_2$) as the 100% reference, the alloy compositions were determined to be 17, 43, 64 and 79% W in $Mo_{1-x}W_xS_2$ and 16, 26, 44, and 55% S in $Mo(S_{1-x}Se_x)_2$, respectively (Figure S1).

The monolayer samples were prepared by mechanical exfoliation and transferred onto the flat end-face of an optical fiber. To improve the adhesion and ensure clean transfer, the fiber tip was gently heated during the process. The fiber with a monolayer was then mounted on the cold finger inside a closed-cycle helium cryostat, allowing for stable temperature control during the experiment. Transmission measurements were carried out by coupling light from a quartz tungsten halogen lamp into the fiber, guiding it through the exfoliated monolayer positioned at the fiber tip, and collecting the transmitted signal with a second fiber aligned at the output. The transmitted spectra were recorded using an optical portable spectrometer. This setup enabled temperature-dependent measurements to be performed across a broad range, from 20 to 320 K.

Results and discussion

In this study, we investigated how alloying molybdenum disulfide (MoS_2) with either tungsten (cationic alloying) or selenium (anionic alloying) affects its optical properties, as revealed by transmission spectroscopy. Specifically, samples with varying compositions of $Mo_{1-x}W_xS_2$ and $Mo(S_{1-x}Se_x)_2$ were investigated to understand how changes in chemical composition influence the positions of characteristic optical transitions, i.e., A, B, and C excitons. Figures 1b and 1c present the transmission spectra recorded at 20 K for both alloys of selected compositions. For all samples, transitions A and B are clearly resolved, while the high-energy C transition, associated with band nesting,[31] is significantly broader and less pronounced, thus limiting the precision in determining its peak position. This is likely due to its origin away from high-symmetry points of the Brillouin zone, where the band structure is more complex and the density of states is higher.[32–34] The A excitonic transition, corresponding to the direct bandgap at the K point of the Brillouin zone, shifts in energy depending on the material composition, from 1.63 eV in $MoSe_2$ to 2.09 eV in WS_2. The simplified schematic of the TMD alloy monolayers discussed here is presented in Figure 1a. A clear trend is observed depending on the type of alloying: chalcogen substitution (Se for S) results in a redshift of the spectral features, whereas metal substitution (W for Mo) leads to a blueshift. This behavior can be understood by considering the atomic properties of the substituting elements. Selenium has a larger atomic radius and lower electronegativity than sulfur, leading to weaker orbital overlap and a reduced crystal field strength around the transition metal, which, in turn, lowers the bandgap and results in a redshift of optical transitions.[35,36] In contrast, although molybdenum and tungsten have similar atomic radii, tungsten has a higher atomic number and significantly stronger spin–orbit coupling. This leads to greater splitting of the valence bands and a modified electronic band structure that increases the bandgap energy, manifesting as a blueshift in the optical spectra.[37] These trends are illustrated in Figure 1d, which shows the energies of A and B excitonic transitions as a function of alloy composition. The extracted bowing parameters for the A excitonic transition were $b_A=0.024\pm0.014$[38] for the $Mo(S_{1-x}Se_x)_2$ alloy and $b_A=0.17\pm0.05$[39,40] for the $Mo_{1-x}W_xS_2$ system, while for the B exciton, the bowing values were $b_B=0.018\pm0.012$[38] and $b_B=0.054\pm0.037$[25], respectively. These values are consistent with previously reported data for similar alloy systems, indicating that the variation in excitonic transition energies with composition follows nonlinear behavior. However, it is important to note that in both cases, the bowing parameters are close to zero, which implies structural and electronic similarity between the alloy constituents. Moreover, the energy separation between transitions A and B, corresponding to the spin-orbit splitting of the valence band, is also considered, as shown in Figure 1e. The smallest A–B splitting is observed for pure MoS_2 and increases with both chalcogen and metal alloying. However, the effect is significantly stronger for metal substitution: for WS_2, the splitting reaches up to 0.4 eV. This observation is consistent with theoretical expectations, as tungsten atoms exhibit stronger spin–orbit coupling than molybdenum, resulting in greater splitting of the valence bands at the K point.[41] In contrast, the substitution of sulfur with selenium also influences the spin–orbit interaction, but to a lesser extent due to the smaller difference in atomic mass and spin–orbit coupling strength between S and Se.[23]

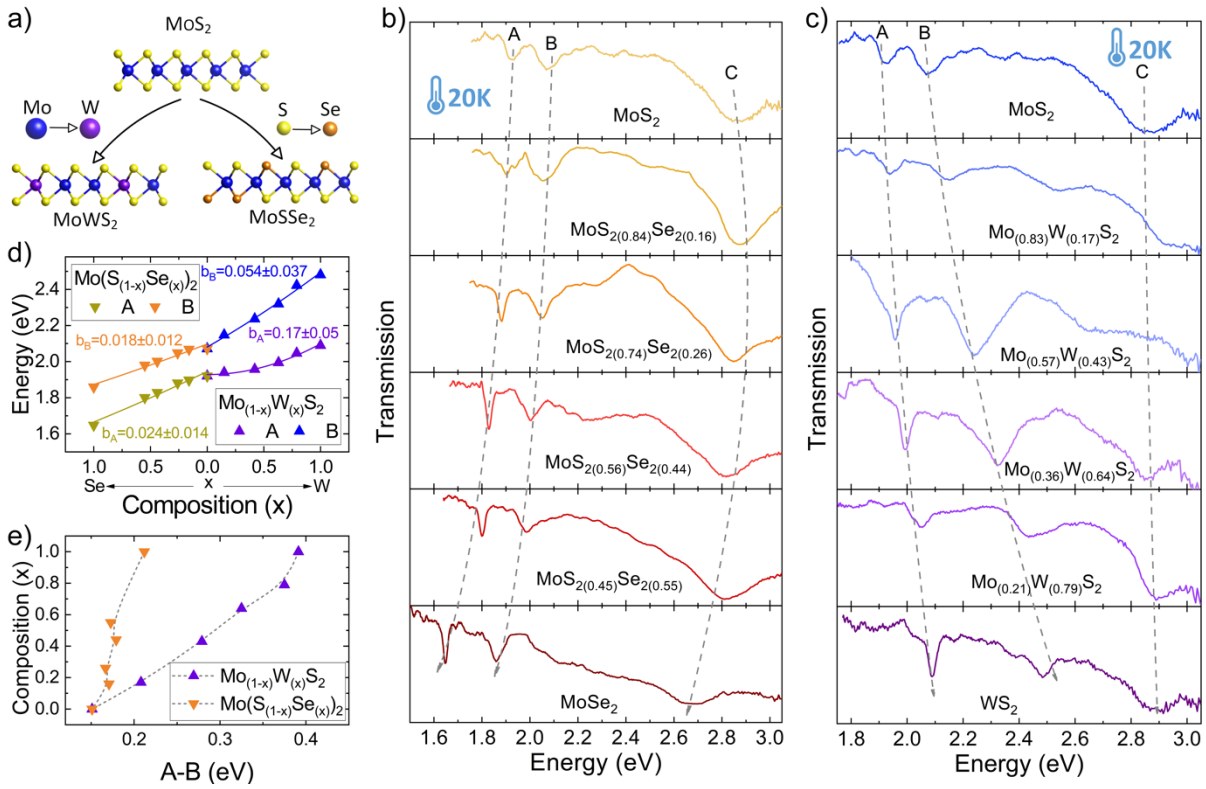

Figure 1. (a) Schematic representation of the studied TMD alloy monolayers: $Mo_{1-x}W_xS_2$, with blue Mo, yellow S, and purple W atoms; and $Mo(S_{1-x}Se_x)_2$, with orange Se atoms. Transmission spectra of (b) $Mo_{1-x}W_xS_2$ and (c) $Mo(S_{1-x}Se_x)_2$ samples measured at 20 K. (d) Composition-dependent energies of A and B excitons for $Mo_{1-x}W_xS_2$ and $Mo(S_{1-x}Se_x)_2$. (e) Composition-dependent energy splitting between A and B transitions for $Mo_{1-x}W_xS_2$ and $Mo(S_{1-x}Se_x)_2$.

As described earlier, a monolayer of each alloy composition was transferred onto the flat-cleaved facet of a multimode optical fiber and placed in a closed-cycle cryostat. To study the impact of external stimuli, transmission spectra were recorded over a wide temperature range from 320 down to 20 K. Representative results are presented in Figure 2 for the $Mo(S_{1-x}Se_x)_2$ alloy series, from pure MoS_2 through intermediate compositions to pure $MoSe_2$. A systematic blueshift of transitions A, B, and C is observed as the temperature decreases. For most compositions, transitions A and B remain clearly resolved up to room temperature, allowing reliable peak extraction across the entire range. In contrast, the C transition appears significantly broadened and exhibits minimal temperature-dependent shift. Due to the increased uncertainty in determining its peak position, this feature was excluded from further quantitative analysis.

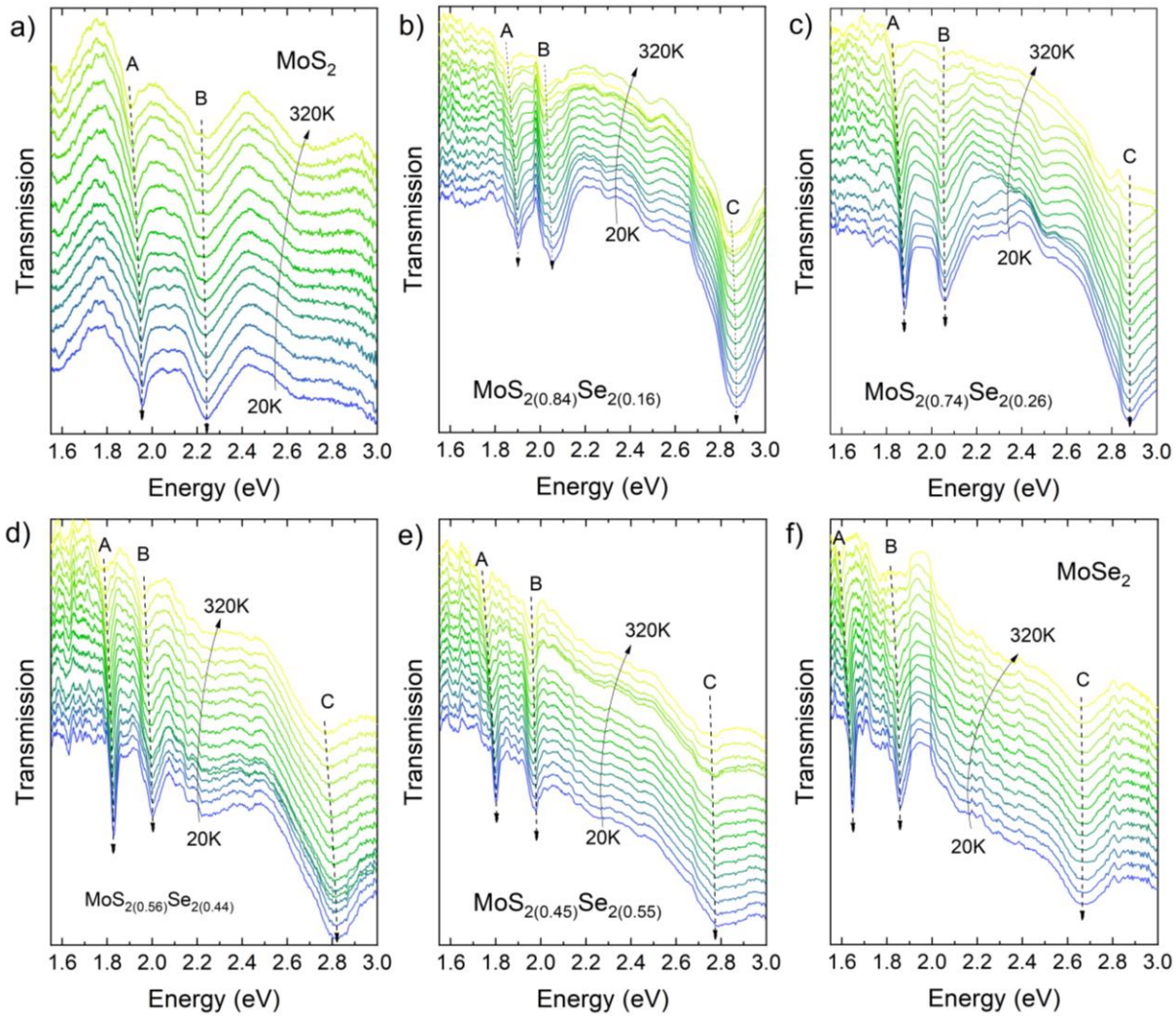

Figure 2. Transmission spectra of $Mo(S_{1-x}Se_x)_2$ alloys with varying selenium content, measured in the temperature range 20–320 K. Panels (a)–(f) correspond to increasing Se concentration. A clear shift of the transmission minimum with increasing temperature and Se content is observed, reflecting changes in the optical transition energies of the studied materials.

Furthermore, Figure 3 shows the analogous results for $Mo_{1-x}W_xS_2$ alloy monolayers, following the same trend. A pronounced blueshift of the A and B excitonic transitions is again observed as temperature decreases. The energy of excitonic transitions was extracted using a Gaussian fitting procedure applied to each peak. As expected from excitonic behavior, the amplitude of the features increases at lower temperatures, while their linewidths decrease due to reduced electron–phonon interaction strength and a lower phonon population.

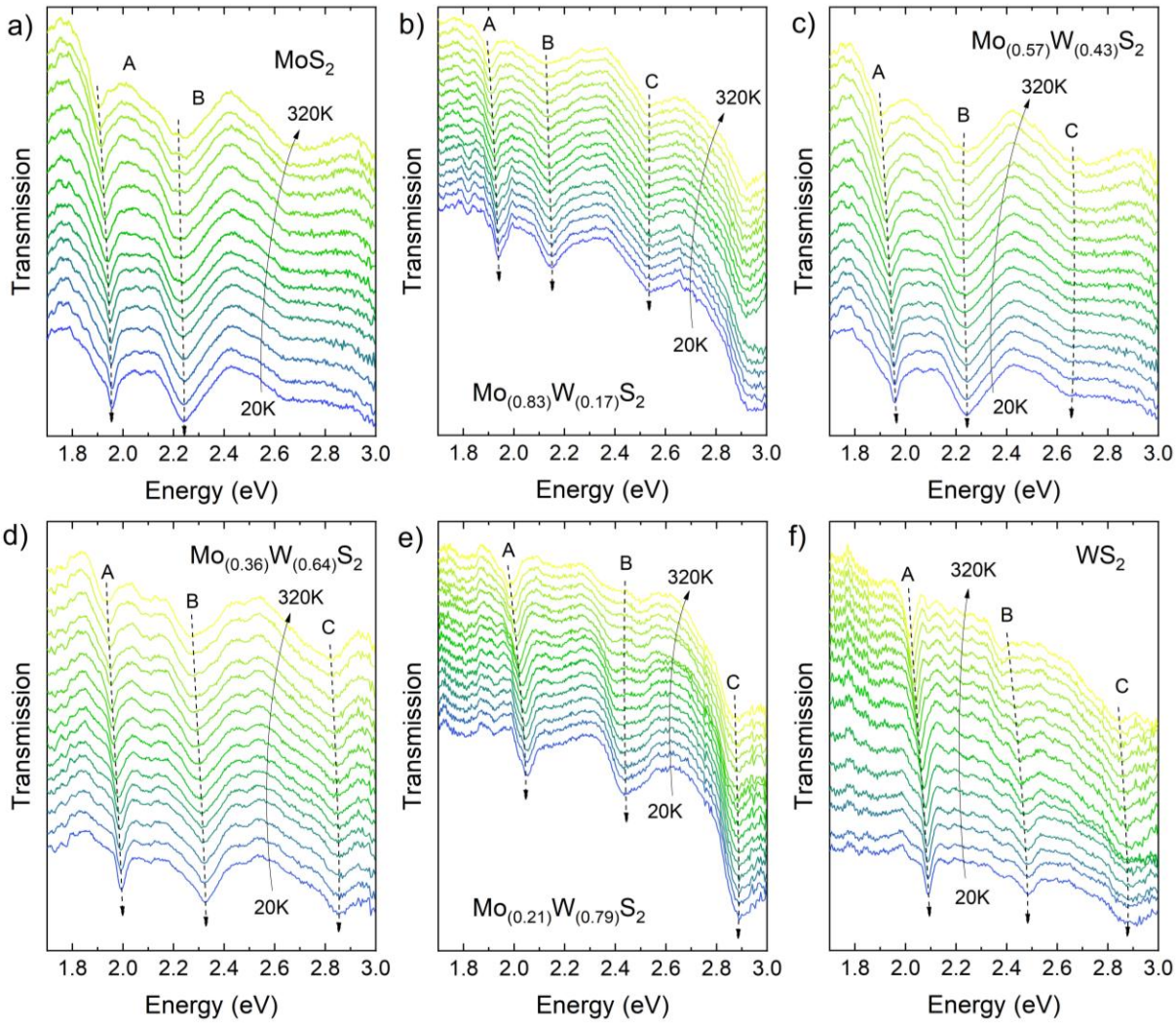

Figure 3. Transmission spectra of $Mo_{1-x}W_xS_2$ alloys with varying selenium content, measured in the temperature range 20–320 K. Panels (a)–(f) correspond to increasing W concentration. A clear shift of the transmission minimum with increasing temperature and W content is observed, reflecting changes in the optical transition energies of the studied materials.

The extracted A and B exciton energies as a function of temperature are plotted in Figure 4 for all compositions and for both alloys. For the A transition in the $Mo(S_{1-x}Se_x)_2$ series, we observe that the rate of energy decrease with increasing temperature is directly correlated with the chalcogen content. It can be seen that pure MoS_2 shows the smallest thermal shift, and $MoSe_2$ the largest, which is consistent with previous studies.[8] Similarly, the $Mo_{1-x}W_xS_2$ alloy exhibits a systematic evolution: WS_2 undergoes the strongest thermal shift, and this effect gradually diminishes toward MoS_2 as the W content decreases. In all investigated materials trend is more pronounced for transition A than for B, where the incorporation of tungsten increases the temperature sensitivity of the B exciton to a lesser extent. This suggests that the A exciton is more sensitive to changes in the electronic band structure and exciton-phonon coupling introduced by metal substitution.

To quantitatively describe the temperature dependence of the excitonic transitions, the data were fitted using both the Varshni model (Figure 4) and a Bose-Einstein-type model. The Varshni equation is an empirical model commonly used to describe the temperature-induced bandgap shrinkage:

$$E_g(T) = E_0 - \frac{\alpha T^2}{T+\beta} \quad (1)$$

where $E_g(T)$ is the transition energy at temperature T, E_0 is the energy at 0 K, and α is a material-specific coefficient that quantifies the strength of the bandgap reduction with temperature related to electron-

phonon coupling and thermal expansion effects; β is a parameter that can be interpreted as an effective temperature scale at which the bandgap energy changes more rapidly.[29] Additionally, we employed a Bose-Einstein model that accounts more explicitly for exciton-phonon interactions:

$$E_g(T) = E_0 - \frac{a_B}{\exp\left(\frac{\theta_B}{T}\right)-1} \quad (2)$$

Where a_B is a coupling constant that represents the strength of the exciton–phonon interaction, and θ_B is an effective phonon temperature and is related to the average energy of the phonons involved in the interaction.[30] Both models were applied to the extracted A and B transition energies across the whole temperature range. The resulting fitting parameters are summarized in Table 1.

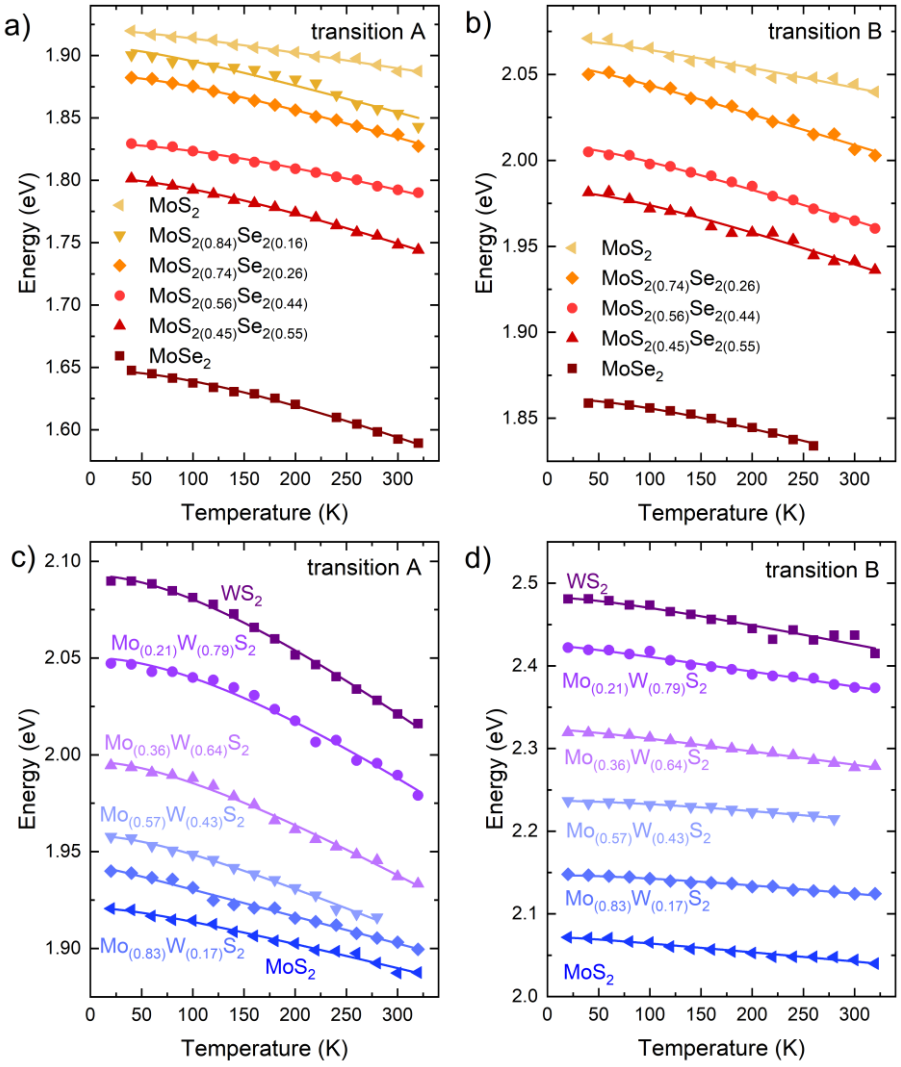

Figure 4. The temperature dependence of the excitonic transition energies, along with the corresponding Varshni fits, reveals how the thermal sensitivity of these materials varies systematically with composition: in the $Mo(S_{1-x}Se_x)_2$ alloy, transitions A (a) and B (b), and in $Mo_{1-x}W_xS_2$ transitions A (c) and B (d).

These observations are also illustrated in Figure 5, which shows the total energy shifts of the A and B excitonic transitions as a function of temperature for all the studied materials. For the A transition in pure MoS_2, the shift is only about 35 meV, indicating low sensitivity to temperature changes, consistent with expectations and the trends discussed earlier for this material. In contrast, the B transitions exhibit more variability, possibly due to how the lower valence band (split by spin-orbit interaction) interacts with phonons or responds to alloy disorder.[42] For the $Mo(S_{1-x}Se_x)_2$ alloys, the A transition shifts range from 35 to 60 meV, while the B transitions span from 10 to 47 meV. This reflects a higher temperature

sensitivity compared to pure MoS_2, particularly for the A exciton. The $Mo_{1-x}W_xS_2$ alloys show even more pronounced temperature-induced shifts: from 35 to 75 meV for the A transition, and from 10 to 67 meV for the B transition when Mo is replaced with W. These large shifts indicate stronger exciton–phonon interactions, likely due to both the heavier atomic mass of W compared to Mo (affecting optical phonon modes) and more delocalized electronic states that enhance coupling with lattice vibrations.[43,44] The increasing range of energy shifts with higher W or Se content suggests that the temperature sensitivity of the bandgap can be tuned through composition, which is relevant for designing optoelectronic devices operating under variable thermal conditions.

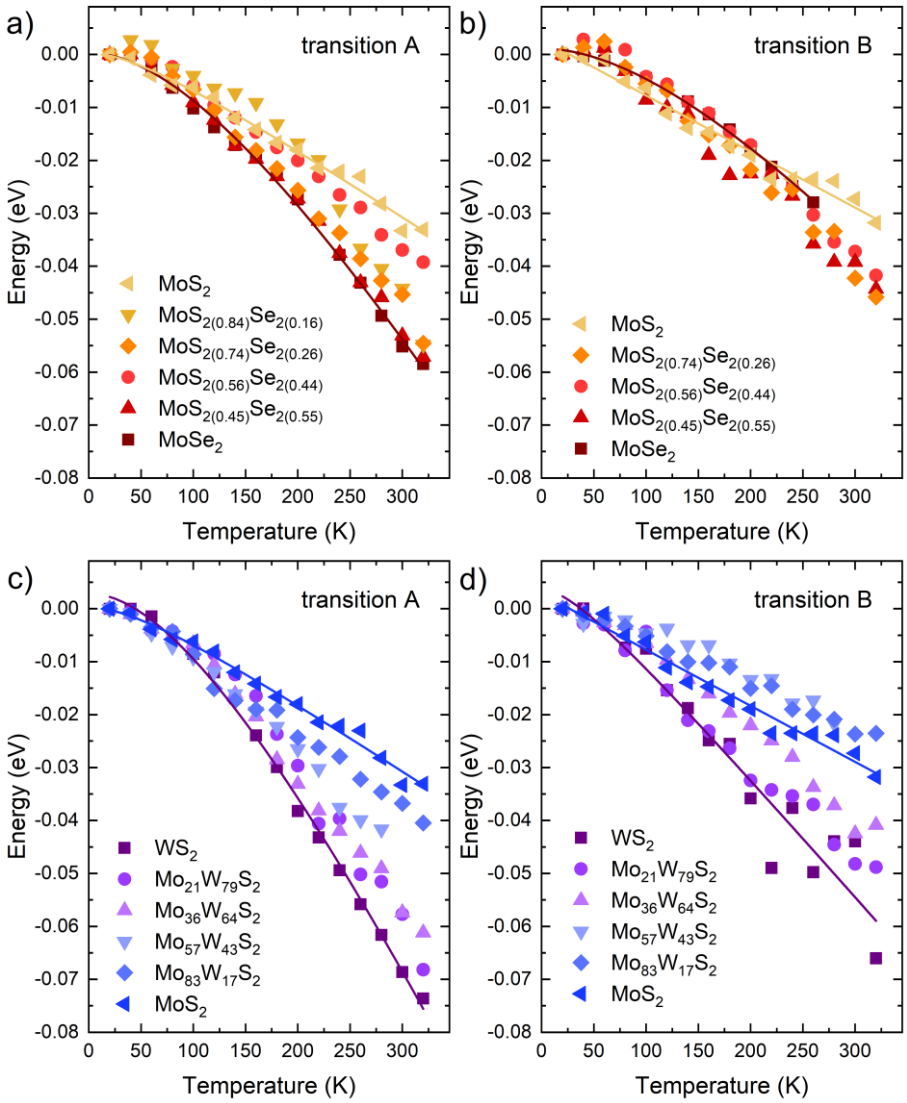

Figure 5. Total energy shift of the A and B excitonic transitions between 20 and 320 K for $Mo(S_{1-x}Se_x)_2$ and $Mo_{1-x}W_xS_2$ alloys.

In the case of the A transition in $Mo_{1-x}W_xS_2$ alloys, both α and a_B parameters increase significantly with increasing W content. This indicates that the sensitivity of exciton energy to temperature is stronger in WS_2-rich samples and gradually weakens as the composition shifts toward MoS_2.These trends show that MoS_2 has a more thermally stable bandgap, which, considering its less stiff lattice compared to WS_2,[45] further supports the dominant role of exciton-phonon coupling in thermally induced bandgap changes. Moreover, the $Mo(S_{1-x}Se_x)_2$ alloys, where the chalcogen atom is gradually substituted from S to Se, also display systematic behavior. The Se-rich alloy shows the highest values of α and a_B, indicating strong exciton-phonon interaction and significant energy shifts with temperature, which decrease monotonically for the intermediate compositions of the ternary alloy. However, when considering both alloy systems, the temperature-induced energy shift is greater upon W substitution, indicating that metal

substitution has a stronger impact on the lattice structure and exciton-phonon coupling than chalcogen substitution, at least in the context of temperature-dependent optical properties.

Table 1. Varshni and Bose-Einstein fitting results for the temperature-induced energy shifts of A and B excitons.

Material	*transition*	E_0 *(eV)*	α *(10^{-4} eV/K)*	E_0 *(eV)*	a_B *(meV)*
MoS_2	A	1.9207(15)	1.33(30)	1.92222(64)	2.89(2.0)
	B	2.0706(11)	1.26(15)	2.071(94)	5.6(1.6)
$MoS_{2(0.84)}Se_{2(16)}$	A	1.9073(15)	2.34(30)	1.9034(17)	15.1(2.0)
$MoS_{2(0.74)}Se_{2(0.26)}$	A	1.8845(54)	2.68(37)	1.8829(13)	20.6(4.0)
	B	2.0560(10)	1.826(62)	2.05335(92)	8.93(94)
$MoS_{2(0.56)}Se_{2(0.44)}$	A	1.8297(49)	2.49(22)	1.83031(74)	17.2(2.7)
	B	2.0089(64)	1.949(46)	2.0082(74)	9.56(85)
$MoS_{2(0.45)}Se_{2(0.55)}$	A	1.8022(77)	3.12(29)	1.80016(98)	26.7(4.3)
	B	1.9826(12)	2.152(42)	1.9830(12)	10.6(1.4)
$MoSe_2$	A	1.6480(11)	3.62(56)	1.6460(13)	30.6(6.2)
	B	1.8606(39)	1.85(55)	1.86090(30)	12(3)
$Mo_{(0.83)}W_{(0.17)}S_2$	A	1.9425(25)	1.40(34)	1.9413(67)	3.51(4.85)
	B	2.1469(48)	1.247(96)	2.14778(41)	6.06(76)
$Mo_{(0.57)}W_{(0.43)}S_2$	A	1.95827(87)	2.34(27)	1.9572(95)	15.0(3.5)
	B	2.2343(67)	1.38(22)	2.2354(11)	7.17(60)
$Mo_{(0.36)}W_{(0.64)}S_2$	A	1.9965(13)	3.17(41)	1.9942(11)	28.1(4.7)
	B	2.3231(73)	1.655(92)	2.3217(67)	8.14(88)
$Mo_{(0.21)}W_{(0.79)}S_2$	A	2.0502(12)	4.15(26)	2.0420(11)	36.7(1.2)
	B	2.4247(31)	1.85(38)	2.4222(12)	9.4(1.5)
WS_2	A	2.09269(96)	4.43(48)	2.09003(59)	40.6(3.2)
	B	2.4828(25)	2.52(38)	2.4829(25)	11.1(1.6)

To better visualize the temperature-dependent behavior of the excitonic transitions, both the α and a_B parameters are presented graphically in Figure 6, where the left Y-axis corresponds to the values obtained from the Varshni model, while the right Y-axis reflects those from the Bose-Einstein model. As shown, both models reveal the same qualitative trends for each material system, confirming their consistency in describing the exciton-phonon interaction strength. Although the temperature dependence of excitonic transitions in TMDCs has been extensively studied in bulk crystals, the behavior observed in monolayers is distinct due to their reduced dimensionality. In monolayer systems, both the Varshni and Bose–Einstein parameters tend to be systematically lower than in bulk counterparts, reflecting weaker exciton–phonon coupling. Our results confirm this trend across all studied compounds. The temperature-induced redshift of excitonic transitions is less pronounced in monolayers, and the associated parameters show a clear dependence on material composition. In $Mo_{1-x}W_xS_2$ alloys, increasing tungsten content leads to higher sensitivity to temperature, with the most significant changes occurring in WS_2-rich samples. This suggests that lattice composition can partially compensate for the dimensional reduction by enhancing coupling to specific phonon modes.

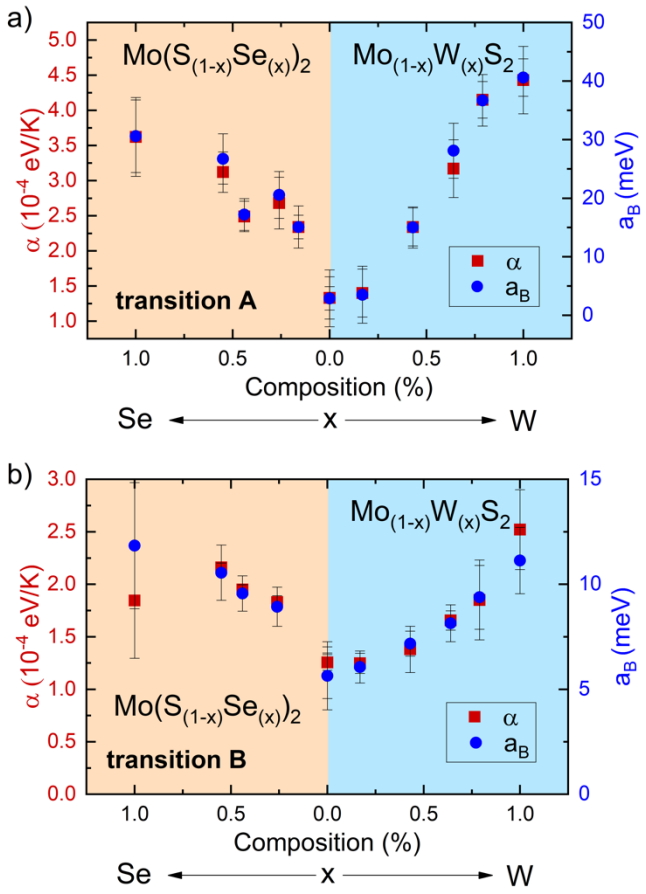

Figure 6. Comparison of the parameters α (Varshni model) and a_B (Bose–Einstein model) for different compositions of $Mo_{1-x}W_xS_2$ and $Mo(S_{1-x}Se_x)_2$.

Summary

In this article, we investigated the shift of the fundamental excitonic transitions A, B, and C in monolayer alloys derived from MoS_2 as the base material. Introducing selenium (Se) on a chalcogen site leads to a redshift of the transitions (i.e., lower energy), while substituting molybdenum (Mo) with tungsten (W) on a transition metal site causes a blueshift (i.e., higher energy). These trends provide valuable insights into how the chemical composition can be tuned to achieve excitonic transitions at desired wavelengths in a controlled and stable manner. Another key aspect of our study was the investigation of temperature-dependent behavior. It was found that replacing sulfur with selenium increases the material's sensitivity to temperature. On the other hand, substituting Mo with W results in a stronger temperature dependence, likely due to the heavier atomic mass of tungsten. In this case, the energy shifts exhibit more monotonic behavior with respect to the alloy composition. These findings highlight the importance of composition engineering for both spectral and thermal control in transition metal dichalcogenide alloys.

Conflict of Interest Statement

The authors have no conflicts to disclose.

Acknowledgments

This work was supported by the National Science Centre (NCN) Poland OPUS 23 no. 2022/45/B/ST7/02750.

Data availability

The data that support the findings of this study are openly available in Zenodo, at https://doi.org/10.5281/zenodo.16632871, reference number 10.5281/zenodo.16632871.

References

(1) A Review of the Synthesis, Properties, and Applications of 2D Materials - Shanmugam - 2022 - Particle & Particle Systems Characterization - Wiley Online Library. https://onlinelibrary.wiley.com/doi/full/10.1002/ppsc.202200031 (accessed 2024-12-30).

(2) Dutta, T.; Yadav, N.; Wu, Y.; Cheng, G. J.; Liang, X.; Ramakrishna, S.; Sbai, A.; Gupta, R.; Mondal, A.; Hongyu, Z.; Yadav, A. Electronic Properties of 2D Materials and Their Junctions. Nano Materials Science **2023**. https://doi.org/10.1016/j.nanoms.2023.05.003.

(3) Hu, J.-Q.; Shi, X.-H.; Wu, S.-Q.; Ho, K.-M.; Zhu, Z.-Z. Dependence of Electronic and Optical Properties of MoS2 Multilayers on the Interlayer Coupling and Van Hove Singularity. Nanoscale Res Lett **2019**, 14 (1), 288. https://doi.org/10.1186/s11671-019-3105-9.

(4) Zheng, W.; Jiang, Y.; Hu, X.; Li, H.; Zeng, Z.; Wang, X.; Pan, A. Light Emission Properties of 2D Transition Metal Dichalcogenides: Fundamentals and Applications. Advanced Optical Materials **2018**, 6 (21), 1800420. https://doi.org/10.1002/adom.201800420.

(5) Jin, L.; Wang, H.; Cao, R.; Khan, K.; Tareen, A. K.; Wageh, S.; Al-Ghamdi, A.; Li, S.; Li, D.; Zhang, Y. The Rise of 2D Materials/Ferroelectrics for next Generation Photonics and Optoelectronics Devices. APL Materials **2022**, 10, 60903. https://doi.org/10.1063/5.0094965.

(6) All-Optical Modulation Technology Based on 2D Layered Materials. https://www.mdpi.com/2072-666X/13/1/92 (accessed 2025-04-16).

(7) Kumbhakar, P.; Chowde Gowda, C.; Tiwary, C. S. Advance Optical Properties and Emerging Applications of 2D Materials. Frontiers in Materials **2021**, 8.

(8) Kopaczek, J.; Zelewski, S.; Yumigeta, K.; Sailus, R.; Tongay, S.; Kudrawiec, R. Temperature Dependence of the Indirect Gap and the Direct Optical Transitions at the High-Symmetry Point of the Brillouin Zone and Band Nesting in MoS2, MoSe2, MoTe2, WS2, and WSe2 Crystals. J. Phys. Chem. C **2022**, 126 (12), 5665–5674. https://doi.org/10.1021/acs.jpcc.2c01044.

(9) Santra, P.; Ghaderzadeh, S.; Ghorbani-Asl, M.; Komsa, H.-P.; Besley, E.; Krasheninnikov, A. V. Strain-Modulated Defect Engineering of Two-Dimensional Materials. npj 2D Mater Appl **2024**, 8 (1), 1–9. https://doi.org/10.1038/s41699-024-00472-x.

(10) Liang, Q.; Zhang, Q.; Zhao, X.; Liu, M.; Wee, A. T. S. Defect Engineering of Two-Dimensional Transition-Metal Dichalcogenides: Applications, Challenges, and Opportunities. ACS Nano **2021**, 15 (2), 2165–2181. https://doi.org/10.1021/acsnano.0c09666.

(11) Hossen, M. F.; Shendokar, S.; Aravamudhan, S. Defects and Defect Engineering of Two-Dimensional Transition Metal Dichalcogenide (2D TMDC) Materials. Nanomaterials **2024**, 14 (5), 410. https://doi.org/10.3390/nano14050410.

(12) Lin, Z.; Carvalho, B.; Kahn, E.; Lv, R.; Rao, R.; Terrones, H.; Pimenta, M.; Terrones, M. Defect Engineering of Two-Dimensional Transition Metal Dichalcogenides. 2D Materials **2016**, 3, 022002. https://doi.org/10.1088/2053-1583/3/2/022002.

(13) Lin, Y.-C.; Torsi, R.; Geohegan, D. B.; Robinson, J. A.; Xiao, K. Controllable Thin-Film Approaches for Doping and Alloying Transition Metal Dichalcogenides Monolayers. Advanced Science **2021**, 8 (9), 2004249. https://doi.org/10.1002/advs.202004249.

(14) Baithi, M.; Duong, D. L. Doped, Two-Dimensional, Semiconducting Transition Metal Dichalcogenides in Low-Concentration Regime. Crystals **2024**, 14 (10), 832. https://doi.org/10.3390/cryst14100832.

(15) Lan, C.; Li, C.; Ho, J.; Liu, Y. 2D WS2: From Vapor Phase Synthesis to Device Applications. Advanced Electronic Materials **2020**, 7. https://doi.org/10.1002/aelm.202000688.

(16) Niu, Y.; Gonzalez-Abad, S.; Frisenda, R.; Marauhn, P.; Drüppel, M.; Gant, P.; Schmidt, R.; Taghavi, N. S.; Barcons, D.; Molina-Mendoza, A. J.; De Vasconcellos, S. M.; Bratschitsch, R.; Perez De Lara, D.; Rohlfing, M.; Castellanos-Gomez, A. Thickness-Dependent Differential Reflectance Spectra of Monolayer and Few-Layer MoS2, MoSe2, WS2 and WSe2. Nanomaterials **2018**, 8 (9), 725. https://doi.org/10.3390/nano8090725.

(17) Wang, G.; Robert, C.; Suslu, A.; Chen, B.; Yang, S.; Alamdari, S.; Gerber, I. C.; Amand, T.; Marie, X.; Tongay, S.; Urbaszek, B. Spin-Orbit Engineering in Transition Metal Dichalcogenide Alloy Monolayers. Nat Commun **2015**, 6 (1), 10110. https://doi.org/10.1038/ncomms10110.

(18) Sulfur Vacancy Related Optical Transitions in Graded Alloys of MoxW1-xS2 Monolayers - Ghafariasl - 2024 - Advanced Optical Materials - Wiley Online Library. https://advanced.onlinelibrary.wiley.com/doi/full/10.1002/adom.202302326 (accessed 2025-04-16).

(19) Krishnan, U.; Kaur, M.; Singh, K.; Kumar, M.; Kumar, A. A Synoptic Review of MoS2: Synthesis to Applications. Superlattices and Microstructures **2019**, 128, 274–297. https://doi.org/10.1016/j.spmi.2019.02.005.

(20) Splendiani, A.; Sun, L.; Zhang, Y.; Li, T.; Kim, J.; Chim, C.-Y.; Galli, G.; Wang, F. Emerging Photoluminescence in Monolayer MoS2. Nano Lett. **2010**, 10 (4), 1271–1275. https://doi.org/10.1021/nl903868w.

(21) Kopaczek, J.; Polak, M. P.; Scharoch, P.; Wu, K.; Chen, B.; Tongay, S.; Kudrawiec, R. Direct Optical Transitions at K- and H-Point of Brillouin Zone in Bulk MoS2, MoSe2, WS2, and WSe2. Journal of Applied Physics **2016**, 119 (23), 235705. https://doi.org/10.1063/1.4954157.

(22) Mak, K. F.; Lee, C.; Hone, J.; Shan, J.; Heinz, T. F. Atomically Thin ${\mathrm{MoS}}_{2}$: A New Direct-Gap Semiconductor. Phys. Rev. Lett. **2010**, 105 (13), 136805. https://doi.org/10.1103/PhysRevLett.105.136805.

(23) Zhu, Z. Y.; Cheng, Y. C.; Schwingenschlögl, U. Giant Spin-Orbit-Induced Spin Splitting in Two-Dimensional Transition-Metal Dichalcogenide Semiconductors. Phys. Rev. B **2011**, 84 (15), 153402. https://doi.org/10.1103/PhysRevB.84.153402.

(24) Zhao, W.; Zheng, T.; Cui, Y.; Song, J.; Liu, H.; Lu, J.; Ni, Z. Observation of Band Gap Bowing Effect Vanishing in Graded-Composition Monolayer Mo1−xWxS2 Alloy. Applied Physics Letters **2024**, 124 (7), 073102. https://doi.org/10.1063/5.0188793.

(25) Tunable Band Gap Photoluminescence from Atomically Thin Transition-Metal Dichalcogenide Alloys | ACS Nano. https://pubs.acs.org/doi/abs/10.1021/nn401420h (accessed 2025-04-16).

(26) Chang, Y.-C.; Wang, Y.-K.; Chen, Y.-T.; Der Yuh, L. Facile and Reliable Thickness Identification of Atomically Thin Dichalcogenide Semiconductors Using Hyperspectral Microscopy. Nanomaterials **2020**, 10, 526. https://doi.org/10.3390/nano10030526.

(27) Frisenda, R.; Niu, Y.; Gant, P.; Molina-Mendoza, A.; Schmidt, R.; Bratschitsch, R.; Liu, J.; Fu, L.; Dumcenco, D.; Kis, A.; Perez de Lara, D.; Castellanos-Gomez, A. Micro-Reflectance and Transmittance Spectroscopy: A Versatile and Powerful Tool to Characterize 2D Materials. Journal of Physics D: Applied Physics **2017**, 50. https://doi.org/10.1088/1361-6463/aa5256.

(28) Kudrawiec, R.; Walukiewicz, W. Electromodulation Spectroscopy of Highly Mismatched Alloys. Journal of Applied Physics **2019**, 126 (14), 141102. https://doi.org/10.1063/1.5111965.

(29) Varshni, Y. P. Temperature Dependence of the Energy Gap in Semiconductors. Physica **1967**, 34 (1), 149–154. https://doi.org/10.1016/0031-8914(67)90062-6.

(30) Viña, L.; Logothetidis, S.; Cardona, M. Temperature Dependence of the Dielectric Function of Germanium. Phys. Rev. B **1984**, 30 (4), 1979–1991. https://doi.org/10.1103/PhysRevB.30.1979.

(31) Kozawa, D.; Kumar, R.; Carvalho, A.; Kumar Amara, K.; Zhao, W.; Wang, S.; Toh, M.; Ribeiro, R. M.; Castro Neto, A. H.; Matsuda, K.; Eda, G. Photocarrier Relaxation Pathway in Two-Dimensional Semiconducting Transition Metal Dichalcogenides. Nat Commun **2014**, 5 (1), 4543. https://doi.org/10.1038/ncomms5543.

(32) Kopaczek, J.; Woźniak, T.; Tamulewicz-Szwajkowska, M.; Zelewski, S. J.; Serafińczuk, J.; Scharoch, P.; Kudrawiec, R. Experimental and Theoretical Studies of the Electronic Band Structure of Bulk and Atomically Thin $Mo_{1-x}W_xSe_2$ Alloys. ACS Omega **2021**, 6 (30), 19893–19900. https://doi.org/10.1021/acsomega.1c02788.

(33) Biroju, R. K.; Maity, D.; Vretenár, V.; Vančo, Ľ.; Sharma, R.; Sahoo, M. R.; Kumar, J.; Gayathri, G.; Narayanan, T. N.; Nayak, S. K. Quantification of Alloy Atomic Composition Sites in 2D Ternary MoS2(1-x)Se2x and Their Role in Persistent Photoconductivity, Enhanced Photoresponse and Photo-Electrocatalysis. Materials Today Advances **2024**, 22, 100504. https://doi.org/10.1016/j.mtadv.2024.100504.

(34) Hong, J.; Senga, R.; Pichler, T.; Suenaga, K. Probing Exciton Dispersions of Freestanding Monolayer ${\mathrm{WSe}}_{2}$ by Momentum-Resolved Electron Energy-Loss Spectroscopy. Phys. Rev. Lett. **2020**, 124 (8), 087401. https://doi.org/10.1103/PhysRevLett.124.087401.

(35) Gong, Y.; Liu, Z.; Lupini, A. R.; Shi, G.; Lin, J.; Najmaei, S.; Lin, Z.; Elías, A. L.; Berkdemir, A.; You, G.; Terrones, H.; Terrones, M.; Vajtai, R.; Pantelides, S. T.; Pennycook, S. J.; Lou, J.; Zhou, W.; Ajayan, P. M. Band Gap Engineering and Layer-by-Layer Mapping of Selenium-Doped Molybdenum Disulfide. Nano Lett. **2014**, 14 (2), 442–449. https://doi.org/10.1021/nl4032296.

(36) Zhao, W.; Ghorannevis, Z.; Chu, L.; Toh, M.; Kloc, C.; Tan, P.-H.; Eda, G. Evolution of Electronic Structure in Atomically Thin Sheets of WS2 and WSe2. ACS Nano **2013**, 7 (1), 791–797. https://doi.org/10.1021/nn305275h.

(37) Kormányos, A.; Burkard, G.; Gmitra, M.; Fabian, J.; Zólyomi, V.; Drummond, N. D.; Fal'ko, V. K·p Theory for Two-Dimensional Transition Metal Dichalcogenide Semiconductors. 2D Mater. **2015**, 2 (2), 022001. https://doi.org/10.1088/2053-1583/2/2/022001.

(38) Feng, Q.; Mao, N.; Wu, J.; Xu, H.; Wang, C.; Zhang, J.; Xie, L. Growth of MoS2(1–x)Se2x (x = 0.41–1.00) Monolayer Alloys with Controlled Morphology by Physical Vapor Deposition. ACS Nano **2015**, 9 (7), 7450–7455. https://doi.org/10.1021/acsnano.5b02506.

(39) Kim, J.; Seung, H.; Kang, D.; Kim, J.; Bae, H.; Park, H.; Kang, S.; Choi, C.; Choi, B. K.; Kim, J. S.; Hyeon, T.; Lee, H.; Kim, D.-H.; Shim, S.; Park, J. Wafer-Scale Production of Transition Metal Dichalcogenides and Alloy Monolayers by Nanocrystal Conversion for Large-Scale Ultrathin Flexible Electronics. Nano Lett. **2021**, 21 (21), 9153–9163. https://doi.org/10.1021/acs.nanolett.1c02991.

(40) Song, J.-G.; Ryu, G. H.; Lee, S. J.; Sim, S.; Lee, C. W.; Choi, T.; Jung, H.; Kim, Y.; Lee, Z.; Myoung, J.-M.; Dussarrat, C.; Lansalot-Matras, C.; Park, J.; Choi, H.; Kim, H. Controllable Synthesis of Molybdenum Tungsten Disulfide Alloy for Vertically Composition-Controlled Multilayer. Nat Commun **2015**, 6, 7817. https://doi.org/10.1038/ncomms8817.

(41) Lee, Y.; Eu, P.; Lim, C.; Cha, J.; Kim, S.; Denlinger, J. D.; Kim, Y. Controlling Spin-Orbit Coupling Strength of Bulk Transition Metal Dichalcogenide Semiconductors. Current Applied Physics **2021**, 30, 4–7. https://doi.org/10.1016/j.cap.2021.03.008.

(42) Zhang, Y.; Li, H.; Wang, H.; Liu, R.; Zhang, S.-L.; Qiu, Z.-J. On Valence-Band Splitting in Layered MoS2. ACS Nano **2015**, 9 (8), 8514–8519. https://doi.org/10.1021/acsnano.5b03505.

(43) Qiu, D. Y.; da Jornada, F. H.; Louie, S. G. Optical Spectrum of ${\mathrm{MoS}}_{2}$: Many-Body Effects and Diversity of Exciton States. Phys. Rev. Lett. **2013**, 111 (21), 216805. https://doi.org/10.1103/PhysRevLett.111.216805.

(44) Molina-Sánchez, A.; Wirtz, L. Phonons in Single-Layer and Few-Layer MoS${}_{2}$ and WS${}_{2}$. Phys. Rev. B **2011**, 84 (15), 155413. https://doi.org/10.1103/PhysRevB.84.155413.

(45) Bandgap engineering of MoS2/MX2 (MX2 = WS2, MoSe2 and WSe2) heterobilayers subjected to biaxial strain and normal compressive strain - RSC Advances (RSC Publishing). https://pubs.rsc.org/en/content/articlelanding/2016/ra/c5ra27871f?utm_source=chatgpt.com (accessed 2025-06-09).

(46) Ho, C. H.; Liao, P. C.; Huang, Y. S.; Tiong, K. K. Temperature Dependence of Energies and Broadening Parameters of the Band-Edge Excitons of ReS2 and ReSe2. Phys. Rev. B **1997**, 55 (23), 15608–15613. https://doi.org/10.1103/PhysRevB.55.15608.

Supporting information file for:

Sensitivity of excitonic transitions to temperature in monolayers of TMD alloys

K. Ciesiołkiewicz-Klepek[1, a)], J. Kopaczek[1], J. Serafińczuk[2], R. Kudrawiec[1, b)]

[1]*Department of Semiconductor Materials Engineering, Wroclaw University of Science and Technology, Wybrzeże Wyspiańskiego 27, 50-370 Wrocław, Poland*

[2]*Department of Nanometrology, Wroclaw University of Science and Technology, Wybrzeże Wyspiańskiego 27, 50-370 Wrocław, Poland*

[a)] *e-mail address: karolina.ciesiolkiewicz@pwr.edu.pl*
[b)] *e-mail address: robert.kudrawiec@pwr.edu.pl*

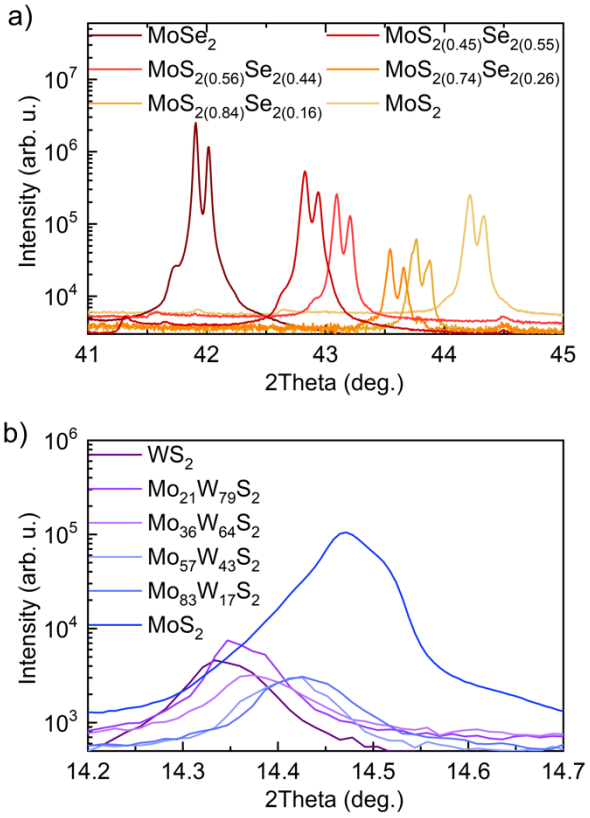

Figure S1. X-ray diffraction (XRD) patterns of $Mo(S_{1-x}Se_x)_2$ (a) and $Mo_{1-x}W_xS_2$ (b) alloys measured using CuKα_1 radiation (λ = 1.540598 Å) in Bragg–Brentano geometry. For $Mo(S_{1-x}Se_x)_2$, bulk fragments were measured directly, while $Mo_{1-x}W_xS_2$ required exfoliation to obtain homogeneous regions. The alloy compositions were determined based on the positions of the (00.6) and (00.2) reflections for $Mo(S_{1-x}Se_x)_2$ and $Mo_{1-x}W_xS_2$, respectively, assuming a linear variation of lattice parameters between the binary endpoints (i.e., MoS_2–$MoSe_2$ and MoS_2–WS_2).

3. Conclusions

This doctoral thesis presents a coherent concept for the application of fiber optic technology for the spectroscopic characterization of bulk materials, thin films, and monolayers of vdW crystals and group III-V semiconductors. The experimental platform, based on optical fibers, has been successfully developed and used in a variety of measurement configurations, enabling studies from room temperature to cryogenic temperatures, with high stability and precision.

In the first stage of the work, the fiber optics were integrated with classical PR and CER systems, allowing for the physical separation of the measurement zone from other instrument components. Although fiber optics have been occasionally used in PR configurations, the available literature has not yet described a systematic analysis of the effect of the fiber core diameter or its distance from the sample on signal parameters. The studies presented here, using optical fibers with core diameters of 50, 105, and 400 μm, provide new insights into the possibilities of spatially mapping optical properties and selecting the appropriate experimental setup. To the best of our knowledge, this is the first reported integration of an optical fiber with a CER system, where the fiber ferrule also serves as an active capacitor electrode. This design eliminated the shadow effect, increased sample and operator safety, and significantly amplified the signal. Furthermore, the beneficial effect of a sapphire dielectric between the electrodes on signal amplitude and protection against electrical breakdown was demonstrated.

The remainder of this thesis focuses on the development of an optical platform in which the investigated samples are coupled to optical fibers. Among the techniques implemented, a thermal transmittance spectroscopy method was developed based on a LOF configuration, where thin layers of MoS_2, $MoSe_2$, WS_2, and WSe_2 were transferred directly onto the fiber end facet. Due to the low heat capacity of the tested materials and the poor thermal conductivity of the glass fiber, laser illumination resulted in a local increase in sample temperature. Immediate shifts in the A and B excitonic transitions and a reduction in the absorption coefficient (up to 60%) were observed, indicating the potential use of this type of configuration in fiber-optic optical modulators and temperature sensors.

The third stage of the studies involved the development of a complete system for measurements at low temperatures (~20 K), based on a closed-cycle helium cryostat. Using a fiber-to-fiber adapter mounted in place of a standard optical window on the vacuum shroud, high positioning stability, resistance to mechanical vibrations, and no temperature drift were achieved. This system enabled measurements of PL, transmission, PT, and PR as a function of temperature. Samples of various dimensionalities and architectures were successfully studied: from thin films, through monolayers, to heterostructures.

In the final part of the thesis, a developed system was used to analyze the positions of A, B, and C transitions in monolayer alloys of MoS_2-based dichalcogenides. It was observed that substituting sulfur with selenium leads to a redshift of the excitonic transitions, while replacing molybdenum with tungsten results in a shift toward higher energies. Furthermore, it was shown that the temperature sensitivity of excitons also depends on the material's chemical composition, the degree of change in transition energy with temperature is significantly greater in the presence of tungsten or selenium.

All of the results obtained in this work confirm the central hypothesis that integrating optical fibers with spectroscopic systems expands the experimental capabilities for characterizing 2D materials. The developed fiber-based techniques enable precise, stable, and flexible measurements under both ambient and cryogenic conditions, offering strong potential for applications in spectroscopy, optical sensing, and fiber-integrated photonic devices.

Bibliography

1. Ghatak, A. K. & Thyagarajan, K. *An Introduction to Fiber Optics*. (Cambridge University Press, 1998).
2. *Lab-on-Fiber Technology*. (Springer International Publishing, Cham, 2015). doi:10.1007/978-3-319-06998-2.
3. Kostovski, G., Stoddart, P. R. & Mitchell, A. The Optical Fiber Tip: An Inherently Light-Coupled Microscopic Platform for Micro- and Nanotechnologies. *Advanced Materials* **26**, 3798–3820 (2014).
4. Fox, M. *Optical Properties of Solids*. *American Journal of Physics* vol. 70 (2001).
5. Yu, P. Y. & Cardona, M. *Fundamentals of Semiconductors: Physics and Materials Properties*. (Springer, Berlin, Heidelberg, 2010). doi:10.1007/978-3-642-00710-1.
6. Xiong, Y. & Xu, F. Multifunctional integration on optical fiber tips: challenges and opportunities. *AP* **2**, 064001 (2020).
7. Chen, J., Xiong, Y., Xu, F. & Lu, Y. Silica optical fiber integrated with two-dimensional materials: towards opto-electro-mechanical technology. *Light Sci Appl* **10**, 78 (2021).
8. Mas-Ballesté, R., Gómez-Navarro, C., Gómez-Herrero, J. & Zamora, F. 2D materials: to graphene and beyond. *Nanoscale* **3**, 20–30 (2011).
9. Butler, S. Z. *et al.* Progress, Challenges, and Opportunities in Two-Dimensional Materials Beyond Graphene. *ACS Nano* **7**, 2898–2926 (2013).
10. Novoselov, K. S., Mishchenko, A., Carvalho, A. & Castro Neto, A. H. 2D materials and van der Waals heterostructures. *Science* **353**, aac9439 (2016).
11. Berkelbach, T. C. & Reichman, D. R. Optical and Excitonic Properties of Atomically Thin Transition-Metal Dichalcogenides. *Annual Review of Condensed Matter Physics* **9**, 379–396 (2018).
12. Dutta, T. *et al.* Electronic properties of 2D materials and their junctions. *Nano Materials Science* (2023) doi:10.1016/j.nanoms.2023.05.003.

13. Kim, J. H., Jeong, J. H., Kim, N., Joshi, R. & Lee, G.-H. Mechanical properties of two-dimensional materials and their applications. *J. Phys. D: Appl. Phys.* **52**, 083001 (2019).

14. Lee, J. Y., Shin, J.-H., Lee, G.-H. & Lee, C.-H. Two-Dimensional Semiconductor Optoelectronics Based on van der Waals Heterostructures. *Nanomaterials* **6**, 193 (2016).

15. Tang, Z., Chen, S., Li, D., Wang, X. & Pan, A. Two-dimensional optoelectronic devices for silicon photonic integration. *Journal of Materiomics* **9**, 551–567 (2023).

16. Niu, Y. *et al.* Thickness-Dependent Differential Reflectance Spectra of Monolayer and Few-Layer MoS2, MoSe2, WS2 and WSe2. *Nanomaterials* **8**, 725 (2018).

17. Carrascoso, F., Li, H., Frisenda, R. & Castellanos-Gomez, A. Strain engineering in single-, bi- and tri-layer MoS2, MoSe2, WS2 and WSe2. *Nano Res.* **14**, 1698–1703 (2021).

18. Baithi, M. & Duong, D. L. Doped, Two-Dimensional, Semiconducting Transition Metal Dichalcogenides in Low-Concentration Regime. *Crystals* **14**, 832 (2024).

19. Kopaczek, J. *et al.* Temperature Dependence of the Indirect Gap and the Direct Optical Transitions at the High-Symmetry Point of the Brillouin Zone and Band Nesting in MoS2, MoSe2, MoTe2, WS2, and WSe2 Crystals. *J. Phys. Chem. C* **126**, 5665–5674 (2022).

20. Biroju, R. K. *et al.* Quantification of alloy atomic composition sites in 2D ternary MoS2(1-x)Se2x and their role in persistent photoconductivity, enhanced photoresponse and photo-electrocatalysis. *Materials Today Advances* **22**, 100504 (2024).

21. Withers, F. *et al.* Light-emitting diodes by band-structure engineering in van der Waals heterostructures. *Nature Mater* **14**, 301–306 (2015).

22. Bao, Q. *et al.* Atomic-Layer Graphene as a Saturable Absorber for Ultrafast Pulsed Lasers. *Advanced Functional Materials* **19**, 3077–3083 (2009).

23. Photodetectors Based on Van der Waals Heterostructures and Hybrid 2D Materials. *AIP Publishing* https://pubs.aip.org/collection/994/Photodetectors-Based-on-Van-der-Waals.

24. Wei, W. *et al.* Graphene-MoS2 Hybrid Structure Enhanced Fiber Optic Surface Plasmon Resonance Sensor. *Plasmonics* **12**, 1–8 (2017).

25. Cardona, M. Modulation Spectroscopy of Semiconductors. in *Advances in Solid State Physics* (ed. Madelung, O.) 125–173 (Pergamon, 1970). doi:10.1016/B978-1-4831-2427-8.50007-3.

26. Kudrawiec, R. & Misiewicz, J. Optical Modulation Spectroscopy. *Semiconductor Research: Experimental Techniques* 95 (2012) doi:10.1007/978-3-642-23351-7_4.

27. Kudrawiec, R. & Walukiewicz, W. Electromodulation spectroscopy of highly mismatched alloys. *Journal of Applied Physics* **126**, 141102 (2019).

28. Spektroskopia fotoodbiciowa struktur półprzewodnikowych - Jan Misiewicz | książka w tezeusz.pl książki promocje, używane książki, nowości wydawnicze. https://tezeusz.pl/spektroskopia-fotoodbiciowa-struktur-polprzewodnikowych-jan-misiewicz.

29. Seraphin, B. O. & Bottka, N. Band-Structure Analysis from Electro-Reflectance Studies. *Phys. Rev.* **145**, 628–636 (1966).

30. Aspnes, D. E. Third-derivative modulation spectroscopy with low-field electroreflectance. *Surface Science* **37**, 418–442 (1973).

31. Glembocki, O. J. & Shanabrook, B. V. Chapter 4 Photoreflectance Spectroscopy of Microstructures. in *Semiconductors and Semimetals* (eds. Seiler, D. G. & Littler, C. L.) vol. 36 221–292 (Elsevier, 1992).

32. Practical thermoreflectance design for optical characterization of layer semiconductors | Review of Scientific Instruments | AIP Publishing. https://pubs.aip.org/aip/rsi/article-abstract/75/4/1098/466456/Practical-thermoreflectance-design-for-optical?redirectedFrom=fulltext.

33. Matatagui, E., Thompson, A. G. & Cardona, M. Thermoreflectance in Semiconductors. *Phys. Rev.* **176**, 950–960 (1968).

34. Berglund, C. N. Temperature-Modulated Optical Absorption in Semiconductors. *J. Appl. Phys.* **37**, 3019–3023 (1966).

35. Varshni, Y. P. Temperature dependence of the energy gap in semiconductors. *Physica* **34**, 149–154 (1967).

36. Logothetidis, S., Cardona, M., Lautenschlager, P. & Garriga, M. Temperature dependence of the dielectric function and the interband critical points of CdSe. *Phys. Rev. B* **34**, 2458–2469 (1986).

37. Logothetidis, S., Via, L. & Cardona, M. Temperature dependence of the dielectric function and the interband critical points of InSb. *Phys. Rev. B* **31**, 947–957 (1985).

38. Lautenschlager, P., Garriga, M., Logothetidis, S. & Cardona, M. Interband critical points of GaAs and their temperature dependence. *Phys. Rev. B* **35**, 9174–9189 (1987).

39. Vyas, K. *et al.* Group III-V semiconductors as promising nonlinear integrated photonic platforms. *Advances in Physics: X* (2022).

40. Wang, Y. Electronic structure of III-V zinc-blende semiconductors from first principles. *Phys. Rev. B* **87**, (2013).

41. De, A. & Pryor, C. E. Predicted band structures of III-V semiconductors in the wurtzite phase. *Phys. Rev. B* **81**, 155210 (2010).

42. Wonglakhon, T. & Zahn, D. Interaction potentials for modelling GaN precipitation and solid state polymorphism. *J. Phys.: Condens. Matter* **32**, 205401 (2020).

43. Kuech, T. F. III-V compound semiconductors: Growth and structures. *Progress in Crystal Growth and Characterization of Materials* **62**, 352–370 (2016).

44. Zhao, C. *et al.* Novel III-V semiconductor epitaxy for optoelectronic devices through two-dimensional materials. *Progress in Quantum Electronics* **76**, 100313 (2021).

45. Electric Field Effect in Atomically Thin Carbon Films | Science. https://www.science.org/doi/10.1126/science.1102896.

46. Slavich, A. S. *et al.* Exploring van der Waals materials with high anisotropy: geometrical and optical approaches. *Light Sci Appl* **13**, 68 (2024).

47. Manzeli, S., Ovchinnikov, D., Pasquier, D., Yazyev, O. V. & Kis, A. 2D transition metal dichalcogenides. *Nat Rev Mater* **2**, 1–15 (2017).

48. Xia, F., Wang, H., Xiao, D., Dubey, M. & Ramasubramaniam, A. Two-dimensional material nanophotonics. *Nature Photon* **8**, 899–907 (2014).

49. Xu, X., Yao, W., Xiao, D. & Heinz, T. F. Spin and pseudospins in layered transition metal dichalcogenides. *Nature Phys* **10**, 343–350 (2014).

50. Akinwande, D. *et al.* Graphene and two-dimensional materials for silicon technology. *Nature* **573**, 507–518 (2019).

51. Nanodevice Laboratory. http://nanodevice.yonsei.ac.kr/?mid=topic_TMDC&ckattempt=1.

52. Schneider, C., Glazov, M. M., Korn, T., Höfling, S. & Urbaszek, B. Two-dimensional semiconductors in the regime of strong light-matter coupling. *Nat Commun* **9**, 2695 (2018).

53. Mueller, T. & Malic, E. Exciton physics and device application of two-dimensional transition metal dichalcogenide semiconductors. *npj 2D Mater Appl* **2**, 1–12 (2018).

54. Singh, A. K. *et al.* Review of strategies toward the development of alloy two-dimensional (2D) transition metal dichalcogenides. *iScience* **24**, 103532 (2021).

55. Wang, G. *et al.* Spin-orbit engineering in transition metal dichalcogenide alloy monolayers. *Nat Commun* **6**, 10110 (2015).

56. Tunable Band Gap Photoluminescence from Atomically Thin Transition-Metal Dichalcogenide Alloys | ACS Nano. https://pubs.acs.org/doi/abs/10.1021/nn401420h.

57. Sulfur Vacancy Related Optical Transitions in Graded Alloys of MoxW1-xS2 Monolayers - Ghafariasl - 2024 - Advanced Optical Materials - Wiley Online Library. https://advanced.onlinelibrary.wiley.com/doi/full/10.1002/adom.202302326.

58. Ning, C.-Z., Dou, L. & Yang, P. Bandgap engineering in semiconductor alloy nanomaterials with widely tunable compositions. *Nat Rev Mater* **2**, 17070 (2017).

59. 2D Layered Material Alloys: Synthesis and Application in Electronic and Optoelectronic Devices - Yao - 2022 - Advanced Science - Wiley Online Library. https://advanced.onlinelibrary.wiley.com/doi/full/10.1002/advs.202103036.

60. Li, Y., Kuang, G., Jiao, Z., Yao, L. & Duan, R. Recent progress on the mechanical exfoliation of 2D transition metal dichalcogenides. *Mater. Res. Express* **9**, 122001 (2022).

61. Bonding - Carbon Allotropes (A-Level Chemistry). *Study Mind* https://studymind.co.uk/notes/carbon-allotropes/.

62. Tamulewicz-Szwajkowska, M., Zelewski, S. J., Serafińczuk, J. & Kudrawiec, R. Geometric progress in the thickness of exfoliated van der Waals crystals on the example of MoS2. *AIP Advances* **12**, 025328 (2022).

63. Nguyen, D. C. *et al*. Visibility of hexagonal boron nitride on transparent substrates. *Nanotechnology* **31**, 195701 (2020).

64. Guan, L. *et al*. Metal-assisted exfoliation of few-layer black phosphorus with high yield. *Chem. Commun.* **54**, 595–598 (2018).

65. Elshof, J. E. ten, Yuan, H. & Rodriguez, P. G. Two-Dimensional Metal Oxide and Metal Hydroxide Nanosheets: Synthesis, Controlled Assembly and Applications in Energy Conversion and Storage. *Advanced Energy Materials* **6**, 1600355 (2016).

66. Novoselov, K. S. & Castro Neto, A. H. Two-dimensional crystals-based heterostructures: materials with tailored properties. *Phys. Scr.* **2012**, 014006 (2012).

67. Parvez, K., Yang, S., Feng, X. & Müllen, K. Exfoliation of graphene via wet chemical routes. *Synthetic Metals* **210**, 123–132 (2015).

68. Zhao, M., Casiraghi, C. & Parvez, K. Electrochemical exfoliation of 2D materials beyond graphene. *Chemical Society Reviews* **53**, 3036–3064 (2024).

69. Chavalekvirat, P., Hirunpinyopas, W., Deshsorn, K., Jitapunkul, K. & Iamprasertkun, P. Liquid Phase Exfoliation of 2D Materials and Its Electrochemical Applications in the Data-Driven Future. *Precision Chemistry* (2024) doi:10.1021/prechem.3c00119.

70. Wang, S. *et al*. Electrochemical molecular intercalation and exfoliation of solution-processable two-dimensional crystals. *Nat Protoc* **18**, 2814–2837 (2023).

71. Yang, R. *et al*. Synthesis of atomically thin sheets by the intercalation-based exfoliation of layered materials. *Nature Synthesis* **2**, 101–118 (2023).

72. Paul, S., Chandra, P., Kumar, D. & Khan, R. Electrochemical Exfoliation of Graphene and Its Derivatives and Its Extended Applications in Therapeutics. in 263–281 (2024). doi:10.1007/978-981-97-2128-3_10.

73. Lee, Y.-H. *et al*. Synthesis of Large-Area MoS2 Atomic Layers with Chemical Vapor Deposition. *Advanced Materials* **24**, 2320–2325 (2012).

74. Tang, L., Tan, J., Nong, H., Liu, B. & Cheng, H.-M. Chemical Vapor Deposition Growth of Two-Dimensional Compound Materials: Controllability, Material Quality, and Growth Mechanism. *Accounts of Materials Research* (2020) doi:10.1021/accountsmr.0c00063.

75. Shanmugam, V. *et al.* A Review of the Synthesis, Properties, and Applications of 2D Materials. *Particle & Particle Systems Characterization* **39**, 2200031 (2022).

76. (16) (PDF) Recent Advancement on the Optical Properties of Two-Dimensional Molybdenum Disulfide (MoS2) Thin Films. https://www.researchgate.net/publication/276868273_Recent_Advancement_on_the_Optical_Properties_of_Two-Dimensional_Molybdenum_Disulfide_MoS2_Thin_Films/figures?lo=1.

77. Castellanos-Gomez, A. *et al.* Van der Waals heterostructures. *Nat Rev Methods Primers* **2**, 1–19 (2022).

78. Geim, A. K. & Grigorieva, I. V. Van der Waals heterostructures. *Nature* **499**, 419–425 (2013).

79. Gupta, N., Sachin, S., Kumari, P., Rani, S. & Jyoti Ray, S. Twistronics in two-dimensional transition metal dichalcogenide (TMD)-based van der Waals interface. *RSC Advances* **14**, 2878–2888 (2024).

80. Calman, E. *et al.* Indirect excitons in van der Waals heterostructures at room temperature. *Nature Communications* **9**, (2018).

81. Zhou, Z. *et al.* Ultralong lifetime for fully photogenerated spin-polarized current in two-dimensional ferromagnetic/nonmagnetic semiconductor heterostructures. *Phys. Rev. B* **103**, 245411 (2021).

82. Drögeler, M. *et al.* Nanosecond Spin Lifetimes in Single- and Few-Layer Graphene-hBN Heterostructures at Room Temperature. *Nano Letters* **14**, 6050 (2014).

83. Liao, W., Huang, Y., Wang, H. & Zhang, H. Van der Waals heterostructures for optoelectronics: Progress and prospects. *Applied Materials Today* **16**, 435–455 (2019).

84. Doan, M.-H. & Bøggild, P. Interface engineering of van der Waals heterostructures towards energy-efficient quantum devices operating at high temperatures. *2D Mater.* **12**, 022002 (2025).

85. Pei, S., Cao, R., Zhou, Y.-H., Zheng, X. & Wang, C. Tunable band alignment and optical properties in van der Waals heterostructures based on two-dimensional materials Janus-MoSSe and C3N4. *New J. Phys.* **26**, 043014 (2024).

86. Hoque, M. A. *et al.* All-2D CVD-grown semiconductor field-effect transistors with van der Waals graphene contacts. *npj 2D Mater Appl* **8**, 1–7 (2024).

87. Zhou, S. & Peng, B. Non-volatile optical memory in vertical van der Waals heterostructures. *J. Semicond.* **41**, 072906 (2020).

88. Van der Waals engineering of ferromagnetic semiconductor heterostructures for spin and valleytronics | Science Advances. https://www.science.org/doi/10.1126/sciadv.1603113.

89. Du, L. *et al.* Moiré photonics and optoelectronics. *Science* **379**, eadg0014 (2023).

90. Agrawal, G. P. *Fiber-Optic Communication Systems*. (John Wiley & Sons, 2012).

91. Stepniewski, G. *et al.* From D-shaped to D-shape optical fiber – A universal solution for sensing and biosensing applications: Drawn D-shape fiber and its sensing applications. *Measurement* **222**, 113642 (2023).

92. Selvaraja, S. K., Sethi, P., Selvaraja, S. K. & Sethi, P. Review on Optical Waveguides. in *Emerging Waveguide Technology* (IntechOpen, 2018). doi:10.5772/intechopen.77150.

93. Knight, J. C. Photonic crystal fibres. *Nature* **424**, 847–851 (2003).

94. Barnard, C. W. & Lit, J. W. Y. Mode transforming properties of tapered single-mode fiber microlenses. *Appl. Opt., AO* **32**, 2090–2094 (1993).

95. Gao, H. H., Chen, Z., Kumar, J., Tripathy, S. K. & Kaplan, D. L. Tapered fiber tips for fiber optic biosensors. *OE* **34**, 3465–3470 (1995).

96. Matějec, V., Kašík, I. & Bartoň, I. Fiber-Optic Nanosensors for Chemical Detection. *Chemosensors* **11**, 521 (2023).

97. Optical Fiber Tweezers: A Versatile Tool for Optical Trapping and Manipulation. https://www.mdpi.com/2072-666X/11/2/114.

98. Slavik, R., Homola, J., Ctyroky, J. & Brynda, E. Novel Spectral Fiber Optic Sensor based on Surface Plasmon Resonance, Sensors and Actuators B, 74, 106-111. *Sensors and Actuators B: Chemical* **74**, 106–111 (2001).

99. Side-Polish Plastic Optical Fiber Based SPR Sensor for Refractive Index and Liquid-Level Sensing. https://www.mdpi.com/1424-8220/22/16/6241.

100. Emami, S. D. *et al.* Micro-bending based optical band-pass filter and its application in S-band Thulium-doped fiber amplifier. *Opt. Express, OE* **20**, 29784–29797 (2012).

101. Rajan, G. *et al.* A Photonic Crystal Fiber and Fiber Bragg Grating-Based Hybrid Fiber-Optic Sensor System. *IEEE Sensors Journal* **12**, 39–43 (2012).

102. Korposh, S., James, S. W., Lee, S.-W. & Tatam, R. P. Tapered Optical Fibre Sensors: Current Trends and Future Perspectives. *Sensors* **19**, 2294 (2019).

103. Borzycki, K. & Osuch, T. Hollow-Core Optical Fibers for Telecommunications and Data Transmission. *Applied Sciences* **13**, 10699 (2023).

104. Tomaszewska-Rolla, D. *et al.* Mid-infrared optical frequency comb spectroscopy using an all-silica antiresonant hollow-core fiber. *Opt. Express, OE* **32**, 10679–10689 (2024).

105. Snelders, D. & Boersma, A. Development of Thermostable FBG Optical Sensor for Oil and Gas Applications. *Proceedings of the 8th International Conference on Sensing Technology* **7**, 278–281 (2014).

106. Urquhart, P. Review of rare earth doped fibre lasers and amplifiers. *IEE Proceedings J (Optoelectronics)* **135**, 385–407 (1988).

107. Shen, Y. *et al.* Picosecond supercontinuum generation in large mode area photonic crystal fibers for coherent anti-Stokes Raman scattering microspectroscopy. *Sci Rep* **8**, 9526 (2018).

108. Zhou, Y., Cheung, K. K. Y., Yang, S., Chui, P. C. & Wong, K. K. Y. Widely tunable picosecond optical parametric oscillator using highly nonlinear fiber. *Opt. Lett., OL* **34**, 989–991 (2009).

109. Liu, D., Sun, Q., Lu, P., Xia, L. & Sima, C. Research progress in the key device and technology for fiber optic sensor network. *Photonic Sens* **6**, 1–25 (2016).

110. Xiong, Y.-F., Chen, J.-H., Lu, Y.-Q. & Xu, F. Broadband Optical-Fiber-Compatible Photodetector Based on a Graphene-MoS2-WS2 Heterostructure with a Synergetic Photogenerating Mechanism. *Advanced Electronic Materials* **5**, 1800562 (2019).

111. Crooker, S. A. Fiber-coupled antennas for ultrafast coherent terahertz spectroscopy in low temperatures and high magnetic fields. *Rev. Sci. Instrum.* **73**, 3258–3264 (2002).

112. Crooker, S. A., Rickel, D. G., Lyo, S. K., Samarth, N. & Awschalom, D. D. Magnetic semiconductor quantum wells in high fields to 60 Tesla: Photoluminescence linewidth annealing at magnetization steps. *Phys. Rev. B* **60**, R2173–R2176 (1999).

113. Battesti, R. *et al.* High magnetic fields for fundamental physics. *Physics Reports* **765–766**, 1–39 (2018).

114. Zheng, B.-C. *et al.* Miniature optical fiber current sensor based on a graphene membrane. *Laser & Photonics Reviews* **9**, 517–522 (2015).